Inflated Exoplanets

Master Thesis

October 31, 2013

Daves Tomasz Benedykt Hoszowski

Dark Cosmology Centre &
Centre for Star and Planet Formation
Niels Bohr Institute
University of Copenhagen

Supervisor:
Assoc. Prof. Anja C. Andersen
Dark Cosmology Centre

Former supervisor:
PDRA. Lars Buchhave
Centre for Star and Planet Formation

Abstract

Planets vary in many physical properties, and those of exoplanets are quite unusual compared to the planets in our solar system. The Jovian planets, Jupiter and Saturn, have partially degenerate interiors which ensure that the planets have similar radii, but vary in mass. But similar radii are not observed for the Jovian-exoplanets, where the radii can vary by a factor of 2. This observation contradicts the models of the mass-radius relation and raises the question whether the models are faulty or a heating mechanism is in progress.

To answer the question, a description of the different detection techniques of exoplanets is made. This description tells us which method is required to investigate the exoplanets' physical properties. Measurements of two systems from the Kepler Objects of Interest (KOI) are made to investigate if their radius is larger than expected, also known as inflated. But, it turns out that these exoplanets are not inflated, and can be explained by stellar irradiated exoplanet models. Therefore I have chosen a sample of 11 exoplanets, which all have a density below 0.2 g cm^{-3}. The boundary is chosen to ensure that the exoplanets are inflated and that they are not following the mass-radii relation. The low-density exoplanets will be discussed on the base of three different heating mechanisms; enhanced atmosphere, tidal heating and ohmic dissipation.

Tidal heating is a viable solution, but not for all cases of inflated exoplanets. Ohmic heating could explain most events, but lacks evidence of its effect within the atmosphere. A detailed discussion of the low-density exoplanets illustrates the need of improving the data, and especially spectra, which can constrain parameters of the atmosphere.

A better understanding of inflated exoplanets could help astronomers understand how an irradiated envelope behaves. A greater understanding of the envelope will as well help physicists understand what happens to Hydrogen and Helium at high pressures, which are irreproducible on Earth.

Resume

Planeter varierer på mange fysiske egenskaber, og exoplaneter er ganske usædvanlige iforhold til planeterne i vores solsystem. Gaskæmperne, Jupiter og Saturn, har delvist en degenererede kerne, som sikrer en omtrent fast radius til forskellige masser. Men samme tendens er ikke observeret for Jupiter-lignende exoplaneter, hvor radiussen kan variere med en faktor på 2. Denne observation modsiger modellerne for forholdet mellem massen og radiussen af planeter, og dermed rejser spørgsmålet sig; om modellerne er forkerte eller er der en igangvrende ekstern opvarmnings mekanisme.

For at besvare spørgsmålet laves der en oversigt over de forskelige observations teknikker af exoplaneter. Denne oversigt fortæller os, hvilken metode er nødvendig for at undersøge exoplaneternes fysiske egenskaber. Observations data af to systemer fra *Kepler* kataloget bliver analyseret for at undersøge om deres radius er større end forventet, også kendt som, oppustet. Men det viser sig, at disse exoplaneter ikke er oppustet, og kan forklares ved modeller for bestrålede exoplaneter. Derfor har jeg taget en stikprøve på 11 exoplaneter, der alle har en massefylde på under 0.2 g cm^{-3}. Denne grænse er valgt for at sikre mig, at exoplaneterne er oppustet, og at de ikke følger forholdet mellem massen og radius. Disse vil blive analyseret på grundlag af tre forskellige opvarmnings mekanismer; tykkere atmosfære, tidevands krafter og ohmsk opvarmning.

Opvarmning ved tidevands krafter er en løsning for nogle oppustet exoplaneter, men ikke for alle. Ohmsk opvarmning kan forklare de fleste tilfælde, men mangler beviser for dens effekt i atmosfæren. En detaljeret diskussion af min stikprøve illustrerer behovet for at forbedre dataene, og især spektre, som kan begrænse parametrene for atmosfæren.

En bedre forståelse af oppustede exoplaneter kan hjælpe astronomerne med at forstå, hvordan en bestrålet atmosfære opfører sig. En større forståelse af det ydre lag af en planet vil hjælpe fysikkere med at forstå, hvad der sker med brint og helium ved højt tryk, som endnu ikke er muligt at opnå på Jorden.

Acknowledgements

First of all, I would like to thank my friends and family for the support and understanding of my work. This one-year project has been frustrating, involving 3 supervisor shifts and two initiated theses, but my social network kept me through it in one piece

My greeting list for astronomers, who helped me during my thesis is long. But here it goes; Adam Burrows, Hanno Rein, Neil Miller, Christoffer Karoff, Brandon W. Tingley, Brian Hinrup and Simon Albrecht. I would like to thank you for helping me out with questions, read-through, and increasing my network in Astronomy. You are the motivation that made me reconsider applying for a Ph.D.

I would like to thank my supervisor, Anja Andersen, who helped me out after my former supervisor got a position at Harvard University. She has been there for me from the first courses in Astronomy and till the end of my thesis. I thank you for being a role model and source of inspiration.

At last, I would like to mention a fun notice that I have made during my work. I started working with a database containing more or less 890 exoplanets, but the database was static - no changes were made, and all my values were outdated. Then I swapped to a dynamic database, which contained 900 exoplanets and all candidates. As I started to write my thesis, I noticed how fast the field of exoplanets progresses, with new exoplanets every week. And half-a-year later, I have to update all my plots to include the new exoplanets.

This field is growing so rapid, and becoming more fascinating by each second!

I hope you will enjoy reading my thesis and become fascinated by exoplanets, as I am!

Contents

CHAPTER 1

Introduction

Exoplanetary science has received a major observational boost within the last 25 years. In the late 1987, the first exoplanet (extrasolar planet) was proposed by Campbell et al. (1988), but another detection was not possible for confirmation. The first confirmed exoplanet was published in 1995: A close-in half Jupiter mass exoplanet orbiting 51-Pegasi (Mayor and Queloz, 1995). Following this detection came a large number of observed close-in Jupiter mass exoplanets, later to be called, "Hot-Jupiters"[1]. The observed hot-Jupiters puzzled astronomers, since they didn't resemble our solar system. But, it was as well known that the observational techniques were biased towards larger exoplanets at close orbits to the stellar host.

The observations have increased during the past years, as can be seen on Figure 1.1. The figure depicts the detection of confirmed exoplanets as a function of time.

[1]Close-in orbits are usually defined as, < 0.1 AU or an orbital period less than 10 days (Beaugé and Nesvorný, 2013)

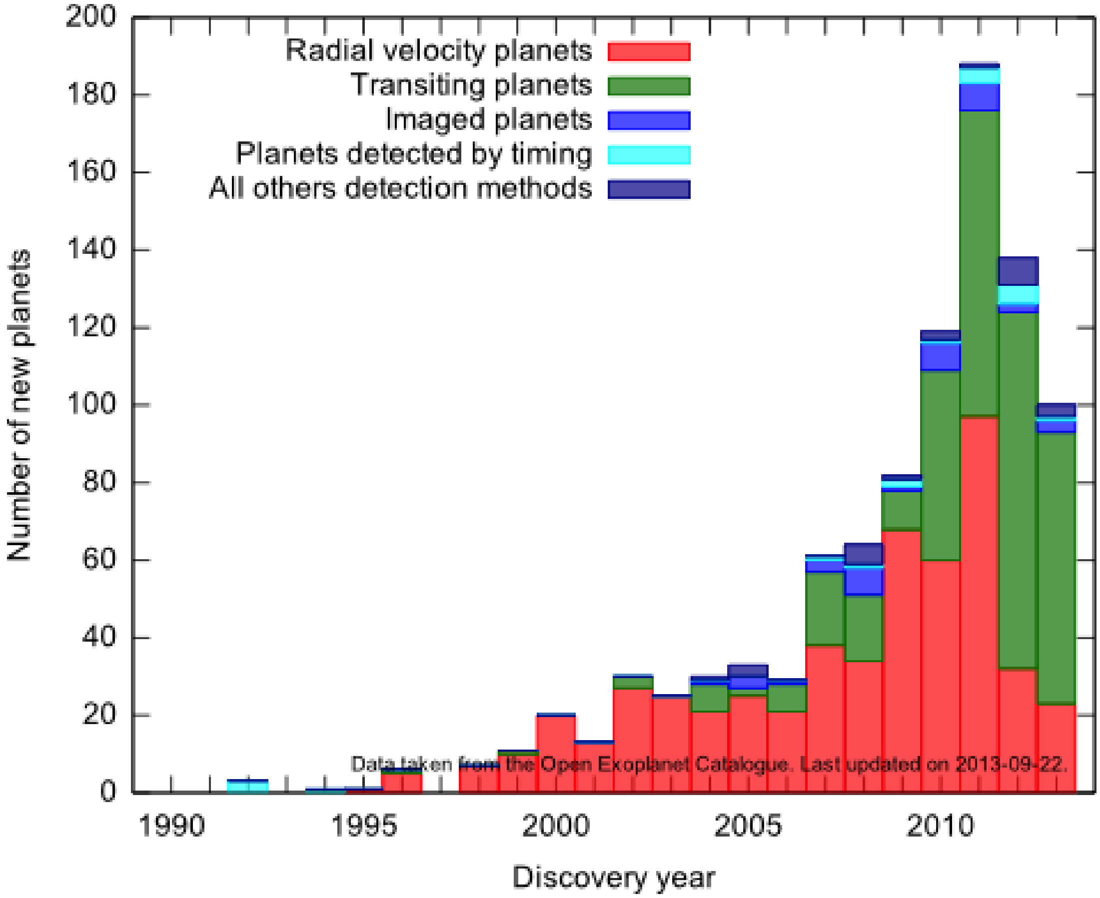

Figure 1.1: A plot of the observation of confirmed exoplanets as a function of time. The different methods are indicated by colors; the annotations are written within the figure. The image is taken from Open Exoplanet Catalogue (Rein, 2012)

The number of transit exoplanets has increased over the past 4 years, primarily due to the launch of the space telescope, *Kepler*, in 2009. The space telescope observes a field[1] of known stars by looking at them with its photometric aperture, thus being able to detect transits; a planet that passes in front of the star, as illustrated in Figure 2.1 at page 10.

Most of the exoplanets observed by *Kepler* are still candidates; or in other words,

[1]This field of view is fixed, and covers 115 square degrees of the sky or around 0.28 percent of the sky

exoplanets, which are not yet confirmed. A confirmation of an exoplanet is achieved as soon as another detection method can verify exoplanetary behavior; like a dip in the light-curve from the star or minor systematic deviations in the stellar motion. The detections of *Kepler* show that our galaxy might not be filled with Hot-Jupiters as previously observed, because a majority of Neptune-sized exoplanet candidates are observed. This can be seen on Figure 1.2.

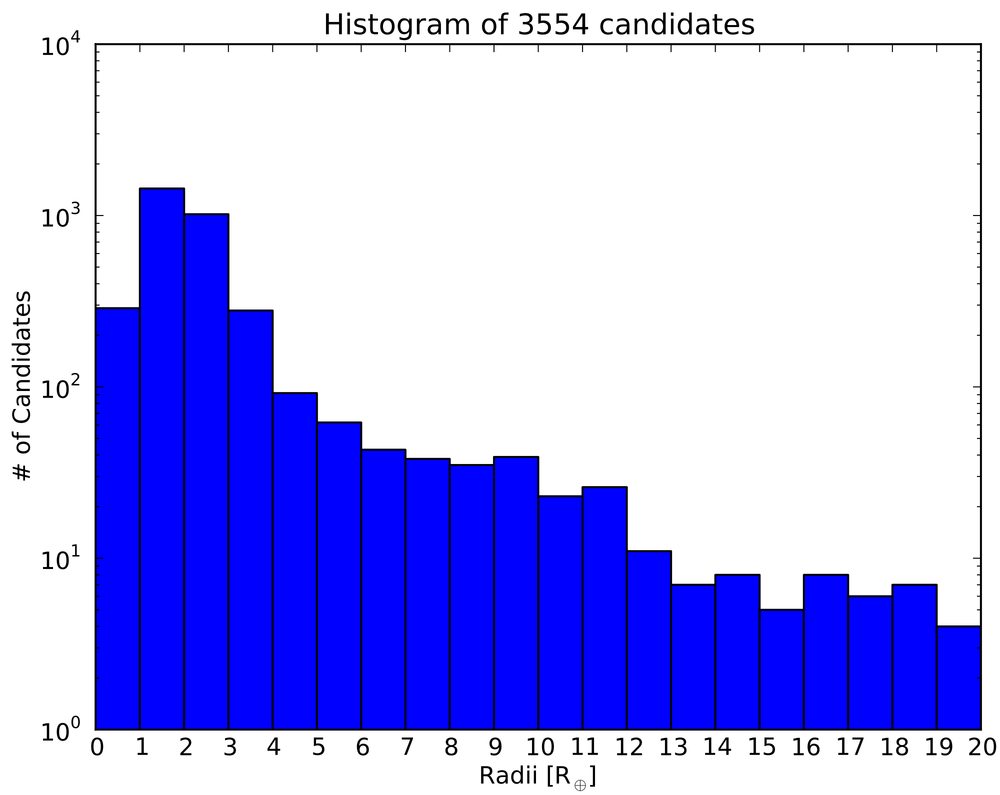

Figure 1.2: The above histogram shows the radii of all exoplanet candidates from the *Kepler* database in bins of 1 $R_\oplus$.

The figure above depicts over 3000 candidate exoplanets, which might be confirmed in the near future by other observational methods. Presently around 950 exoplanets have been confirmed, which are mainly larger exoplanets, but as can be seen from Figure 1.2, a whole new range of exoplanets is up for confirmation. The same tendency is seen for the large HARPS (High Accuracy Radial velocity Planet

Searcher) survey, which observed 376 Sunlike stars, and noticed a mass function of exoplanets extended towards low Earth masses (1-3 $M_\oplus$) (Howard, 2013, cf. Fig. 2).

At present time, a vast variation of exoplanets is observed (Wade, 2013), which have to be formed by a formational process[1]. The interior of planets has to withstand the gravitational pull due to the mass of the planet. Rocky and icy-planets, as `Earth` and `Neptune`, are in hydrostatic equilibrium by the coulomb force. The gaseous planets, as `Jupiter`, are more massive and have an internal pressure large enough that the material is in a degenerate state, thus having degenerate pressure withstanding the gravitational pull thereby keeping the planet in hydrostatic equilibrium. The critical mass of a planet that swaps between the two states of internal pressure is at ~ 2.6 M_{Jup} for a gaseous Hydrogen and Helium (H/He) planet (Zapolsky and Salpeter, 1969). But a newer model by Baraffe et al. (2008) results in a higher critical mass of 3 M_{Jup} for a gaseous H/He planet. Below this mass, the pressure by the coulomb force slightly dominates over the degenerate effects, while a mass above the critical mass are supported by more degenerate pressure.

The equation of state (EOS) describes the relationship between density, pressure and temperature for a given material in thermodynamical equilibrium. As the parameters increase towards the interior of a planet, the matter behaves in different manners. It can change states from liquid to solid, or become degenerate at large enough pressures. If the values for pressure, temperature and density for a material are known, then one might use the EOS to determine a relation between the mass and radii of a planet of that material. H/He planets that are less massive than 2.7 Jupiter masses will have a radii-mass relation of $R \propto M^{1/3}$, while more massive H/He-planets will have a relation of $R \propto M^{-1/3}$ (Zapolsky and Salpeter, 1969). More modern equation of states yield a relation of $R \propto M^{1/10}$ for a mass lower than the critical mass, while $R \propto M^{-1/8}$ for more massive objects (Baraffe et al., 2008), as can be seen in Figure 1.3 (*magenta line*).

[1]The formation of planets is still under discussion, but the two main theories are: Gravitational Instability and Core Accretion. The latter theory is strongly supported by the observations of *Kepler*

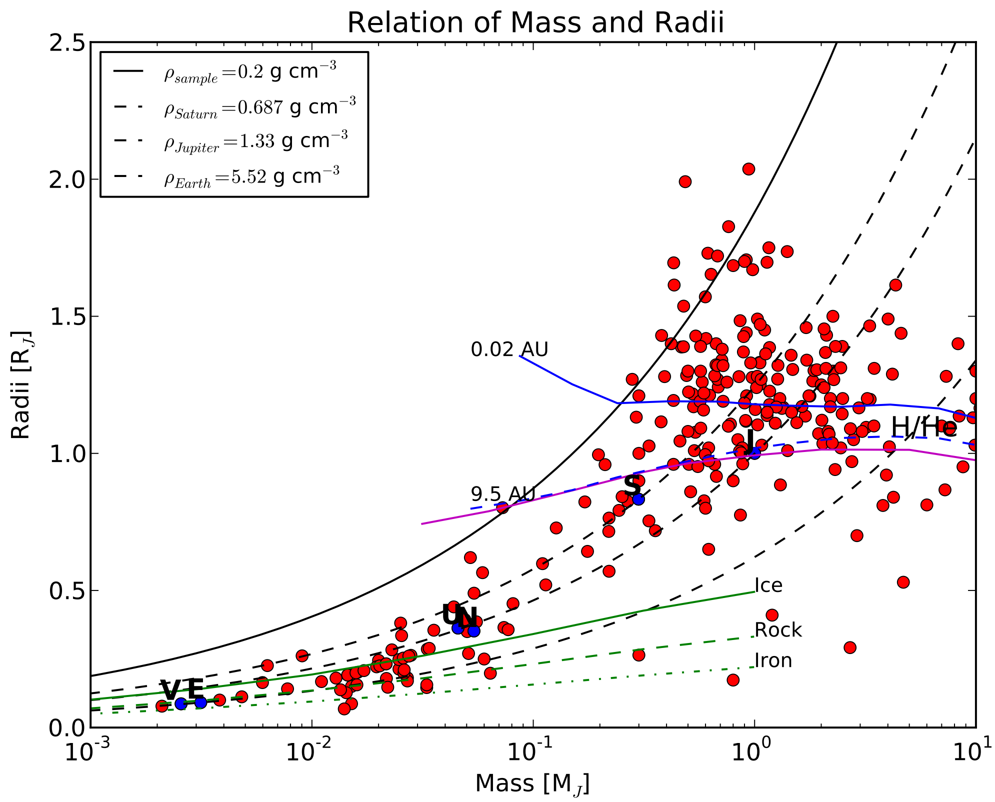

Figure 1.3: The figure depicts all the confirmed exoplanets by radii as a function of mass, both determined in Jupiter-units. The two blue lines illustrate the upper radii limit of an exoplanet which is irradiated (Fortney et al., 2007). The magenta colored line is built on a non-irradiated model by Baraffe et al. (2008). The green colored lines in the bottom are models of an exoplanet being strictly ice, rock or iron (Fortney et al., 2007). The black lines are isodensities as presented in the annotation, from left to right.

The figure depicts several interesting physical properties of the observed planets. First of all, it can be seen that Earth and Venus have an interior mixture between rock and iron to present the observed radii of the planets. Uranus and Neptune have a density similar to Jupiter, but are smaller than the gaseous giants. It is proposed that the Neptunian-planets are mainly composed of icy planetesimals in the core, and a H/He gaseous envelope, which increases the radii to the observed value (Fortney and Nettelmann, 2010). The primary effect of heavy elements, such as rock, iron and ice, in the core or envelope is to reduce the radii of the planet (Miller and Fortney, 2011).

The vast majority of the massive exoplanet can be seen by the isodensities, where gaseous giants can be tenuous as cork and hard as a terrestrial planet, as "Earth ($\rho \sim 5.52\mathrm{g\ cm^{-3}}$)". The reason that gas giants can have such a range of densities is due to the compressibility of Hydrogen (*Conference talk, Fortney and Baraffe (2013)*). It can be seen that Jupiter and Saturn have a similar radii, and behave as degenerate interiors do, according to the equation of states of Hydrogen and Helium (Baraffe et al., 2008; Fortney et al., 2007). This can as well be seen on Figure 1.3 by the magenta-colored line. The model is built on the equation of states of Hydrogen and Helium for a solar metallicity. The reason that Saturn and Jupiter are predicted to have higher metallicities than the Sun is due to the fact that they lie below the predicted radii of planets with solar abundances (*the magenta colored line*)[1].

A peculiar physical property of the exoplanets is that not many of them obey the equation of state model of Hydrogen and Helium in Figure 1.3. A lot of exoplanets are larger than the model of Baraffe et al. (2008), which assumes a non-irradiated system[2]. Most of the confirmed exoplanets are in close-in orbits, and are therefore affected by the stellar incident flux. A larger stellar incident flux will deploy an energy within the atmosphere, which will inflate the exoplanet. But, the effect of irradiation only slightly lifts the radii of exoplanets, as can be seen on Figure 1.3 (*Blue lines*).

The prediction of the stellar irradiated exoplanets model does not fit the observed radii of exoplanets, and this discrepancy raises the question of what inflates these exoplanets to such large radii?

To solve the problem, a detailed analysis has to be made of the physical properties of exoplanets. There are several parameters for an exoplanet that are hard to determine; such as the age and core mass.

The first-mentioned parameter, the age, is determined by several parameters, as will be explained in section 3.4. Within the first 200 Myr of forming a planet, the radii can becomes larger than 1.5 $\mathrm{R_{Jup}}$ depending on mass and distance. The more massive and further away a planet is the smaller its radii becomes during the formation. This can as well be seen in Figure A.4. But, observing close-in exoplanets

[1] Figure 1.3 is built on several parameters, but a full simulation of values would lift the line a bit above the radii of Jupiter, as seen in (Seager et al., 2007, cf. Fig. 4)

[2] A non-irradiated system corresponds to planets further out, like Jupiter and Saturn, which do not receive a large amount of stellar incident flux

at such an early stage has still not been done due to the low contrast between the star and planet.

The core mass is dependent on the models assumed for the interior of exoplanets. A lower core mass will allow a larger radius due to a smaller gravitational potential within the center of the exoplanet. This is the reason that the lines are mashed-up for the more massive exoplanets in Figure 1.3, since the ratio of M_{core}/M_{planet} becomes smaller (Fortney et al., 2007, cf. Fig. 5).

A core mass of zero is typically used in the literature (Batygin et al., 2011; Burrows et al., 2007) to represent an upper limit on the model. The models presented in Figure 1.3 are as well given for planets with a core mass of 0 $M_\oplus$ to give an upper limit on the radii.

The problem of inflated exoplanets is apparent from Figure 1.3, and a probable solution is a mechanism that pumps heat into the interior of a planet. Many models propose mechanisms such as tidal dissipation or enhanced atmospheric opacity, since a stellar irradiation cannot explain the inflated radii (Fortney et al., 2007). The stellar irradiation would only affect the radius of exoplanets on the level of 10% to 20% (Fortney et al., 2011a). The larger percentage is seen on the low masses of the solid blue line in Figure 1.3, because of the lower dominance of degeneracy.

There is a tendency for inflated exoplanets to be in regions with increased stellar incident flux, and several authors have found this limit to be above 2×10^8 erg s^{-1} cm^{-2} (Demory and Seager, 2011; Fortney et al., 2011b; Howard, 2013). The relation between incident stellar flux and the inflated radii is only apparent for massive exoplanets, and does not exist for Neptune-sized exoplanets.

In this thesis, I will introduce the reader to the observational techniques to measure physical properties of exoplanets in Chapter II. The Chapter will as well contain the newest information on upcoming projects based on a recent article by Bhattacharjee and Clery (2013). In Chapter III, I discuss data, which has been thought to be inflated, but could be explained by the stellar irradiated models in Figure 1.3. The data set contains two targets from the Kepler Objects of Interest (KOI), `KOI-102` and `KOI-94`. The Chapter will as well contain a discussion of the last mentioned exoplanet based on a publication by Weiss et al. (2013), with a description of false-positive detection. The latter term describes the probability of a detection being other than an exoplanet. Chapter IV is the general part of this thesis due to the KOI sample not being inflated. Here I will discuss the mechanisms behind inflating exoplanets, and add a sample of the eleven least dense-exoplanets, which are all inflated. The idea behind this choice was that the least dense exoplanets must be inflated and share similar composition. Chapter V will be a final discussion of the mechanisms and combining the knowledge gained in this master thesis, and introducing different interesting topics. I will compare two of the models received from astronomers in the field with a model of tidal dissipation, and investigate how they predict the equilibrium radii. I will as well include several ideas, which made me think during the work on the inflated exoplanets.

CHAPTER 2

Detection Techniques

Exoplanets can be detected by various observational techniques, which each have their pros and cons. A common feature in the method is that larger exoplanets, by radii and mass, are easier to detect, because they either, cover a larger fraction of the light from the stellar host, or enforce a stronger gravitational pull on the stellar host. The mentioned effects can be detected by the two methods; *transit* and *radial velocity*, which will be described in section 2.1 and 2.2, respectively. If an exoplanet is detected by both methods, then an estimate of radii and mass can be determined, which in hand gives an estimate of the density. The latter parameter can then yield information of the composition of the exoplanet. But, the measured parameters of exoplanets also depend on the measured values of the stellar host, while these depend on the resolution of their spectra and stellar evolutionary tracks (Seager et al., 2007).

Other observational techniques can provide more precise radii of stars, such as *Asteroseismology*, which can increase the precision up to 3 times compared to the spectra and stellar evolutionary tracks. This can be seen in the case of `Kepler-7b` (Demory et al., 2011, cf. Table 1). The precision required on the stellar radii is essential for a precise radii of the exoplanet, due to the linear relation between these parameters (Latham et al., 2010). The relation is also apparent in Equation Equation (2.1), since a change in flux is observed as the exoplanet transits, so a larger star will necessarily require a larger exoplanet to create the same change in flux.

This raises the question, whether the observed inflated exoplanets are due to biases of detection techniques or weakly determined stellar parameters by spectra.

This chapter will describe the five detection methods used for exoplanetary search, transit method §2.1, radial velocity §2.2, astrometry §2.3, direct observations §2.4 and microlensing §2.5. But, it will as well include a technique to determine the inclination of the exoplanets relative to the stellar spin axis, The Rossiter-McLaughlin effect §2.1.1. The technique might be essential to explain the early process of planet formation (Beaugé and Nesvorný, 2012; Triaud, 2011). A brief overview of these detection methods will be made, with a pro-and-cons, section §2.6.

All the information given in this chapter will provide the newest projects of each technique, which were published in a special edition of Science, in May-2013.

2.1 Transit Method

The first transit of an exoplanet, `HD 209458 b`[1], was detected in September 1999. The observation was used to verify that the movement of the star was indeed created by the exoplanet, since the object was first detected by the radial velocity method. More on the latter method in section 2.2.

The method requires exoplanets to be within the line-of-sight, so that a measurement of the relative flux variation of the stellar flux during the transit can be done. The variation is detected by the photometric instrument, which in turn can give an estimate of the radii due to the linear relation (Latham et al., 2010).

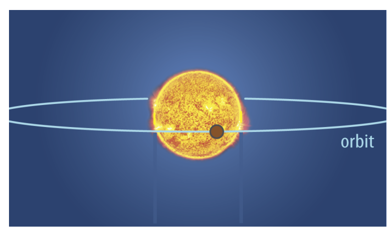

Figure 2.1: An illustration of a transit. Image taken from Howard (2013)

$$\frac{\Delta F_\star}{F_\star} \approx \left(\frac{R_{pl}}{R_\star}\right)^2 \tag{2.1}$$

Where, $F_\star$ is the stellar flux, R_{pl} is the planet radii and $R_\star$ is the stellar radii.

Transit detection can tell the observer a lot about the exoplanet and its behavior, such as its size, orientation relative to the sky and the stellar obliquity[2]. As the

[1] Parameters for `HD 209458 b`: P $\approx$ 3.52 days, $M_{pl} \approx 0.71\ M_{Jup}$ and $R_{pl} \approx 1.38\ R_{Jup}$

[2] This is the value λ which tells us how the orbital motion of a planet is relative to the stellar spin axis

exoplanet enters its occultation[1] (passage behind the stellar host) and exits through its transit (passage in front of star), but one should be careful with elliptical orbits, because exoplanets might go out of line-of-sight during the orbit (Winn, 2011). Detailed transits can indicate anomalies in the transit, which in turn might yield companions of other exoplanets in the system, as in the case of `KOI-94`.

The number of stars required to observe a transit can be calculated as $N \approx (\eta p_{transit})^{-1}$, where N is the number of stars, η is the fraction of stars having transiting exoplanets and $p_{transit}$ is the probability. The probability of detecting a transit is, $R_\star/a$ (Winn, 2011, cf. section 2.1 - 2.2)[2]. It would take over 10^3 stars to find a close-in giant at approximately 0.05 AU for a Sunlike star (Winn, 2011). The fraction of stars which should have transits is a low number ($\eta \approx 0.01$), since the transit method requires an inclination near line-of-sight, $i \approx 90°$. Space telescopes as *Kepler*therefore observe a large field of stars to ensure detection of transits.

The flux-ratio for Jupiter orbiting the Sun (at ~ 5 AU) is around 1 % and for the case of Earth, it is, 0.01 %. The capability of our detectors from ground is around 0.1 % and limited by the variable extinction of the atmosphere, while the accuracy from space can reach down to 10^{-4}% (Bhattacharjee and Clery, 2013; Papaloizou and Terquem, 2006). This means that space telescopes as *Kepler* should find terrestrial planets, as Earth. But, it should be noted that the probability of detecting a transit,$R_\star/a$, decreases with increasing semi-major axis. Long-term monitoring is required for further out transits, since at least three observed transits are required to determine a period, which is crucial before considering a detection (*private communication, Tingley (2013)*).

The advantage of transit-observations is that it is the only technique, so far, that can observe multiple stars at once. It is capable of detecting planets in all ranges but within short orbital periods, unless long observation time is applied. It suffers from the required line-of-sight condition of the exoplanets.

2.1.1 The Rossiter-McLaughlin Effect

The Rossiter-McLaughlin effect is named after its founders, who observed the behavior in binary stars, in 1924.

The Rossiter-McLaughlin (RM) effect can be described by Figure 2.2. It is a

[1] It is important to note that some authors (Faedi et al., 2013; Hartman et al., 2011) refer to occultation as a secondary eclipse

[2] The probability of detecting Jupiter at 0.05 around the Sun is, ~ 0.09

variation in the spectra of the star, as the exoplanet enters a transit. The star rotates around its stellar-spin axis, and the emitted light will therefore move towards and away from us, resulting in a blue-shift and redshift of the light. The stellar rotation will create a variation in the radial-velocity (RV) of the star. If a planet is present, then it will block out the light of the star that is shifted, thus inducing an apparent change in the measured RV of the star, as seen in the third row of Figure 2.2. This induced change in the stellar RV will be time-variable, and can inform us of the path of the transit relative to the rotational spin-axis of the star, also known as obliquity.

The RM-effect is used to investigate the obliquity of exoplanets to indicate whether the orbits are aligned or misaligned. The information of alignment can inform us of the conditions of planet formation.

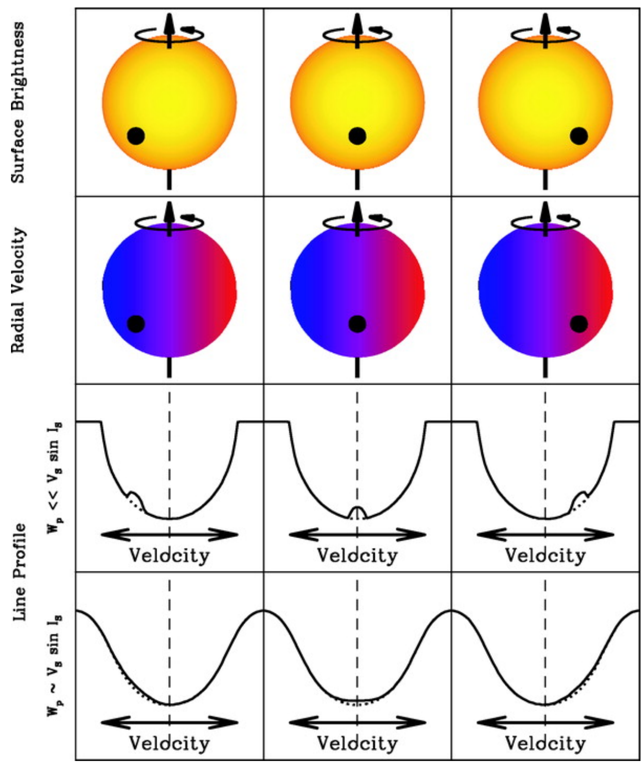

Figure 2.2: The first row depicts a transiting planet. The second row illustrates the radial velocity of a rotating star. The third row illustrates a stellar absorption line, for a case of pure rotational broadening, ignoring other affects (W_p is the net broadening, or in other words, broadening by other mechanisms), except the additional RV-bump of a transiting exoplanet. The fourth row includes other line-broadening mechanisms. Figure taken from (Gaudi and Winn, 2007)

The RM effect introduces a combined method between photometric detection and radial velocity measurements, thus enabling detection and confirmation of transits (Winn, 2011). The RM effect can yield information of the alignment of the planet relative to the star's spin axis. If an exoplanet is misaligned, as `Wasp-17b`, then a different RM-profile[1] will appear (Winn, 2011, cf. Fig. 14b), which could be due to earlier dynamical scattering, as I will investigate in section 4.2.6.

It should be noted that once the obliquity, λ, is found, one should be warrant since the stellar rotational axis might be inclined along the line of sight, thus requiring a three-dimensional obliquity, ψ (Winn et al., 2011).

2.1.2 Transit, now and near future

There are many known missions that utilize the transit method to observe exoplanets, i.e. OGLE (Optical Gravitational Lensing Experiment), COROT (COvenction ROtation and planetary Transits) and *Kepler*. The latter mentioned space telescope has had great success observing exoplanets (Borucki et al., 2010), and it has found around 50 % of all transit-detected confirmed exoplanets. It should be noted that *Kepler* has more than three thousand candidates, as seen on Figure 1.2, which have a low-false positive (Howard et al., 2012). But, Beaugé and Nesvorný (2013) notices that the false-positive estimation of the candidates is ranging between 10% up to 50%. More on false-positive will be told in section 3.3, but for now, it should be understood as a value of the probability that a detection is false, or in other words, not an exoplanet.

Upcoming plans for transit-detections include the CHEOPS (CHaracterizing ExO-Planets Satellite), which is under construction and will be sent up in 2017. Its mission is to observe the nearby stars, which have detected orbiting exoplanets. The goal is to investigate the density of these exoplanets (Bhattacharjee and Clery, 2013). Another mission is the TESS (Transiting Exoplanet Survey Satellite), which is planned to be sent up in the same year, as CHEOPS. Its goal is to observe the brightest stars in the Sun's neighborhood, in search of exoplanets ranging from gaseous to Earthlike planets in habitable zones (Bhattacharjee and Clery, 2013).

[1] A RM-profile is a (time,RV)-plot, where different radial velocity (RV) measurements as a function of time can indicate the angle, λ, between the orbital and stellar spin axis.

2.2 Radial Velocity Method

The first detected exoplanet by the radial velocity (RV) was in 1989, `HD 114762 b`[1], but at that time the detected object was considered a brown dwarf. The first confirmed exoplanet came upon the detection of `51-Peg b` (Mayor and Queloz, 1995).

In a simple case of radial velocity measurements; a two-body problem can be assumed. The mutual gravitational interaction in our two-body problem is between the stellar host and planet. The interaction will shift the center-of-mass outside the center of the most massive object, the stellar host ($M_\star \gg M_{pl}$). If the exoplanet orbit is along the line of sight, then it will cause a minor additional movement in the stellar radial-velocity, which can be detected by the Doppler shift, as seen in Figure 2.3. This motion will allow us to use the equation of motion, which enables us to solve the two-body problem, and find the radial movement of the star and companion, the exoplanet. The Radial movement will be a function of time, thus being able to yield the period. The latter mentioned value enables us to calculate the projected mass ($M_p$sini). The precise mass depends on the inclination of the orbit, and the latter parameter can be found by astrometry (Murray and Correia, 2011). The average inclination is around 65°, and an a priori probability of sin(i) to be larger than 0.5 is 87% (Lovis and Fischer, 2011).

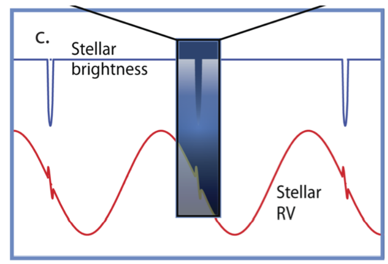

Figure 2.3: An illustration of the radial velocity during a transit, which could be seen in Figure 2.1. Image taken from Howard (2013)

The semi-amplitude of the star, K, can be described by the movement of the star in our line-of-sight. It is described by the following equation,

$$K = \left(\frac{2\pi G}{P}\right)^{1/3} \frac{M_p sini}{(M_p + M_*)^{2/3}} \frac{1}{\sqrt{1-e^2}} \tag{2.2}$$

The equation above tells us that the sensitivity is towards smaller periods and larger mass - since a higher K-value is more detectable (higher velocity-shifts). If one assumes $M_p \ll M_\star$ then Equation (2.2) can be transformed into the following,

$$K(ms^{-1}) \quad = \quad \frac{28.4329ms^{-1}}{\sqrt{1-e^2}} \frac{M_p sini}{M_J} \left(\frac{M_\star}{M_\odot}\right)^{-2/3} \left(\frac{P}{1yr}\right)^{-1/3} \tag{2.3}$$

[1]Parameters for `HD 114762 b`: P ~ 84 days, $M_{pl} \sim 11\ M_{Jup}$ and unknown radii

By using Kepler's third law, I can obtain an equation for the period, since our problem is a two-body system.

$$P(yr) \quad \propto \quad \left(\frac{a}{1AU}\right)^{3/2} \left(\frac{M_\star}{M_\odot}\right)^{-1/2} \tag{2.4}$$

Now, I insert Equation (2.4) into Equation (2.3) and obtain the semi-amplitude in terms of proximity to a star by the use of Kepler's third law[1]

$$K = \frac{28.4329 ms^{-1}}{\sqrt{(1-e^2)}} \cdot \frac{m_p sin(i)}{\mathrm{M_{Jup}}} \cdot \left(\frac{\mathrm{M}_\star}{\mathrm{M}_\odot}\right)^{2/3} \cdot \left(\frac{a}{1AU}\right)^{-1/2} \tag{2.5}$$

The equation above tells us that the further away the exoplanet is from the star, the harder it becomes to measure the semi-amplitude, because the value becomes smaller - and closer to the stellar noise and instrumental limit.

In the case of calculating the mass, I choose Equation (2.3), and isolate the mass of the exoplanet. The reason is that *Kepler* provides high precision measurements of the period. The period could also be found by my radial-velocity measurements, which typically span over several transits.

$$m_{pl}\ sini = \frac{K\sqrt{1-e^2}}{28.4} \left(\frac{M_\star}{M_\odot}\right)^{2/3} \left(\frac{P}{1yr}\right)^{1/3} \tag{2.6}$$

Since, I am going to work with the radial velocity in the upcoming chapter; a brief overview of the terms in Equation (2.3) is made.

- The first term requires an eccentricity, which can be found by detailed photometric measurements and by multiple spectroscopy observations. The latter mentioned gives a weaker constraint on the eccentricity, while a timing of the secondary eclipse gives a stronger constraint on the eccentricity (Miller et al., 2009).

- The second term requires the exoplanet mass and inclination, where the latter is impossible to find without astrometry. The exoplanet mass is the value, which I wish to find, but due to the additional $sin(i)$ -term, an estimated mass is achieved. So, my estimations are always the lower limit, since a exoplanet will always lie on the line-of-sight, so $i = 90°$, thus $sin(i) = 1$.

[1] Kepler's third law states the following proportionality, $P^2 \propto \mathrm{M}_\star{}^{-1} a^3$

- The third term is the total mass of the system, but since the stellar mass is usually 10^3 larger, it allows me to disregard the mass the exoplanet, m_2. The stellar mass can indirectly be found by spectroscopic analysis, photometry, parallax measurements and comparison with stellar evolutionary models (Lovis and Fischer, 2011). This will as well be seen in section 3.4.4.

- The last term is the period, which can be detected by the transit method with a high precision of 10^{-6} days, as seen in our data set, Chapter 3.

The problem of inclination is an important limitation of the RV technique, because a small inclination could increase the mass of the exoplanet, so wrong mass would be achieved. But theoretically the probability that sin(i) is larger than 0.5 is 87% (Lovis and Fischer, 2011).

Modern methods can measure radial velocities down to 1 m s^{-1}, but the problem is the orbital period. Jupiter induces a radial velocity of 11 m s^{-1} on the Sun, but because of its distance of $\sim$ 5 AU, it has an orbital period of $\sim$ 12 years, which means that an observation requires at least 24 to be sure of a planetary orbit.Earth would induce a velocity of 0.1 m s^{-1}, which is too small and would be mixed into the stellar jitter, also called stellar noise. This term will be described in section 3.3.1. The technique is, as described, primarily for massive exoplanets at low orbital periods. Radial velocity measurements are as well limited by the brightness and stability of the stars, thus best for FGKM-stars (Kalas, 2011). The technique does not require major instrumental improvement, but just an extremely sensitive spectrometer and lots of time.

2.2.1 Measuring radial velocity

The radial velocity technique depends on the detection of the well-known Doppler effect. The effect is introduced due to a moving emitting source, which emits spectral lines at different wavelengths. The shift in wavelength is due to the Doppler shift, and can be measured by the numerous spectral lines that are present in a stellar spectra. The width of the lines can then be transformed into a radial velocity, which is a function of the semi-amplitude, as described in Equation (2.2). But, obtaining an absolute radial velocity through the Doppler effect is a though task, due to several systematic effects, as; gravitational redshift, line asymmetries, calibration systematics, etc. (Lovis and Fischer, 2011).

Stars radiate mostly between the UV and mid-IR domain, but emissions in the UV and mid-IR domain are hard to detect by ground telescopes due to the atmosphere of Earth. Therefore most measurements are focused on FGK-stars which emit most their light in the optical spectrum, alike our Sun. The most governing property of a spectrum is the effective temperature of the star (Lovis and Fischer, 2011), thus creating different spectra for different stellar types.

- OB - stars ($T_{\text{eff}} \geq 10000$ K) will have all their elements being partly or fully ionized, thus having line opacities that will be negligible in the visible and near-IR spectrum (*Only a continuum will appear*). Another problem concerning warm stars is the rotational broadening; which broadens the intrinsic widths of lines. But it can be avoided, when the stars reach the Red Giant Branch (RGB) and RGB-clump stages, where the effective temperature and the rotation decline. The declined temperature will move the spectrum to a redder part, thus moving the spectral lines towards the visible spectrum and a declined rotation will sharpen the lines.

- Cool stars ($T_{\text{eff}} \leq 3500$ K) have more packed spectral lines, less contrasted and more overlapped due to presence of complex molecules. One problem, from an instrumental point of view, is their low optical luminosity, which makes it difficult to reach a high signal-to-noise (SNR), and the main spectral regime being in IR puts a constraint on the instrumentation. As seen in section 2.2.2, the uncertainty of our radial velocity measurement is inversely proportional to the SNR.

Increasing the amount of measured lines will increase the precision of the radial velocity, but some lines are useless, as H α- and Ca II H and K lines, which are strongly saturated, thus giving broad wings, which raises the problem of line asymmetry. The preferred lines for FGK stars are the Fe-lines, which are numerous, thus necessary for high precision of Doppler shift measurements.

2.2.2 Precision of Radial velocity

The precision depends on three parameters; signal-to-noise ratio (SNR), the depth and the width of the spectral line. If a Gaussian shape for a spectral line is assumed, then the following equation may be applied for the precision,

$$\sigma_{RV} = \frac{\sqrt{FWHM}}{C \cdot SNR} \tag{2.7}$$

Where, FWHM, is the full-width half maximum of a spectral line, SNR is the signal-to-noise ratio in the continuum, and C, is a the depth level divided by the continuum level, which can also be described as, C$\sim$ 1/FWHM. The equation above tells us that the precision will be best for a line that is narrow (low FWHM) and steep (C becomes large).

Another factor that affects the precision is the activity of the star due to its cyclic variations. Older stars are preferred due to their slower rotation and more calm nature than young stellar stars. The rotation of a typical young Sunlike star would be around $\sim$ 1-2 days, while at its "present" age of 5 Gyr, it has a rotational period of 20 - 50 days, thus better for radial velocity measurements (Lovis and Fischer, 2011). Other stars have no cyclic variations, which could be due to being in a Maunder-minimum state[1] and these stars are favorable for Doppler measurements, due to high precision of measurements.

In principle, all measurements will contain some noise (jitter) due to the cyclic period of stars or stellar activity. This jitter-term will be described in more detail in Chapter 3.

Young stellar objects and those at the end-off Main Sequence will have larger jitter due to a more violent stellar surface, while older GK-stars will remain calmer, thus lower jitter. Stellar lines as H α and Ca II H & K with the broadband photometry can indicate the chromosphere activity (Martínez-Arnáiz et al., 2010).

2.2.3 Radial Velocity, now and near future

All telescopes can have spectrometers attached to them, and be used for exoplanet detection, but the two major spectrometers are; the High Accuracy Radial velocity Planet Searcher (HARPS) at a 3.6 m telescope at La Silla, Chile and the HIgh Resolution Echelle Spectrometer (HIRES) on the 10 m Keck I telescope at Hawaii.

The projects in the near future are; the Automated Planet Finder, which resembles HIRES, but its primary goal is to detect exoplanets. It will obtain 25 spectra per night (Bhattacharjee and Clery, 2013).

The trend of detecting exoplanets with radial velocity has been moved from detection of exoplanets to confirming candidates, due to *Kepler*'s large amount of detections. Therefore has a similar spectrometer to HARPS been mounted at a 3.6 m Telescope at the Canary Islands to observe the same patch of Sky, as *Kepler* did.

[1] A state where stars seem to be very quiet, thus having low activity level and showing no cyclic variations. It appears to around 10 - 20% old stars

2.3 Astrometry

Astrometry is an observational technique where an observer is looking at the movement of a star. To investigate the movement of a star requires an extreme accuracy, because of the large distance to the objects. Astrometry has been proposed to detect "unseen companions" since 1855, but still no exoplanet has been confirmed with the method (Bhattacharjee and Clery, 2013). According to the *exoplanet.eu*, a discovery of `HD 176051 b` has been made by Astrometry, but this disagrees with the database of Open Exoplanet Catalogue (Rein, 2012), which instead proposes its discovery by radial velocity. The reason for this discrepancy could be that in the year of the planets discovery, a group of astronomers proposed a detection, while being confirmed later on by radial velocity.

Astrometry depends on measuring the angular motion of the star with an interferometer, as seen on Figure 2.4. It requires a large amount of statistics as seen on the figure by the dark filled circles. An example of bias could be uncertainty in the kinematics of the system. Astrometry is usually used to estimate parallax distances for stars in the Milky way. The benefit of astrometry is its disregard of inclination, thereby enable to spot exoplanets not detectable by transit and radial velocity.

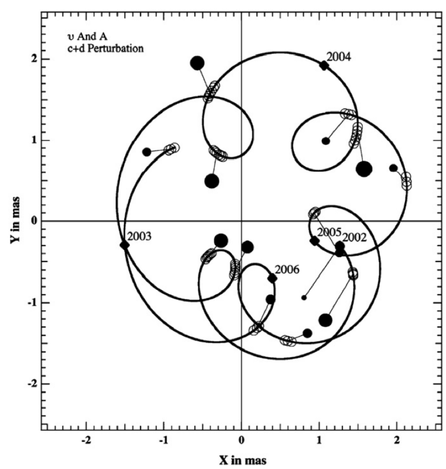

Figure 2.4: An illustration of Astrometric reflex motion of ν `And` and its planetary companions. The astrometric orbit is shown by the dark line, the open circles are the observations with dark circles indicating the amount of observations. The observation is taken over 4 years (from 2002 - 2006). Image is taken from McArthur et al. (2010)

Jupiter affects the motion of the Sun, and this motion can be resolved in arcsec. If I move to a distance of 10 pc from our solar system, then the variations of stellar motion due to Jupiter would be 500 μarcsec, while interferometers resolve down to 1 marcsec, thus making a detection of Jupiter, from 10 pc, impossible.

Even though, Astrometry has not yet confirmed any exoplanets, it is a valuable tool to radial-velocity, since it can find the real mass of exoplanets by the inclination of the orbital motion. Another feature that it has, is the independence of spectral type or rotation of a star. But, it is a very time-consuming method, thus being normally used in combination with other techniques to find a value of the inclination.

2.3.1 Astrometry, now and near future

The launch of GAIA will have a resolution of 2 - 10 μarcsec, which will enable a large detection of exoplanets (Papaloizou and Terquem, 2006). The mission will be able to observe 1% of our galaxy with a goal of finding tens of thousands exoplanetary systems (Bhattacharjee and Clery, 2013; Tingley, 2013).

2.4 Direct Imaging

Direct imaging has detected its first exoplanet in, 2004, `2M1207 b`[1]. A detection of an exoplanet requires a strong luminous source and a large distance from the stellar source. The latter mentioned case can be seen in the case of `Fomalhaut b`, where an exoplanet is detected at a distance of 177± 67 AU.

The luminosity of the exoplanet needs to be larger than a millionth of its stellar host to be detected in optical light. This factor is not a constant value, but varies with the angular distance from the star, and distance to the observer. A useful method to reduce the contrast between the luminosity, of the star and planet, is by coronography and nulling interferometry (*private communication, Tingley (2013)*).

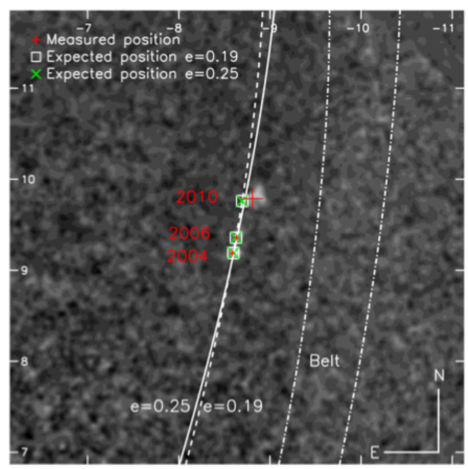

Figure 2.5: An image of `Fomalhaut b`'s movement with predicted orbital eccentricities. Imaged by Hubble Space Telescope, and figure from (Galicher et al., 2012)

The benefit of direct imaging is receiving the temperature of the exoplanet at a given wavelength, which can be calculated into an atmospheric temperature given a certain atmospheric model. And it does not suffer from sensitivity on period of the orbit as the transit and radial velocity methods. A mass can as well be determined by thermal evolution models, which predict the luminosity and spectrum with time (Fortney et al., 2011a). But, these predictions of mass

[1]Mass of 4M_{Jup}, semi-major axis of 46 AU

are typical very uncertain (Galicher et al., 2012), as for `2M 1207 b`, having a mass of $4^{+1}_{-6}\mathrm{M_{Jup}}$ according to exoplanet.eu.

But, the strength of the mentioned techniques is the weakness of direct imaging, since the closer an exoplanet is to its host star, the harder the detection of the exoplanets' luminosity. The important factor of direct imaging is the observation of exoplanetary atmospheres, since it is based on photometric instruments, as the transit-method. It might as well be the only technique that can yield information about the initial conditions of planet formation in young stellar objects (*Conference talk, Fortney and Baraffe (2013)*).

Direct imaging only suffers from the instrumental technology and therefore preferred for detecting exoplanets with a very large period and in young stellar objects.

2.4.1 Direct imaging, now and near future

The only space-telescopes, which can be used for imaging, are the Hubble Space Telescope (HST) and Spitzer Space Telescope (SST), which observed `Fomalhaut b`, as seen in Figure 2.5. The future looks a bit dark in this sector, since observations from ground-based telescopes are limited by the atmosphere, and both space-missions[1] have been dumped (Bhattacharjee and Clery, 2013). But, two attachments will come into work later this year at the Gemini south telescope and the SPHERE at the European Southern Observatory's Very Large Telescope (VLT). They will increase our sensitivity of detection by a factor of ten. Their goal will be to investigate nearby young stellar systems, because of the high temperature of exoplanets due to early formation. They will as well work in infrared, since exoplanets appear brighter and stars dimmer, compared to visible light.

2.5 Microlensing

Microlensing detected its first exoplanet in 2004, `OGLE235-MOA53 b`[2], as seen on Figure 2.6. The technique is based on the gravitational lens effect - which is one star passes in front of a brighter background star, where the foreground star will act as a lens, thereby brightening the background star up to a 1000 times. The lensing will occur differently when a smaller companion is attached to the foreground star. This

[1]The space missions were called Terrestrial Planet Finder and Darwin with mirrors the size of the Hubble Space Telescope (2.4 m)

[2]Parameters for OGLE235-MOA53 b: Mass, $2.4\mathrm{M_{Jup}}$, Semi-major axis, 5.1 AU

lensing effect can be seen at the light curve since the exoplanet will perturb it, creating two successive spikes of brightness, as seen on Figure 2.6. The gained information can then be transformed into a mass and distance determination (Bhattacharjee and Clery, 2013).

This method is most sensitive to exoplanets at a separation $\sim$ 1 - 5 AU from the lens star, and can, by rough assumption, disregard exoplanet size. Another benefit of the gravitational lensing is that it disregards range, since the mentioned exoplanet, `OGLE235-MOA53 b`, was found at the range of 5.2kpc, which is a lot further than any other method can detect. The disadvantage is the rarity of microlensing with no possibility of double-checking.

The method is mostly used to constrain stars containing exoplanets, and a 5 year analysis of PLANET photometry indicated that 33 % of M-dwarfs could be harboring Jupiter-mass companions within a distance of 1.5 - 4 AU (Papaloizou and Terquem, 2006).

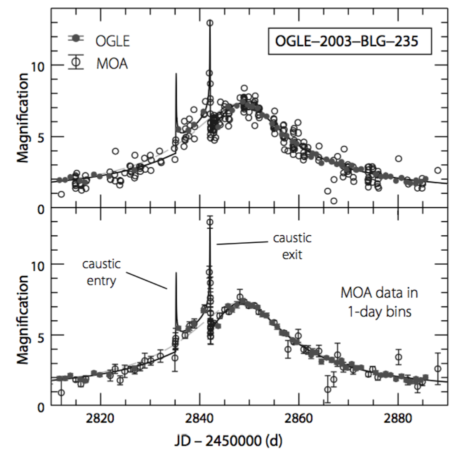

Figure 2.6: The above figure depicts `OGLE-2003-BLG-235` or `OGLE235-MOA53`, as it gets lensed by a background star. The lensing lasted 80 days during 2003. The figure is taken from Perryman (2011).

2.5.1 Microlensing, now and near future

One of the telescopes used for microlensing is the Optical Gravitation Lensing Experiment (OGLE), 1.3 m, which has at first been used to search for Dark Matter, but became more of a planet-hunting tool. The largest mirror used for gravitational lensing is a 1.8 m telescope, Microlensing Observations in Astrophysics (MOA).

No plans are mentioned in the near future in Bhattacharjee and Clery (2013), but to increase the potential of gravitational lensing, a network of telescopes has to be put in place, since these events can appear rapidly. As an example, the SONG project could be mentioned, which is going to be a network of 1 m telescopes spread out on Earth. Gravitational lensing does not require instrumental advances, other than the time of observation.

2.6 Overview of detection techniques

In this section, an overview is given of the detection-techniques, which were just mentioned. The Table gives an overview of which methods are necessary for further investigation of exoplanets. The table is presented in a ”pros and cons”-style.

Detection method	
Transit	The method has been a invaluable for detecting all different kinds of exoplanets due to the space telescope, *Kepler*. It has been crucial for determining radii by light curves and thereby enabling a measure of density with a mass-determining method. The inclination is a smaller problem of the method, since a transit will occur as the planet is aligned on the line-of-sight, so the inclination is almost edge-on. The problem arises by eccentric orbits, which can be inclined (*private communication, Tingley (2013)*). The transit gains by being able to observe multiple stars simultaneous with a great distance from us than radial-velocity (Papaloizou and Terquem, 2006).
Radial Velocity	Radial velocity is strongly biased towards larger masses and smaller periods. But, HARPS has proven to be extremely efficient in finding smaller exoplanets with their enhanced methods. It is sensible to the inclination of the line-of-sight. The methods disadvantage is its range, $R_{detection} \lesssim 100$ pc (Papaloizou and Terquem, 2006), and the time needed for observations.
Astrometry	Astrometry can detect all types of exoplanets, but suffers from a range-problem and required time used for detection. But, it can aid radial velocity measurements to obtain an exact mass by finding an inclination.
Direct Imaging	Direct Imaging is essential for receiving temperature and spectra of exoplanets, but suffers from a range problem, since it relies on instrumental progress. The exoplanet detection relies on the contrast with the stellar system; as in, luminous exoplanets around dim stars are easier to detect.
Microlensing	Microlensing has the major advantage due to the lensing effect. It suffers from the rarity of events and the period of events. The exoplanets are hard to confirm due to lack of other detection methods at same distance and the short appearance of the lensing effect.

Table 2.1: An overview of the different detection techniques from Chapter 2.

CHAPTER 3

Data sample

In the following chapter, I introduce two data samples of radial-velocity measurements taken from spectra obtained from the Nordic Optical Telescope (NOT). These measurements were made available by my former supervisor, Lars Buchhave. The targets are candidates from the Kepler Objects of Interest (KOI), system; `KOI-94` and `KOI-102`. The observations from NOT were taken in a time span of 2 years, from 2009 to 2011. The analyzed spectra are then transformed into data files comprised of; the heliocentric Julian date (HJD), radial velocity, error estimation, and signal-to-noise ratio. Every dataset of radial-velocity measurements contains a template value, which is when the exoplanet is at the side of the star. At this point, the radial velocity measurement from the spectra of the star will only contain information of the star, itself. This radial velocity measurement then becomes a template, which all radial-velocity measurements are subtracted by. The procedure was preformed by Lars Buchhave and ensures that the signal is not related to the star itself.

I apply a fitting procedure to each dataset, where I present three crucial items; (I) parameters, (II) error estimates on the parameters and (III) the goodness-of-fit, also known as chi-squared (Press et al., 2007, cf. section 15.2). The last value determines how well the model fits the data. A general rule-of-thumb is that if the goodness-of-fit approximates the degrees of freedom then the fit is good[1]. More detail is available in section, §3.1, while the results are discussed in §3.2.

[1] $\chi^2 \approx \nu$, where $\nu = N - M$; ν is the degrees of freedom, N is the number of measurements, and M is the number of adjustable values

A minor introduction is made to the reliability of the results of Kepler Objects of Interest (KOI). As earlier mentioned, the false-positives of the catalogue is currently debated (Beaugé and Nesvorný, 2013) and an introduction to its sources is presented in §3.3. It is important to notice that the jitter that I apply in the analysis is described in section 3.3.1.

A brief overview of the determination of each stellar parameter[1] is presented to indicate where the uncertainties lie. These determinations are found in §3.4.

3.1 Analysis

The data analysis of the radial velocity data is performed as soon as the data is extracted from the spectra. The required information is the time of observation, the radial velocity measurement and the occultation event or transit event. The time of observation in astronomy is typically given by the heliocentric Julian date (HJD), and it needs to be transformed into the position of a planet during its orbital phase for further analysis. This transformation requires an occultation event; when the exoplanet is at the side of the star (Phase = 0), and a period. Both of these values are observed with high precision by the *Kepler* space telescope. The high precision can be seen on the amount of decimals given in table 3.1 and 3.2.

In the analysis, I choose to use two fitting procedure, a simple least squares fit and a Markov Chain Monte Carlo (MCMC) based on (Foreman-Mackey et al., 2013). I use the second procedure to ensure that there isn't any multiple solution for the semi-amplitude. The idea was proposed by my former supervisor, Lars Buchhave, to be confident in the results yielded by the fitting procedures.

The main difference is that the least squares fit tries to find the best matching fit to the data sample, while a Monte-Carlo based simulation tries to investigate how random iterations can form the certain fit. A simple sinusoidal function is applied for both of the fitting procedures to estimate the semi-amplitude, Equation (2.3) at page 14. It should be noted that in the following I assume circular orbits, $e = 0$, because it eases the fitting procedure (allowing a sinusoidal function, $v_{rad} = K \cdot sin(t)$). It is as well valid for close-in massive exoplanets, as seen on Figure A.5. A variable eccentricity would complicate the function to fit, and a simple sinusoidal function cannot be assumed.

[1] Age §3.4.1, T_{eff} §3.4.2, log $g_\star$ §3.4.3, $M_\star$ and $R_\star$ §3.4.4, and at last, the radial velocity, v_{rad}, §3.4.5

In the first method, I investigate what chi-square tells me about the data and how I can achieve a perfect chi-square, or get a reduced chi square to a unity. The latter term is just the chi-square divided by the degrees of freedom, as described in the first footnote in the introduction of this Chapter. Chi-square is described by the following equation,

$$\chi^2 \equiv \sum_{i=1}^{N} \left(\frac{y_i - y(x_i; a_1 ... a_M)}{\sigma_i} \right)^2 \tag{3.1}$$

$$\chi^2_{reduced} = \frac{\chi^2}{\nu} \tag{3.2}$$

In the Markov Chain Monte Carlo (MCMC) method I investigate what the acceptance fraction is; if the value, `a`, equals one, then all the proposed values in the MCMC-simulation are accepted, while a value equal 0 indicates that everything was rejected. It is recommended that the acceptance fraction, `a`, lies between 0.2 and 0.5 (Foreman-Mackey et al., 2013).

In my MCMC simulation, I apply 10^7 free parameters, or 1000 walkers and 10000 runs[1]; the walkers determine the spread of the guess, while the number of runs applies how many times each walker should be iterated.

3.2 Results

In the following section, I will show the results achieved by doing the analysis described above. I will briefly explain the results of `KOI-102`, while a deeper comparison will be made for the case of `KOI-94`, due to newer observations (Weiss et al., 2013).

3.2.1 KOI-102

The received data might not have been completely up to date with the Kepler Input Catalogue (KIC), therefore a check up has been made, and a secondary companion has been found. The KIC can contain errors , so a checkup is advised using the Kepler Community Follow-up Observing Program (CFOP) (Tingley, 2013). Both catalogs, KIC and CFOP, agree on the system having a secondary companion. The

[1] http://dan.iel.fm/emcee/

catalogs include information regarding the stellar properties, which point towards a Sun-like star, a young G2V star.

	`KOI102` Received	`KOI102` Updated	
Name:	K00102.01	K00102.01	K00102.02
Period [*days*]	1.7351363	1.73513627	1.19000006
$R_{pl}[R_\oplus]$	3.704	3.63	1.19
T_c [HJD]	2454968.05914		
Age [Gyr]	...	2.5 ± 1.5	
$R_\star$ [$R_\odot$]	...	1.079	
$M_\star$ [$M_\odot$]	...	...	
[Fe/H]	...	...	
$T_{\rm eff}$ [K]	...	5838	

Table 3.1: Parameters of the system, `KOI102`. T_c is the transit event. The received-subscript is the information received from my former supervisor the 27/2-2013. Updated values are taken from the Kepler Input Catalogue (KIC)[1]. Unmeasured parameters are defined as, ... All values are taken from 5th of March 2013.

The system contains two exoplanets, with the largest exoplanet being a Neptunian size[2]. The information provided by KIC tells us that the stellar system looks like ours, just younger, with an age of 2.5 ± 1.5 Gyr. To calculate the proximity to the stellar host, I need the period of the exoplanet and mass of the star and exoplanet, as seen in Equation (2.4)[3]. The two latter values are unknown, but the mass of the exoplanet can be estimated by fitting the radial velocity data, and the mass of the star can be estimated to $1M_\odot$, since the host star, `KOI-102`, is similar to the Sun.

The radial velocity data is fitted in figure 3.1 by the least squares fit procedure. The lower plot is the residual scatter, which is the data points subtracted by the fit. More information on the use of this residual, also known as bisector span, will be given in section 3.3.1.

[1]http://archive.stsci.edu/kepler/kic.html

[2]The radii of Neptune is 3.8 $R_\oplus$

[3]The equation does not include the mass of the planet, since it is 2-3 orders lower than the stellar mass

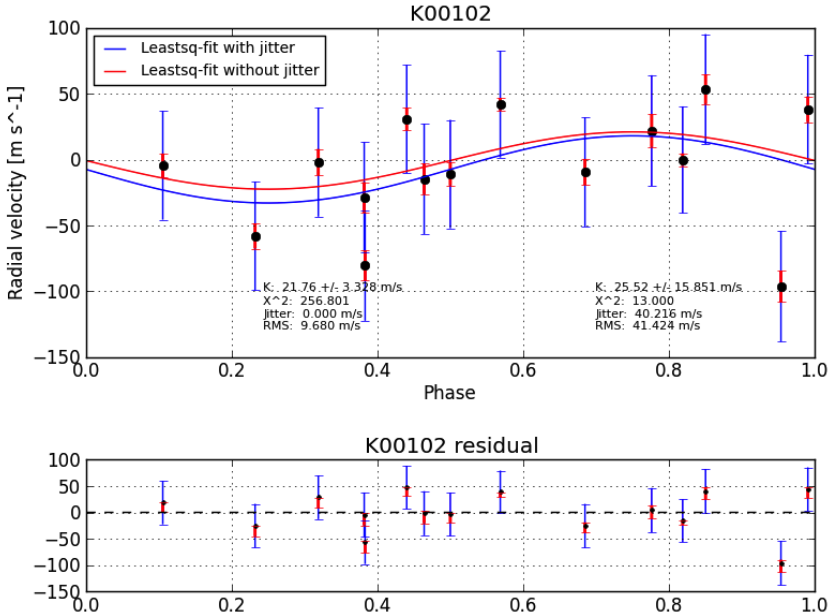

Figure 3.1: Our data plotted with an amplitude of 25.518 ± 15.852m s^{-1} for an enforced reduced chi-square of 1, while a fit without any jitter yields a lower amplitude of $21.76\pm$ 3.328 m s^{-1}

The plot above illustrates two conditions of the data sample; red and blue, which correspond to a fit without and with jitter. This can as well be seen by the corresponding colored errorbars, since the errorbars with jitter are larger. The jitter-term is explained in more detail in section 3.3.1[1].

The red case is where the data is fitted raw, which results in a large chi-square, which combined with the degrees of freedom, gives a large reduced-chi-square. This indicates that our fit has not captured the dataset, due to the uncertainty on the radial velocity. The root-mean-square of the errors is almost half of the amplitude, which as well indicates the large uncertainty of the result.

In the blue case, I assume that there is a jitter, which increases the errorbars of the raw data. I add noise to ensure a perfect chi-square on the background that the star could produce additional noise. Our root-mean square of the errors increases as well, due to the added noise, and exceeds the amplitude, thus indicating that even a "perfect" fit yields a non-realistic result.

[1]The reader should understand jitter as a term of noise, which is produced by the stellar activity. It is largest for active stars, and lowest for older stars.

I can conclude that within a 99,7 % confidence level, or 3σ, that the minimum mass limit is below $0.19\mathrm{M}_{\mathrm{Jup}}$ by the use of Equation (2.6). This value is obtained by taking the jitter-free case, and adding the jitter would increase the minimum mass limit to $0.42\mathrm{M}_{\mathrm{Jup}}$.

The MCMC shows same result as the least squares fit, and no signs of other peaks. This means that no other solutions have a local minimum.

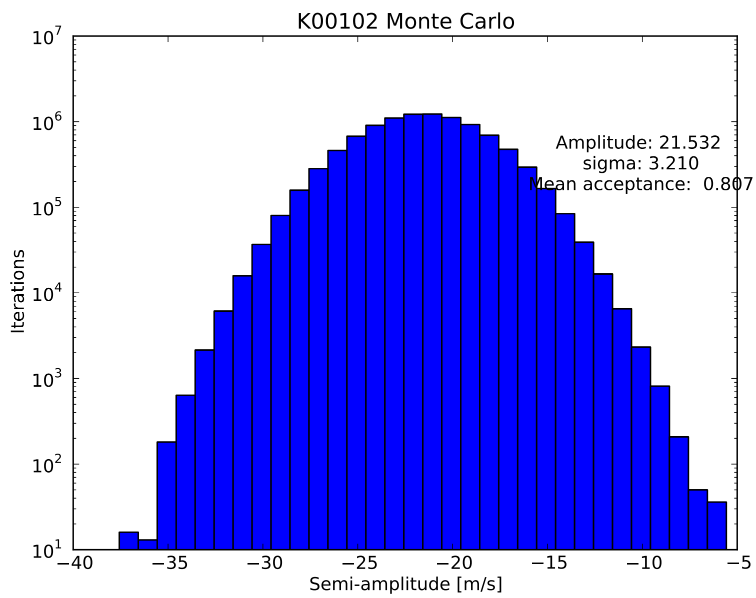

Figure 3.2: The MCMC result of 10^7 iterations is illustrated by a logarithmic scale along the y-axis with the iterations, and the semi-amplitude along the x-axis. The semi-amplitude is calculated to 21.532 ± 3.21 m^{-1}.

The acceptance fraction is 0.807, which indicates that too many iterations are accepted, thus emphasizing the uncertainty of our semi-amplitude guess. Figure 3.2 shows that the MCMC method and least squares fit are nearly identical, and the difference in amplitude is around 0.2 m s^{-1}.

The conclusion of `KOI-102` is that there might be a exoplanet with a mass of 0.129 $\pm$ 0.02 $\mathrm{M}_{\mathrm{Jup}}$, and within 3σ; it is possible to conclude that the minimum mass must be below $0.19\mathrm{M}_{\mathrm{Jup}}$ or $60\mathrm{M}_{\oplus}$. The result including jitter is highly unlikely due to the calm nature of the star. It should be noted that the mass achieved is by assuming that the system is composed of one exoplanet. The assumption is good enough due to the smaller companion being Earth-like, thus less massive by a factor of ten[1]. The assumption made of the system being a single-planet system will be discussed in Chapter 5.

3.2.2 KOI-94

The `KOI-94` system is composed of four exoplanets, which vary from Earth-like to Jupiter sizes. The parameter list is given below, in table 3.2. In a multiple exoplanet system, more measurements with higher precision are necessary to detect the smaller exoplanets, so in our case, I assume that the measurements in our data are produced by the largest exoplanet, `K00094.01`. This assumption is acceptable, since the semi-amplitude depends on the mass of the exoplanet and its period (2.2), and in this case; the larger exoplanet should have an order higher mass than the companions.

The information from the KOI-catalogue indicates that the exoplanets orbit around a F8 star with a temperature of 6184 K. It is a bit older than `KOI-102`, with an estimated age of 3.13 ± 0.41 Gyr. The stellar radius is 1.52 $R_\odot$, which could indicate a star towards the end of the main-sequence.

[1]Neptune is $\sim$ 15 times more massive than Earth

	KOI94			
Name :	K00094.01	K00094.02	K00094.03	K00094.04
Name: (Weiss et al., 2013)	KOI -94d	KOI-94c	KOI-94e	KOI-94b
Period [$days$]	22.34300041	10.42370701	54.31993103	3.74324489
$R_{pl}[R_\oplus]$	9.259±0.016	3.436± 0.016	5.48± 0.018	1.411± 0.026
Updated	11.39999962	4.21999979	6.73000002	1.73000002
T_c [HJD]	2454965.74047100			
Age [Gyr]	3.13 ± 0.41			
$R_\star$ [$R_\odot$]	1.51999998			
$M_\star$ [$M_\odot$]	1.277±0.05 (Weiss et al., 2013)			
[Fe/H]	+0.0228 (Weiss et al., 2013)			
$T_{\rm eff}$ [K]	6148			

Table 3.2: Parameters of KOI-94: T_c is the time of transit, which is needed to calculate the phase. Values are taken from the Kepler Input Catalogue (KIC). Values are from 5th of March 2013. Additional information about the system was taken from a recently published paper, and is referenced in the table.

I preform same procedure as for KOI-102, introducing a least squares fit plot, with a plot of the residual-values.

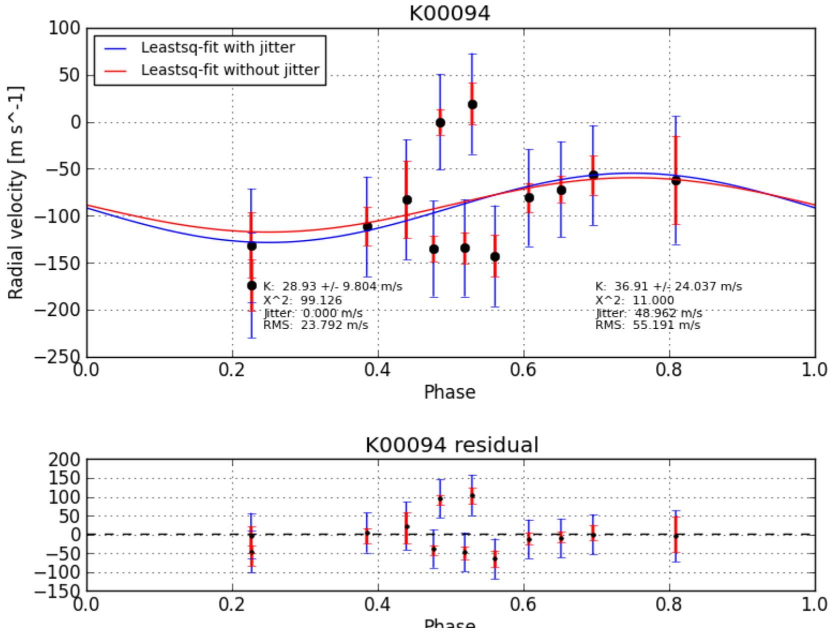

Figure 3.3: A least squares fit of the system `KOI-94`, but only `K00094.01` should inflict a large semi-amplitude due to its larger size, and therefore mass.

It is clear to see that there are 6 outliers for the raw data, while the data set including jitter has only 3 outliers, due to the larger errorbars. The chi-square value is smaller than in the case of `KOI-102`, which is probably due to the larger RMS of the data. The whole fit is placed lower than the template value than in the case of `KOI-102`. It might indicate that the template value is determined for a case, where all the exoplanets in the system pull the star away from us, causing it to redshift. It can be seen that the distribution of data in this plot is widely spread, which could be due to the larger exoplanet, `KOI-94d`, not being the dominant source of semi-amplitude in the system. This can especially be seen in the residual plot. This would be the consequence of a lower period-mass ratio, as can be noticed in Equation (2.2)[1] . It is known that `KOI-94d` has the second largest period in the system, and the period will slightly reduce the dominance on the semi-amplitude, K. I will investigate this dominance in section 5.4.

The results are checked with a MCMC simulation, which shows the following figure,

[1]The semi-amplitude, K is proportional to the period and mass; $K \propto P^{-1/3} M_{pl} \mathrm{M}_{\star}{}^{-2/3}$

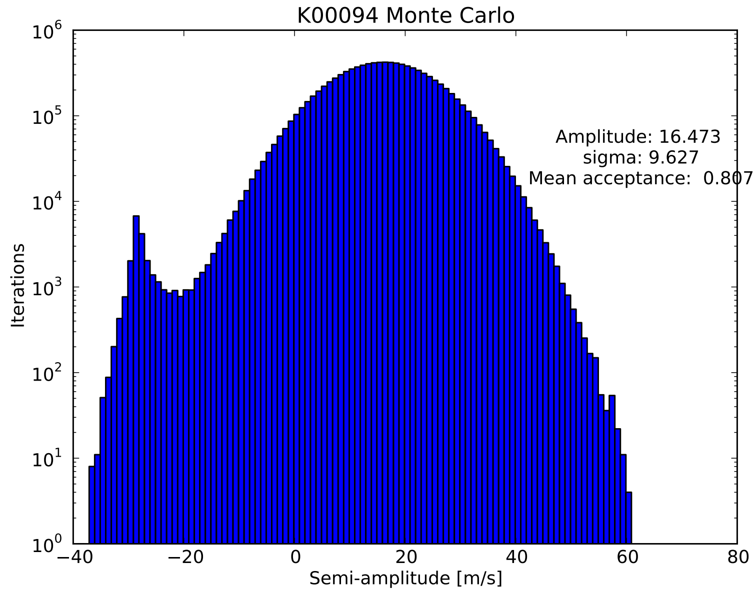

Figure 3.4: The MCMC result of 10^7 iterations is illustrated by a logarithmic scale along the y-axis with the iterations, and the semi-amplitude along the x-axis. The semi-amplitude is calculated to 16.473 ± 9.63 m^{-1}.

In section 3.2.1, I noticed that the MCMC and least squares fit yielded more or less the same amplitude. In this case, the difference is almost 12 m s^{-1}. The reason for this shift could be the number of iterations ran by the MCMC, since a larger number would give a larger semi-Amplitude.

I tried to run the simulation multiple times with the result that less runs with more walkers resulted in a similar amplitude to the least squares fit, 28.061m s^{-1} (10 runs, 1000 walkers; acceptance fraction: 0.910), while an opposite case of less walkers but more runs resulted in 13.860 m s^{-1} (1000 runs, 10 walkers; acceptance fraction: 0.798). If the walkers or runs were multiplied by a factor ten, then same feature was noticed. The above result used 10^3 walkers and 10^4 runs.

The mass has been calculated by using Equation (2.6), and is illustrated in the following box:

Mass with jitter:	0.60205 ± 0.39 M_{Jup}
Mass without jitter:	0.47181 ± 0.156 M_{Jup}
Mass by MCMC-run:	0.258 ± 0.15 M_{Jup}

The estimated mass difference between the least squares fit method and MCMC is apparent, and is due to the different yielded semi-amplitudes of both mentioned methods. The case of jitter and jitter free least squares fit method do agree within their 1σ uncertainty.

Figure 3.3 illustrates our fit to the data sample, which is a better fit than `KOI-102`, due to lower chi-square, resulting in a χ^2_{red} of 9.04 compared 19.7 for `KOI-102`. But, the error of the fitted amplitude is still larger in `KOI-94`, compared to `KOI-102`. The fit of `KOI-94` is weak compared to a recent publication (Weiss et al., 2013), who separate the radial velocity measurements into segments by more detailed observations of the exoplanets movement. Their semi-amplitude is 19.68 ± 2.19, which lies closer to our MCMC-guess. Another factor is their root-mean-square of 5 compared to ours, which is 4 times larger. They find a mass of the exoplanet, `KOI-94d` or `K00094.01`, to 0.33 ± 0.03 M_{Jup} , which is larger than the result by the MCMC-run, but smaller than the result by least squares fit.

I have combined both data-sets of the stellar system, `KOI-94`, into a figure to illustrate the difference. This figure is represented on the following page.

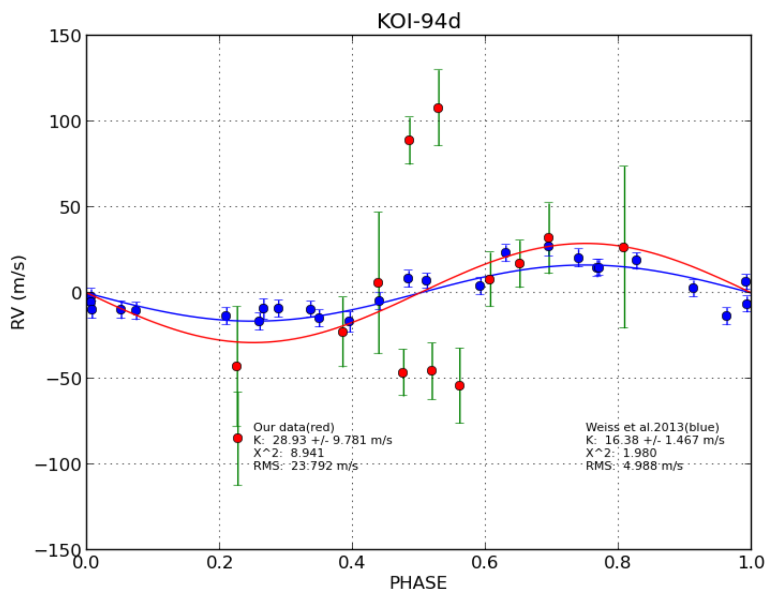

Figure 3.5: Same plot as in Figure 3.3, but compared with the data sample of Weiss et al. (2013)

As mentioned, they achieve a lower root-mean square and a reduced-chi-square of 1.98, so the fit is well made. It should be noted that the fit done above assumes that the only planet yielding a dominant semi-amplitude is `K00094.01` or `KOI-94d`.

A combined data set would increase χ^2_{red} to 4, but the amplitude would be a bit smaller than for the their amplitude, thus giving us a mass slightly smaller; 0.27 $\pm$ 0.30 M_{Jup}. So, the uncertainty on the mass increases by introducing our data sample, due to our larger uncertainties. Our mean uncertainty of the dataset is more or less twice as large as their measurements. The difference could be due to the different instruments used. The authors used HIRES at the Keck I telescope (Weiss et al., 2013), while our data is taken by FIES at the Nordic Optical Telescope.

A combined plot looks almost the same as in Figure 3.5, since the fitting procedure, least squares fit, weighs the error-bars, and those of Weiss et al. (2013) are smaller and greater in number, so their results will weigh more, thus having a similar amplitude to the one given in Figure 3.5.

To conclude the topic of `KOI-94d`, or `K00094.01`; I estimate with a 99.7% confidence a minimum mass limit less than 1.8M_{Jup}, since a jitter could be apparent in the stellar system. Weiss et al. (2013) get a total mass of the system with 99.7% confidence, below 0.89M_{Jup}. The MCMC run will yield a mass a bit lower, of 0.71 M_{Jup} (within 3σ confidence).

3.3 False-positives

In the entry of this chapter, I briefly mentioned the topic of false-positive (FP). The false-positive determination on the Kepler candidates varies a lot; from 10% (Howard et al., 2012) to 50% (Beaugé and Nesvorný, 2013, *see references within*). A false-positive occurs, when an observed sign of an exoplanet is due to stellar jitter, a blending scenario by a nearby star or other. A blending scenario could mimic an exoplanet orbit quite precisely, and high resolution imaging is therefore required to dismiss scenarios.

An example could be as a star pulsates it would mimic a semi-amplitude, which could represent an exoplanet. But, this would be rejected by looking at the stellar luminosity and color variations (Mayor and Queloz, 1995).

The following section will introduce the term, jitter, in §3.3.1, and blending scenario, §3.3.2.

A peculiar detail discussed by (Beaugé and Nesvorný, 2013, cf. *Bonomo et al., 2012*) is that if the detected exoplanets by CoRoT are compared with the total amount of detected exoplanets proposed by *Kepler*, then CoRoT should have detected a much larger amount in the range $2R_{\oplus}$ to $4R_{\oplus}$. This fact might question the false-positive rate of *Kepler*. But a discussion is outside of our topic and should only further interest the reader into other branches of exoplanetary science.

3.3.1 Jitter

From section 2.1.1 we learned that stars can broaden their emission lines. This broadening of the lines is due to the stellar motion, but in cases, additional broadening can be due to the activity of the star, which is referred to as jitter or noise. This factor can be as powerful as to mimic an exoplanet pulling on the star. A jitter source could as well be caused by instrumental effects, and a study of 100 main-sequence stars yield a jitter of 2 m s^{-1} (Cochran et al., 2011). In the case of `KOI-102`, the star was a main-sequence star, and the jitter I applied (blue case) in Figure 3.1 was around 20 m s^{-1}. A similar case is seen for `KOI-94`, but since this star is larger, the jitter is expected to be larger, which is seen on Figure 3.3 (*The jitter is around 50 m* s^{-1}).

The amount of jitter produced depends on the age and stellar activity, and it can be as large as 78 m s^{-1}, as in the case of `HAT-P-32` (Hartman et al., 2011). The last mentioned author also notices that large jitter could as well be an indication of multiple exoplanets. A possible exoplanet companion can be seen at the bisector spans (BS) from the RV-measurements. These look like the ones represented in the bottom of Figure 3.1 and Figure 3.3. If there is a large scatter in the measurements, then no additional exoplanet is expected, but a Lomb-Scargle frequency spectra can indicate these features by noticing the peaks in the spectra (Hartman et al., 2011).

The case of jitter by stellar activity can be tested by determining the age, as later described in section 3.4.1. Older stars are typically more quiescent, thus containing less jitter in their atmosphere. Another method is to measure the chromospheric emission in the Ca II H and K-lines. A large jitter can also appear by nearby effects such as moonlight contamination of the spectra, but these conditions are typically noted and removed, when writing the RV-measurements.

In my data analysis, I added a jitter, and this was done to replicate "perfect" fits by increasing the error bar, but it shouldn't be advised if the jitter exceeds the semi-amplitude (Hartman et al., 2011), as it does in both our cases. These values are as well a lot larger than the expected jitter of main sequence stars, which contain a jitter of 2 m s^{-1} (Cochran et al., 2011).

Therefore to remove the false-positive probability of an object, many of these effects have to be disregarded, before one can confirm an exoplanet with confidence.

3.3.2 Blending scenarios

A blending scenario is when a binary star blends the light curve to indicate a transit depth, which could correspond to an exoplanet. This scenario can be resolved with high-resolution imaging, which can detect nearby fainter stars, which may be the source of the transit depth. A bisector span can as well rule out a blend scenario, as long as the scatter in BS-values is not comparable to the RV semi-amplitudes (Hartman et al., 2011).

An example could be the case of `Kepler-14`, where high resolution imaging has resolved a stellar companion with a similar magnitude. The exoplanet is then orbiting a binary, which in turn indicates that the observed semi-amplitude is lower than it really is. The increased semi-amplitude will increase the exoplanet mass by 60%, and the radii will increase by 10% (Buchhave et al., 2011). The authors warn that blending scenarios have a large impact on the estimated parameters of exoplanets.

3.4 Properties of stellar hosts

Stellar parameters are essential for precise determination for the parameters of exoplanets. To determine stellar parameters with a high precision, a comparison has to be made between, high-resolution and synthetic, spectra. This can be done by analysis packages, as Spectroscopy Made Easy (SME), which creates synthetic stellar spectra, based on free variables as, effective temperature $T_{eff\star}$, surface gravity $\log(g_\star)$, metallicity [Fe/H], and rotation velocity $vsini$. These spectra are then compared with the spectra of the star to obtain the stellar parameters.

To improve the precision of stellar parameters, astronomers typically compare their SME results with the Yonsei-Yale tracks (Yi et al., 2001) series of stellar evolution models (Hartman et al., 2011). It should be noted for the reader that there are multiple methods to determine parameters for a star, which are described in a published paper of Southworth (2010).

3.4.1 Determination of Age

Age determination is a very uncertain parameter due to its dependency on parameters such as effective temperature, metallicity and stellar density (Triaud, 2011). Usually estimations of age come from evolution tracks of stars, such as Yonsei-Yale (Yi et al., 2001). Observational estimation is also possible: If a star has a low Lithium abundance (logA(Li) < 0.4, or equivalent width lower than 11mÅ) with a low rotation rate and no signs of stellar activity, then it is most likely older than the Sun. The mentioned observational conclusion can still give a large uncertainty as seen for `WASP-54`, where the estimation is $4.4^{+7.4}_{-2.4}$ Gyr (Faedi et al., 2013).

Another observational method is to determine the gyrochronological age, which makes use of a relation between the age and rotation rate. In such case, caution needs to be taken, when a companion of large mass is orbiting the stellar host, since an alteration of rotation rate may occur by tidal interactions.

3.4.2 Determination of T_{eff}

The temperature of stellar surface is obtained by observing excitation lines of the stellar spectra, as the Hα-line. Highly ionized hydrogen lines point towards OB stars, while numerous molecular lines indicate a colder star, such as, KM stars. These stars will inflict different properties upon a spectra as described in section 2.2.1. Photometric measurements can also predict a temperature by observing the luminosity of the star, as the space telescope *Kepler* does it.

3.4.3 Determination of the surface gravity

The surface gravity, $g_\star$, is determined by a spectrum. Lines as NaI D and Mg Ib are used as diagnostics for the surface gravity. A high precision is required, since the surface gravity and effective temperature are necessary to obtain precise values of mass, radii and metallicity.

3.4.4 Determination of $M_\star$ and $R_\star$

The determination of mass can be done in several ways. In the case of a binary star, a simple use of Newton's form of Kepler's third law will yield the exact masses. A single star is harder to determine the mass of, thus a calibration is usually used, where an observed $\log(g_\star)$ and T_{eff} estimate the mass and radii. But, $\log(g_\star)$ is usually poorly constrained by spectroscopy. The process can be seen in (Yi et al., 2001, table 4), where a combination of temperature (T_{eff}) and $\log(g_\star)$ can estimate the mass of a star.

The radii of a star can as well be found by knowing the distance and flux of the star. The radii and mass of a star are typically assumed to have an uncertainty on 5 - 10% (Seager et al., 2007). The radii of a star has a linear-relation to the radii of the exoplanet (Latham et al., 2010), while a more massive star would inflict a more massive exoplanet, as seen in Equation (2.6).

3.4.5 Determination of radial velocity

The radial velocity of a star can be found by investigating the broadening of lines within the spectra. These broadenings were due to the movement of the star around the center of mass, as was described in section 2.2.

3.5 Final remarks on the data

None of the data, which was fitted showed any exoplanets with a high confidence, due to large values of reduced chi-square. The result, which I achieve from the data, is that there might be exoplanets with a total mass of $<0.19 M_{Jup}$ (`KOI-102`) and <1.8 M_{Jup} (`KOI-94`), with a 3σ confidence. It should be noted that the false-positives for multiple planet-systems are low, so more observations of `KOI-102` could be relevant.

If I assume that these exoplanets are composed purely by Hydrogen and Helium (H/He) in hydrostatic equilibrium, then the mass-radii relation can be described by $R \propto M^{1/3}$ (Zapolsky and Salpeter, 1969). A more modern equation of state of these gasses would yield a less strict relation, of $R \propto M^{1/10}$ (Fortney et al., 2011a). The difference is due to the fact that the first mentioned mass-radius relationship only takes coulomb forces into account, while the second one is a mixed-state between atom-interactions (Coulomb) and degeneracy.

`K00102.01` has a mass below 0.19 M_{Jup} and a radii of 0.33 R_{Jup} ($3.7 R_\oplus$). If I take a look at Figure 1.3 at page 5, then I notice that the exoplanet is by no means inflated. If the mass-radius relations are used to investigate its radii by mass for a H/He sphere, then the following results are achieved; 6.3 $R_\oplus$ and 9.2 $R_\oplus$, model of Zapolsky and Salpeter (1969) and Fortney et al. (2011a), respectively. These radii depict the planets estimated radii by mass if a simple H/He-cold sphere is assumed. In the introduction, I mentioned that a method to vary the radii is to insert a core mass of heavy elements. A larger core mass would decrease the predicted radii of the models, so a case of an icy planet is likely, and predicts a radius around 0.4 R_{Jup}.

According to Figure 1.3 the conclusion must be that `K00102.01` is an icy planet with some rocky interior, if the mass 0.19 M_{Jup} is assumed.

In the case of `KOI-94d`, I assume the mass by the 3σ limit, even though the mass is proposed to be 0.33 M_{Jup} (Weiss et al., 2013). The exoplanet has a mass of 1.8 M_{Jup} and a radii of 0.843 R_{Jup} ($9.259R_{\oplus}$). The exoplanet is not inflated compared to the standard cooling models described in Fortney et al. (2011a), as the radius depicted from Figure 1.3 is around 0.9 R_{Jup} for a mass of $1.8M_{Jup}$. If the hydrostatic equilibrium of the H/He-exoplanet is purely by coulomb forces, then a radii of 13 $R_{\oplus}$ is predicted. The exoplanet is therefore far from inflated, but it is known that an upper limit on mass has been taken. If the results of Weiss et al. (2013) are taken into consideration, then the planet becomes slightly inflated if the interior is purely dominated by coulomb forces. A more realistic model would still predict the exoplanet to behave below the standard cooling model, as seen in Figure 1.3 (magenta line).

Remember that these exoplanets are in close-in orbits, thus as well irradiated by the solar host, but these objects can still be explained by the models of Fortney et al. (2007) described in Figure 1.3 (blue lines).

The exoplanets analyzed in this Chapter can be explained by the models, and are therefore not inflated, as was initially predicted. The following Chapter will discuss the matter of inflated exoplanets.

CHAPTER 4

Inflated exoplanets

To date over nine-hundred exoplanets have been confirmed, which vary largely on the physical properties (Wade, 2013). The larger variation of exoplanets is seen in Figure 4.1 especially for the gaseous giants, as introduced in Chapter 1. This is due to the fact that larger exoplanets are easier to detect, therefore more numerous, as described in Chapter 2, but an upcoming confirmation of the *Kepler* exoplanet candidates might change the variation towards lower mass exoplanets as well. The Figure on the next page depicts all currently confirmed exoplanets on a mass-radii plot by red-dots. The blue and green dots indicate the solar planets, and targets of our sample; all exoplanets below 0.2 g cm^{-3}, respectively. The black lines, solid and dashed, indicate the density limit of our sample and the density of the solar planets; Saturn, Jupiter and Earth.

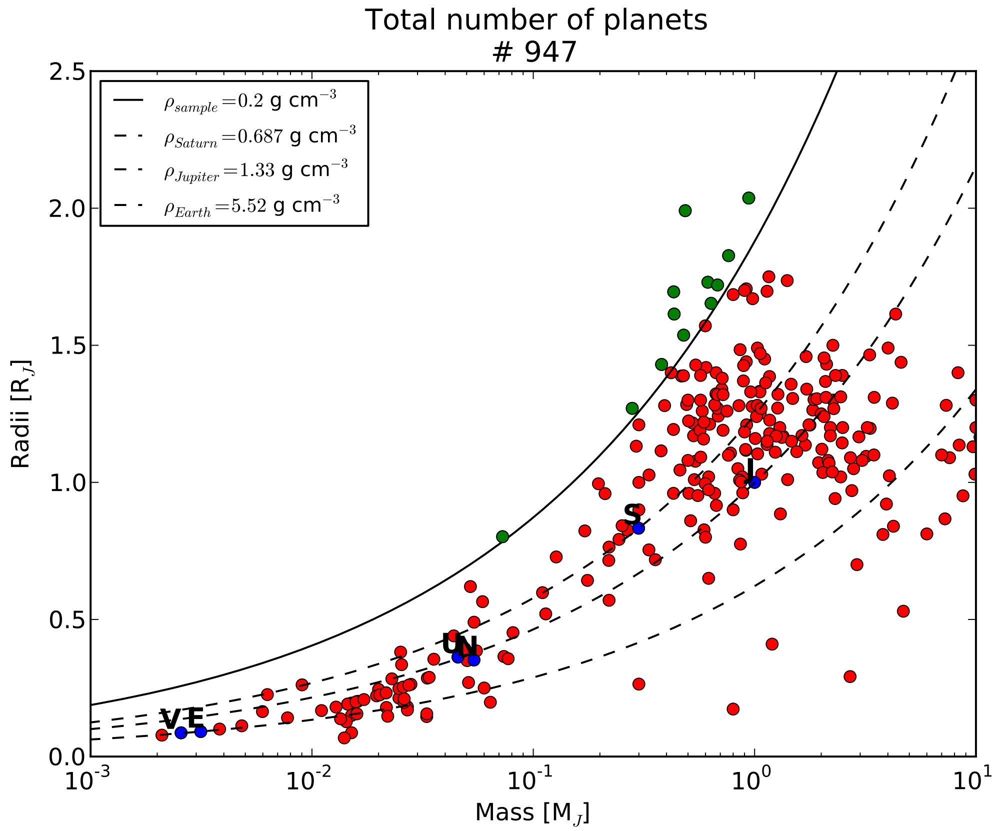

Figure 4.1: The figure depicts all confirmed exoplanets, with four isodensities; the solid line indicates a density of 0.2 g cm^{-3}, which is the upper density limit of our sample, the three dashed-lines represent the density of `Saturn`, `Jupiter`, and `Earth`. The blue and green dots indicate the planets in our solar system and our sample of interest, respectively.

The mass of Jupiter and Saturn differ by a factor of 3, while their radii differ by less than 1/5. A similar variation in radii is not observed for exoplanets since the radii of Jupiter-mass planets can vary by a factor of 2. This feature can be seen on Figure 4.1, where a 1 M_{Jup} exoplanet can have radii in between 0.25 R_{Jup} and 2 R_{Jup} .

The largest exoplanets by size are important for exoplanetary science, since their large radii enables us to investigate exo-atmospheres by the occultation. Spectra of these large exoplanets are still of very low-resolution, but future investigation in this area will give a lot of information about the atmospheric composition of these puffed-up giants (Burrows, 2013a,b).

In the introduction of this thesis, I explained that the interior of exoplanets differs depending on the mass. The more massive exoplanets have partially degenerate interiors, and become more degenerate with increasing mass, while lower mass exoplanets are supported by coulomb force. These states of the material in the interior of exoplanets will yield different mass-radii relations, as seen in Figure 1.3 in Chapter 1 and Figure 4.2. The exoplanets above the relations are numerous as can be seen on the following figure.

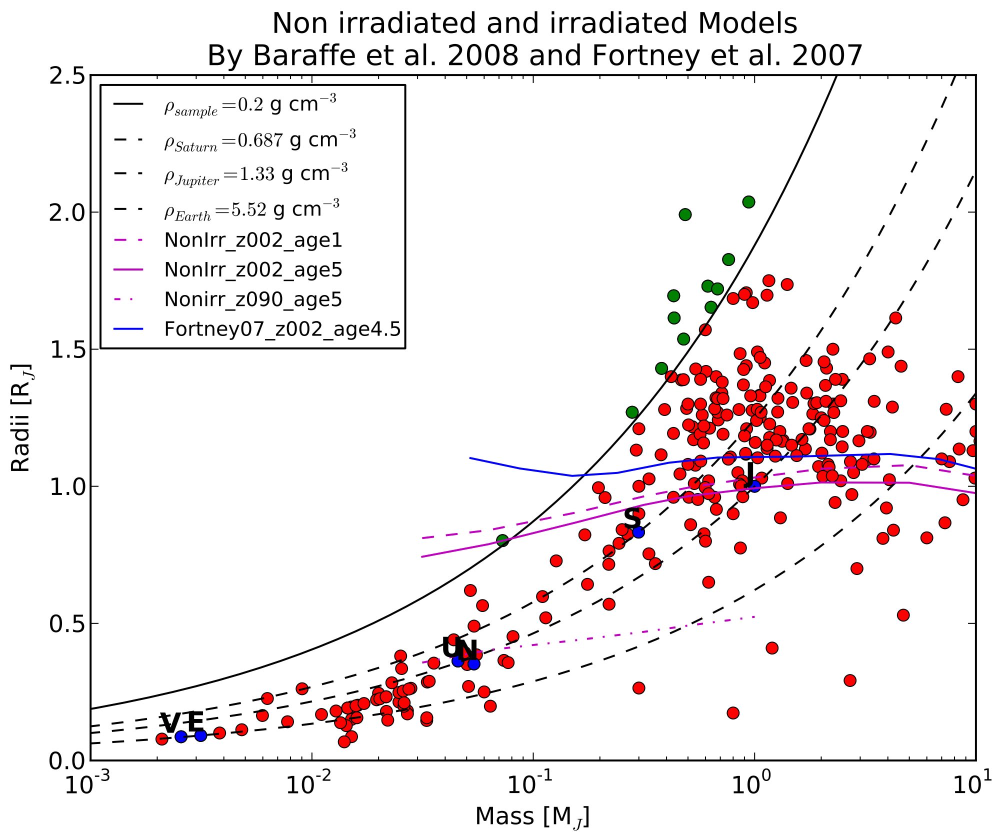

Figure 4.2: The figure illustrates the problem with the observed exoplanets being larger than expected by the standard models (Baraffe et al., 2008). The magenta colored lines are made by the models of Baraffe et al. (2008) for a Sunlike system with a 10 $M_\oplus$ core, and are indicated by the annotation in the figure. The blue line is taken from the models of Fortney et al. (2007) for a 0 $M_\oplus$ core mass at 0.045 AU, and is similar to that of Figure 1.3.

The Figure shows the trend introduced in the first Chapter; A numerous amount of exoplanets have larger radii than predicted by the equation of states for partially - and degenerate matter (magenta line). A younger planet system would only slightly lift the radii predicted by the models (dashed-magenta line). These models assume a core mass of 10 $M_\oplus$, but a lower core mass would slightly lift the predicted radii dependent on the mass. This dependence is due to the ratio of the core-to-planet mass; as the planet mass increases the effect of the core diminishes (Fortney et al., 2007).

The interesting part of the Figure 4.2 is that the radii of some exoplanets are up to 50% larger than expected by stellar non- and irradiated models (Hartman et al., 2011) and a few exoplanets are even up to 100% larger than expected, as seen by the upper green dots. These occurrences cannot simply be due to minor adjustments to the models, and therefore a heating mechanism is required. The mechanisms could involve a sudden stall of interior cooling, contraction due to migration thereby increased incident flux, tidal heating, or maybe a combination of heating mechanisms.

Most inflated exoplanets are in close-in orbits and thus heavily irradiated. Demory et al. (2011); Fortney et al. (2011b) have noted that there is a relation between the inflated state of a planet and its incident stellar flux. It is observed that the inflation occurs above a value of $2 \cdot 10^8$ erg s^{-1} cm^{-2}. More on this topic will be discussed in section 5.2 after a detailed discussion of the heating mechanisms has been given.

In this chapter, I will focus on three mechanisms of planet inflation that could affect all gaseous exoplanets to some degree. The metallicity could affect the atmosphere of a planet, thus increasing its opacity, which in turn decreases the cooling rate of a planet. This is referred to as the enhanced atmosphere, and was at first proposed by Burrows et al. (2007).

Another mechanism is the tidal dissipation, which all close-in exoplanets should be affected by to some degree. The mechanism can generate a large amount of heating as the exoplanet circularizes, but the circularization requires an initial eccentric orbit. An eccentric planet orbit can occur during a disk-planet or planet-planet interaction. The mechanisms behind tidal heating has been discussed during the past decade and is a popular theory (Jackson et al., 2008a,b; Liu et al., 2008; Miller et al., 2009).

A third mechanism could be the ohmic heating, which is due to the drag between metals in the atmosphere and magnetic field. This drag should occur due to the high velocity winds in an irradiated-envelope[1]. The idea has recently been proposed to

[1] The conditions are predicted to T$\geq$ 1500 K and $v_{wind} \geq$ km/s, but better spectra are required

affect the irradiated exoplanets by Batygin et al. (2011); Perna et al. (2012)

Each heating mechanism is plotted into a (M_{pl},R_{pl})-plot to show the predicted radii of exoplanets. It should be noted that the results are based on rough assumption, and therefore not strictly correct, because of the large amount of assumptions within the models. These considerations will be further discussed in Chapter 5.

This Chapter will include the mechanisms behind inflation of exoplanets, §4.1, where I will explain the enhanced atmosphere, §4.1.1, tidal dissipation §4.1.2 and Ohmic heating §4.1.3. After explaining the mechanisms, I move towards looking at our set of low density exoplanets, ranging from 0.08 to 0.18 g cm^{-3}; `Hat-P-32 b` §4.2.1, `HAT-P-33 b` §4.2.2, `HAT-P-40 b` §4.2.3, `Kepler-7 b` §4.2.4, `Kepler-12 b` §4.2.5, `WASP-17 b` §4.2.6, `WASP-31 b` §4.2.7,`WASP-39 b` §4.2.8, `WASP-54 b` §4.2.9, `WASP-63 b` §4.2.10 and `OGLE-TR-10 b` §4.2.11. The description will be useful to give an idea of the variety of each system that contains inflated exoplanets.

4.1 Mechanisms for inflation

Almost all inflated exoplanets are at low proximity of their host star, which averages to a distance of 0.045 AU. This distance is represented by a dashed line in Figure 4.3.

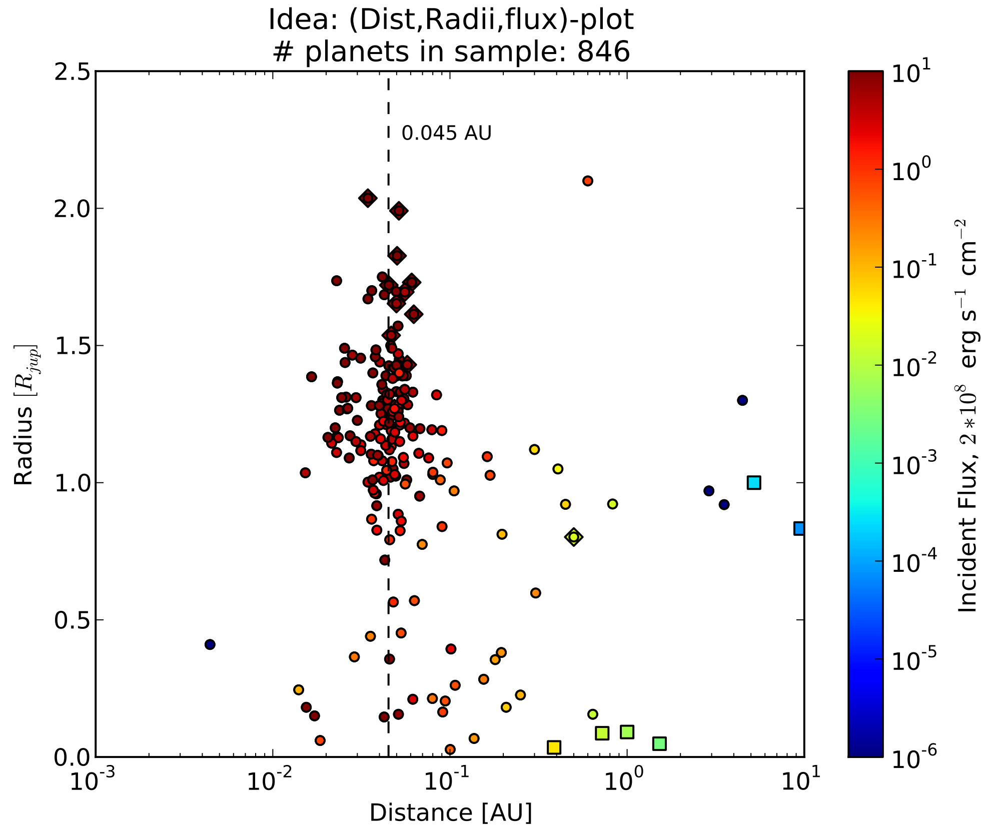

Figure 4.3: The figure depicts the radii and proximity to the stellar host for all exoplanets within 5.2 AU. The colors indicate the incident flux in order of the flux limit of 2×10^8erg s^{-1} cm^{-2}. The squares and diamonds indicate the solar planets and the low-density planets in our sample.

The figure clearly depicts that most of the large exoplanets have close-in orbits of a distance less than 0.1 AU. The close orbit results in a high level of irradiation by their stellar host, as seen by the colorbar. The figure clearly indicates that one should not compare these large exoplanets by the non-irradiated models by Baraffe et al. (2008), but use the models of Fortney et al. (2007). The latter models are based under Sunlike conditions (solar abundance, G2V star) for a given age and core mass. I will illustrate the case of a 1 Gyr model and 5 Gyr with two different core masses; 0 $M_\oplus$ and 10 $M_\oplus$. The first mentioned core mass should be understood as the upper-limit of the model, as can be seen by the solid lines in Figure 4.4.

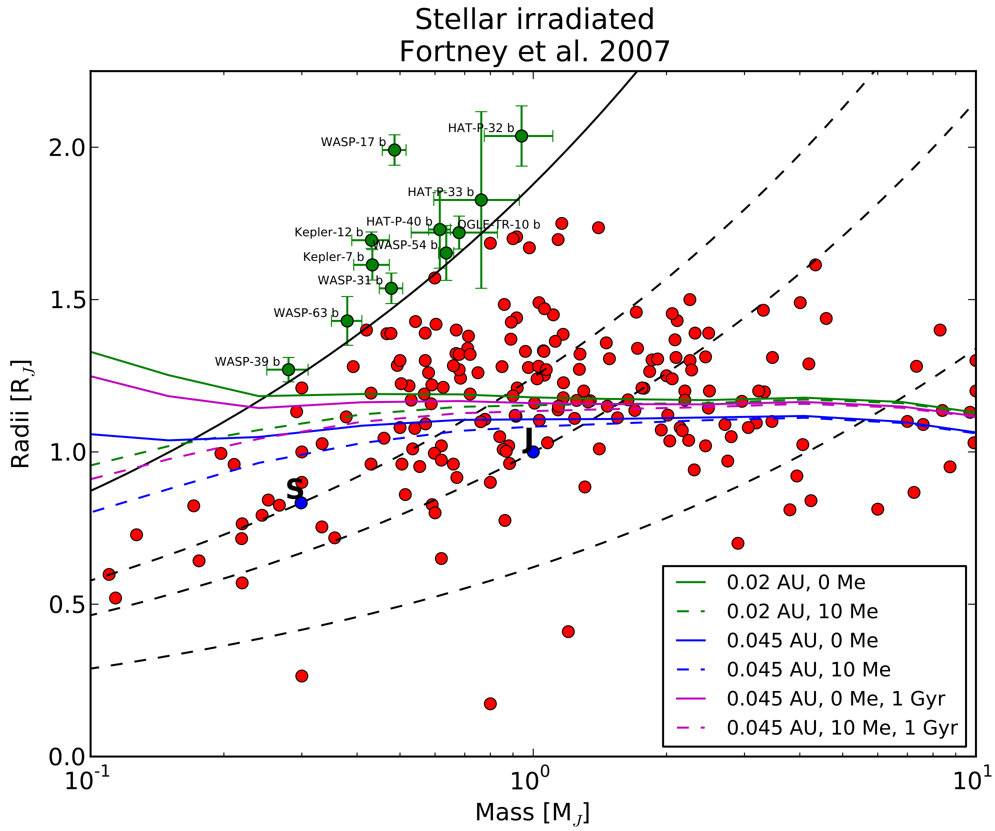

Figure 4.4: The figure depicts the model of Fortney et al. (2007), which predicts radii of stellar irradiated planets. The green and blue lines indicate a distance of 0.02 and 0.045 AU at an age of 4.5 Gyr, respectively, while solid and dashed indicate a core mass of 0 and 10 $M_\oplus$, respectively. The magenta colored line is the same as the blue, but at an earlier age, 1 Gyr. Red, Green and blue dots are all the confirmed exoplanets, low-density sample and solar system planets (Saturn, Jupiter are shown), respectively.

The blue line apparent in the figure above is the same as the one depicted in Figure 4.2. All named exoplanets are the ones being described later in section 4.2. Exoplanets with no core mass tend to be larger for lower planet masses, compared to 10 $M_\oplus$ core mass planets, because of the lower degenerate electron pressure. This tendency disappears as the exoplanet mass becomes larger, because of an increased degenerate electron pressure. Fortney et al. (2007) also mentioned that the core mass has a lesser affect as the planet mass increases, which also mixes the dashed and solid lines towards the larger masses.

The general approach towards making models to explain inflated exoplanets is to find a method that ensures capture of internal heat, thus reducing the cooling rate. Exoplanets contract continuously, thereby reducing their radii, but if this contraction was stalled, then the larger radii could be apparent at a later stage in the planetary evolution. A core-less 0.3 M_{Jup} planet at 0.045 AU is around 1.9 R_{Jup} at 10 Myr, while being reduced to 1.2 R_{Jup} after 1 Gyr (Fortney et al., 2007, cf. Fig. 5). If a contraction could be stalled for at least 1 Gyr, then a possible explanation could occur for an inflated radii.

Different mechanisms suggest different ways of enhancing the heating required for inflating the radii. It could be by external sources, such as tides, or internal, as the opacity, which could thicken the atmosphere or operate in a specific pattern, i.e. Double diffusive convection (Fortney et al., 2011a). For a brief overview over some of the other mechanisms, I would refer to a review by (Fortney and Nettelmann, 2010, cf. *section 4*)

In the following section, I choose to focus on three models, which try to explain the appearance of inflated planets. The first model is the enhanced atmosphere, where the atmosphere is enriched §4.1.1. It is alike the double diffusive model, but differs on the fact that the latter model is more advanced, since it includes the molecular weight gradient. The second model is the tidal dissipation, §4.1.2. It can explain the larger radii, but fails to explain scenarios with a circular orbit for older inflated exoplanets. The last model is the Ohmic heating §4.1.3, which makes use of the magnetic drag in the atmosphere by the ionized alkali.

In each case, an applied prediction of radii will be applied to illustrate the predicted enhanced radii of each model.

It should be noted that the models are taken directly out of articles for each heating mechanism. In the case of enhanced atmosphere, I received a core-heating model, instead of models based on different atmosphere enrichment. The core-heating model is based on Burrows et al. (1997), and is a model which tells us how much heating is required to inflate a planet to a given size. It should be noted that higher opacity would result in a lower heating, because of the thicker atmosphere decreasing the cooling rate. A similar core-heating mechanism is extracted from Miller et al. (2009), and in the case of Ohmic heating a model is extracted out of Batygin et al. (2011), which is a function of temperature and efficiency for a given mass.

4.1.1 Enhanced atmosphere

It is observed that the close-in exoplanets of large radii are heavily irradiated by their stellar companion, as seen in Figure 4.3. This should mean that the atmosphere of these exoplanets would not behave in a similar manner to the atmosphere of Jupiter, which has a incident flux more than 6 orders lower. The atmosphere of close-in planets would have an increased amount of optical and UV radiation, which could alter it towards a thicker opacity. The use of non-irradiated models might therefore underestimate the contraction rate of these close-in planets, and predict wrong radii. The proposed mechanism of altering the atmosphere has then been to enhance it with a higher metallicity (Burrows et al., 2007), but this has been a subject of critics (Fortney et al., 2011a).

The atmospheric opacity can be detected by spectroscopy, and highly irradiated exoplanets are proposed to have enhanced opacities due to gases such as TiO and VO (Anderson et al., 2010; Knutson et al., 2010). Other exoplanets can as well be highly irradiated, but not inflated, as seen on Figure 4.3. The appearance of low radii irradiated exoplanets might be due to a different evolution or core mass (Anderson et al., 2010). Fortney and Nettelmann (2010) mention that spectra of hot-Jupiter atmospheres neither support nor refute the assumed opacities of the enhanced atmosphere, due to the low resolution of spectra.

The model has its problems; such as, if the enhanced opacity is purely by metallicity then it would not be maintained in the upper layers of an inflated atmosphere, but dive into deeper layers, so a mixing is required (Fortney et al., 2011a). The model could explain the inflated radii of `HD 209458 b` by 3 times larger solar metallicity, but even a 10 times solar metallicity cannot explain the large radii of `WASP-17 b` (Anderson et al., 2010), see section 4.2.6.

Another problem with the model is that a higher metallicity planet results in increased core mass, which instead leads to a decreased planet radii compared to a planet of same mass, but lower metallicity (Enoch et al., 2012). But, if the metals are placed within the atmosphere of an exoplanet, than an increase in radii will be slightly larger than the decrease in radius by increased metallicity of the envelope (Burrows et al., 2007).

I have received a core-heating model, which is based on the solar metallicity and corresponds to the lower boundary of the prediction by the enhanced atmosphere model (Burrows, 2013b; Burrows et al., 1997). The model depicts the achieved equilibrium radii at a given heating of the core. In other words; in the model a heating-power is inserted in the core of the planet, so the planet would inflate.

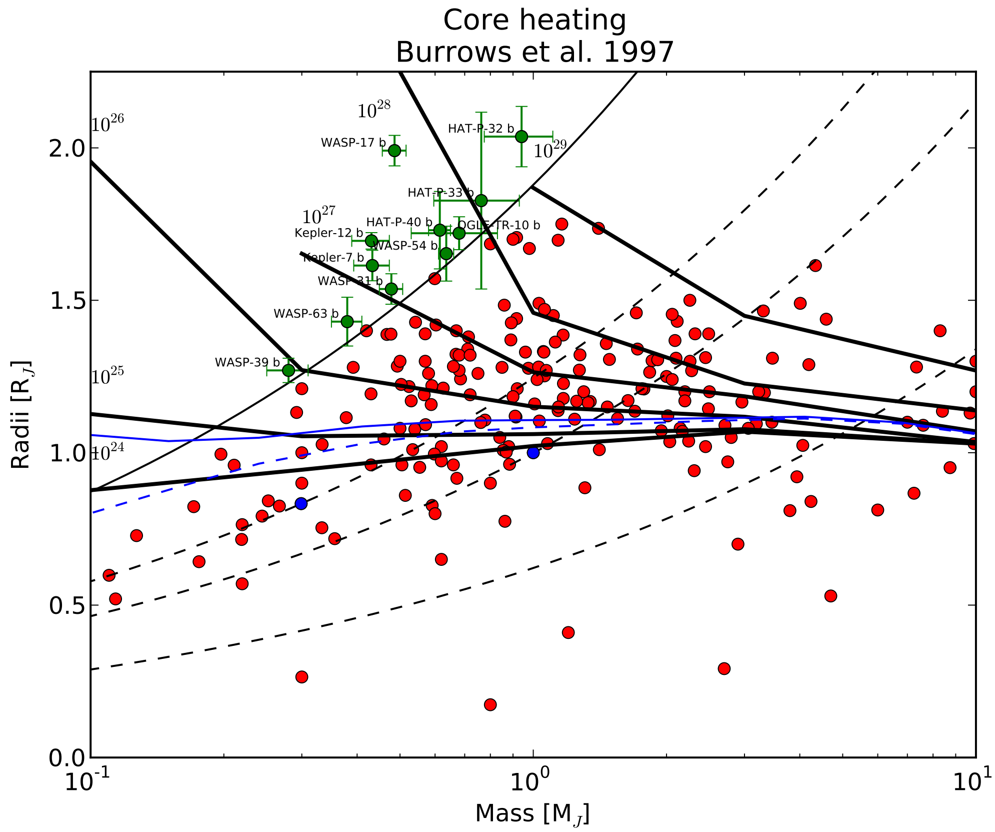

Figure 4.5: The figure depicts the core-heating models of Burrows et al. (1997) by thick solid lines. The applied heating in the models range between 10^{24} and 10^{29} erg s^{-1} . The model also depicts the models of Fortney et al. (2007) by the same annotation as in Figure 4.4. The isodensities are annotated as in Figure 4.1.

Figure 4.5 depicts the exoplanets including our low-density sample by green dots. It can be seen that exoplanets such as `HAT-P-32 b` cannot be inflated to its radii with a core heating of 10^{29} erg s^{-1} and a Sun-like assumption[1]. Evaporation would occur for exoplanets less massive than $1 M_{\mathrm{Jup}}$ at this level of heating, therefore some feature has to be inserted into the atmosphere to keep it intact. A candidate could be an increased metallicity, but as is seen in table 4.2: `HAT-P-32` is less metal rich than the Sun by 8%. This would contradict a higher metallicity atmosphere, but a larger dose

[1]Here I refer to a stellar host being G2V with a solar metallicity

of UV, optical radiation is expected due to the stellar class of `HAT-P-32`. The larger amount of radiation might trigger some alteration of the exoplanets atmosphere, to enrich it to a thicker opacity.

But, the case could as well be that another mechanism is responsible for the inflated radii of `HAT-P-32 b`.

4.1.2 Tidal dissipation

Tidal dissipation occurs as two orbiting celestial bodies inflict each other with a tidal force. The tidal force heats up the lighter body, in this case, exoplanets, to slow or stall planetary contraction (Fortney and Nettelmann, 2010).

An example of tidal heating can be observed in the case of Io[1]; where tidal heating is responsible for a large geological activity, by gravitational pulls from Jupiter and the other Galilean moons; Europa, Ganymede and Callisto. The multiple pulls create a tidal-lock, and thereby a continuous tidal heating, while for a single system, the tidal heating will stop as soon as the orbit becomes circular. It should be noted that many close-in exoplanets are tidally locked (Ibgui and Burrows, 2009; Spiegel and Burrows, 2013).

The timescale of tidal heating can be expressed by the following equation (Liu et al., 2008),

$$\tau_{circ} = 0.10Gyr \times (\frac{Q_p}{10^5})(\frac{\mathrm{M}_\star}{\mathrm{M}_\odot})^{-3/2}(\frac{M_p}{M_J})(\frac{R_p}{R_J})^{-5}(\frac{a}{0.05AU})^{13/2} \tag{4.1}$$

The parameters are; the tidal dissipation parameter Q_p, stellar mass, $\mathsf{M}_\star$, semi-major axis, a and planet mass and radii, M_p and R_p, respectively. The tidal dissipation parameter is an uncertain value, which is a function of driving frequency(Miller et al., 2009, cf. *Ogilvie & Lin 2004*), amplitude of the distortion and internal structure of the celestial object[2].

Ibgui and Burrows (2009) estimates the value of the tidal dissipation to be $10^{6.55}$, while a simulation compared to observed exoplanets determines Q_p to lie in the range $10^6 - 10^7$ (Beaugé and Nesvorný, 2012). The equation above predicts that a Jupiterlike planet at a close-in orbit (0.05 AU) has a circularization orbit of 0.1 Gyr for a star like the Sun. In the case of a low density exoplanet, such as `HAT-P-32 b`, the timescale would be 2 Myr (for the eccentric case, see section 4.2.1). The age of

[1]The innermost of the four Galilean moons orbiting Jupiter

[2]It should be noted that the Q-value is based on the observed circularization time; 10^5 for stellar binaries and 10^5 - $10^{6.5}$ for Jovian planets. It might be different in cases for the close-in gas giant systems (Burrows, 2013b; Miller et al., 2009)

`HAT-P-32 b` is 2.7 Gyr, and a circularization should only be a brief moment in the planets lifetime.

A problem with the circularization timescale is that it is shorter than the age of the exoplanets, as seen for `HAT-P-32 b`. The circularization timescale lies in average between 0.1 - 1 Gyr (Fortney et al., 2011a; Jackson et al., 2008a), while the age of exoplanets in our low-density sample range from a lower age of 0.5 Gyr (`WASP-31 b`, §4.2.7) to 9 Gyr (`WASP-39 b`, §4.2.8). Baraffe et al. (2003); Leconte et al. (2010) notice that the mechanism occurs to early in the evolution, so the radiation is already radiated away at the present age of the systems.

It should be noted that earlier versions of tidal heating did not take orbital decay into account, thus yielding incorrect results. Jackson et al. (2008a) proposed a newer model with the orbital decay, and it leads to an equation of tidal heating, which estimates the required heating to inflate planets.

$$P_t = \frac{63}{4}\left[(GM_s)^{3/2}\left(\frac{M_s R_p^5 e^2}{Q_p'}\right)\right] a^{-15/2} \tag{4.2}$$

The equation above describes the tidal power, also called tidal heating, deposited in an planet. The model for the equation above disregards the other two tidal-dissipation effects, obliquity and alignment, and it should only be used for stellar systems which are relative slower than the orbiting planet (Miller et al., 2009). It should as well be noted that it is unknown where the tidal energy is deployed, but I assume it to be within the interior of a planet. This assumption will be discussed in section 5.3.2.

It is apparent in Equation (4.2) that if the orbit is circular then no heating will be deployed within the planet. So, I start out by introducing the general causes for eccentricities;

- A planet-disk interaction case; in which the protoplanet disk will exert a torque on the planet forcing it to move closer towards the stellar host. This effect will ensure an early-on circularization of the planet and decrease the semi-major axis, while the tidal heating will decrease as the circularization damps the eccentricity.

- Planet-planet interaction case; in which the interactions between the planets will transfer orbital energy and momentum, thus creating inward or outward migration. This would be the case if the close-in planet is in an eccentric path, and thus it would take longer time for circularization with a third-part companion to disrupt the circularization.

The second case is interesting, because free-floating exoplanets, as `CFBDSIR 2149-0403` have been observed, so a planet-planet interaction is probable. The exoplanet is the only one found so far due to the difficulty of detection[1]. But, it could as well be that this "coincident"/exoplanet is formed by itself in the interstellar space (Wade, 2013).

It is mentioned that if a tendency of more inclined exoplanets for massive stars than lower mass stars ($< 1.2\mathrm{M}_{\odot}$) is observed, then planet-planet scattering might be important (Triaud, 2011). More massive stars would have more massive disks[2] that are more likely to form planets, thus causing a more dynamical/chaotic planet formation (Beaugé and Nesvorný, 2012).

The circularization can as well be changed by the tidal-damping effect from the exoplanet upon the star, but these effects have not been taken into consideration in further investigation of the tidal-heating due to their uncertainty. The stellar tidal dissipation, $\mathrm{Q}_{\star}$, can broaden the timescale at low values ($\mathrm{Q}_{\star} \lesssim Q_p$) or become narrow as $\mathrm{Q}_{\star}$ becomes larger - thereby producing an inward spiral of the exoplanet due to the quick timescale of circularization (Ibgui and Burrows, 2009).

Figure 4.6 is built on the results of simulations for different runs with a $1\mathrm{M}_{\mathrm{Jup}}$ orbiting a Sun-like star at 0.05 AU (Miller et al., 2009). The figure depicts the required internal heating for a 5 Gyr old exoplanet with a 10 $\mathrm{M}_{\oplus}$ core to reach a given radii. The models also assume a H/He envelope with a helium abundance of 27% (Y = 0.27). The results seen on Figure 4.6 are made by hand, since the runs are not present for distribution (*private communication, Miller (2013)*).

[1]Rogue planets or free-floating exoplanets can only be detected by direct imaging, and require a high luminosity for detection

[2]The disk mass is said to be $0.1\mathrm{M}_{\star}$ ($M_D \approx 0.1\mathrm{M}_{\star}$, and the material available can be calculated as such; $M_z = 0.3 \times M_D \times Z_{\star}$

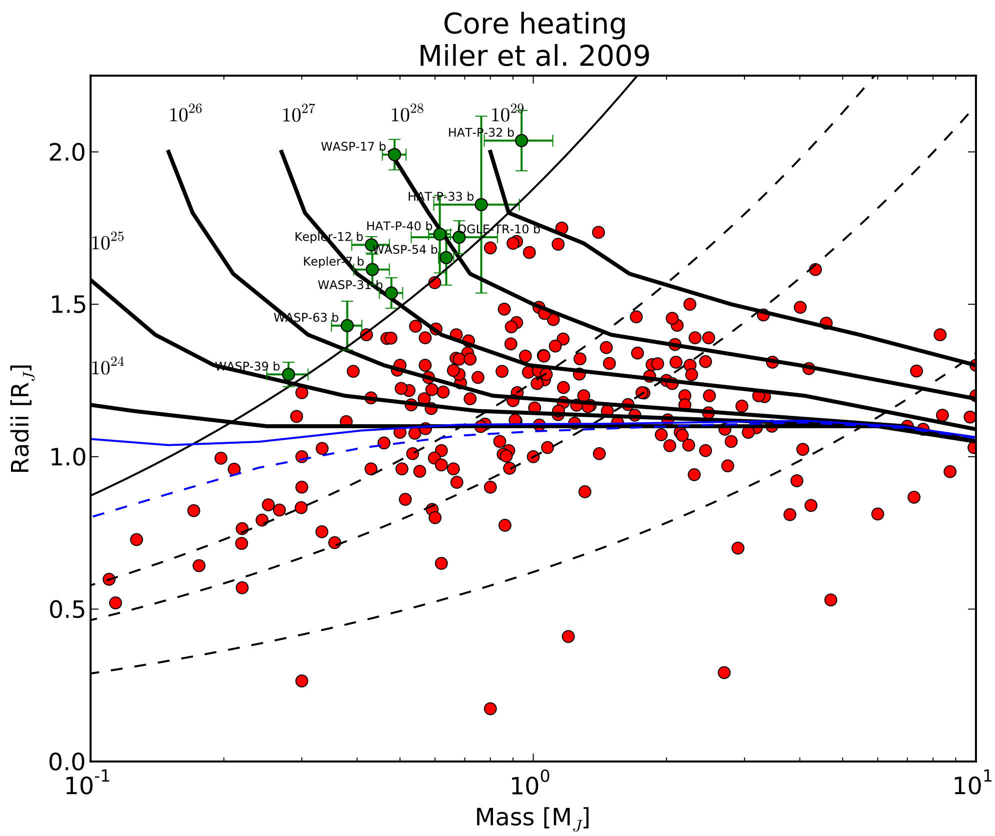

Figure 4.6: The figure depicts the internal heating as a function of mass, based on models by Miller et al. (2009). The thick solid lines are the required internal heating in erg s^{-1} for a given radius and mass. The dashed lines followed by one solid are the isodensities, as annotated in Figure 4.1. The blue lines are the stellar irradiation models from Fortney et al. (2007), as can be seen in figure 4.4

Figure 4.6 depicts that an internal heating of 10^{28} erg s^{-1} is sufficient for `Wasp-17 b`. This is a couple of orders larger than predicted by a constant contraction rate, which is in the order of 10^{25} [1]. This calculation assumes a constant radii throughout the lifetime and assumes a rapid planet formation shorter than a Gyr. Neither of these two assumptions are strictly correct, as it is known that young planets are far more luminous and contract faster at earlier stages (Burrows et al., 2007; Miller et al., 2009).The result indicates that the energy it "should" produce by contraction

[1] I assume a constant gravitational potential, $U \sim G \cdot \frac{M^2}{R}$ and the timescale of the system; all values of `WASP-17` can be seen in table 4.8 at page 72

is not sufficient to explain its current appearance. Instead an internal heating or contraction in the order of 10^{28} is required to explain the appearance.

The ratio of tidal heating and luminosity at the planets surface, P_t/L, can tell us about the importance of tidal effects (Miller et al., 2009); if the luminosity is smaller than the tidal power, then the ratio is above a unity, thus increasing the entropy and radii of the planet, while a ratio below a unity will continue the contraction. The ratio tells us if the exoplanet might be affected by tidal heating at the current stage. In our sample, I know all the necessary values; and to calculate the luminosity of the planet, I assume a black body radiation, thus $T_{eff} = T_{eq}$. But, it should be noted that this is a wrong assumption since the difference can be a factor 10 in difference for hot-Jupiters (Spiegel and Burrows, 2013)[1].

WASP		HAT		Kepler		OGLE-TR	
Exoplanet	P_t/L - ratio	Exoplanet	P_t/L - ratio	Exoplanet	P_t/L - ratio	Exoplanet	P_t/L - ratio
WASP-17 b	0.0029	HAT-P-32 b	1.41	Kepler-12 b	0.000192	OGLE-TR-10 b	0.0
WASP-31 b	0.0	HAT-P-33 b	0.0758	Kepler-7 b	0.00701		
WASP-39 b	0.0	HAT-P-40 b	0.00893	Kepler-30d	1.24e-09		
WASP-54 b	0.0061						
WASP-63 b	0.0						

Table 4.1: The ratio between the tidal heating and planets luminosity. If the ratio is above one, then the tidal heating is an efficient source. The results are calculated for $Q_p = 10^5$; lower values would yield higher ratios. But higher tidal dissipation values are expected (Beaugé and Nesvorný, 2012; Ibgui and Burrows, 2009).

The following values indicate that `HAT-P-32b` is affected by tidal heating, while this is not the case for the other inflated exoplanets in the low-density exoplanets. I go into further details of `HAT-P-32 b` in section 4.2.1. The distance between the solid heating-lines in Figure 4.6 shortens with increasing mass. This is due to the importance of the coulomb force decreasing with increasing mass, as the interior of the exoplanets becomes more degenerate.

4.1.3 Ohmic heating

The exoplanets which appear inflated are mostly affected by a large amount of stellar irradiation, as seen in Figure 4.3. The irradiation will inflict strong winds upon the atmosphere of the planet, and as well thermally ionize the alkali (Sodium and

[1]The effective temperature characterizes the difference between the outgoing and incoming fluxes, while the equilibrium temperature characterizes only the incoming flux

Potassium) in the atmosphere. The winds will advect the ionized alkali around the planet giving rise to a distinct magnetic field. The distinct magnetic field can then drive the photons by stellar irradiation into deeper layers of the planet and deploy kinetic energy. In a non-ionized atmosphere, these photons would deploy an energy at around 1 bar, but the ohmic dissipation proposes to advect these photons into pressures of 10 to 100 bars (*Conference talk, Fortney and Baraffe (2013)*). It has been proposed that additional mechanisms occur as the two magnetic fields interact (the distinct by alkali and the planets own magnetic field), which in turn could increase the power generate within the planet (Buzasi, 2013).

The before mentioned mechanism of tidal heating could initiate as soon as circularization was in progress. This is not the case for ohmic heating, since it has to be activated from the formation of the planet, thus requiring a minor migration towards the stellar host towards high levels of incident flux, or a fast inwards migration (Wu and Lithwick, 2013).

Batygin et al. (2011) has made a simulation based on a Sunlike model (Sunlike metallicity); depicting the exoplanets evolution with Ohmic heating for an efficiency of 3% and a core mass of 0 $M_\oplus$. The efficiency-term will be explained later, but it is a term for the "power" of Ohmic heating. Setting the core mass to 0 $M_\oplus$ gives an upper-boundary on the model.

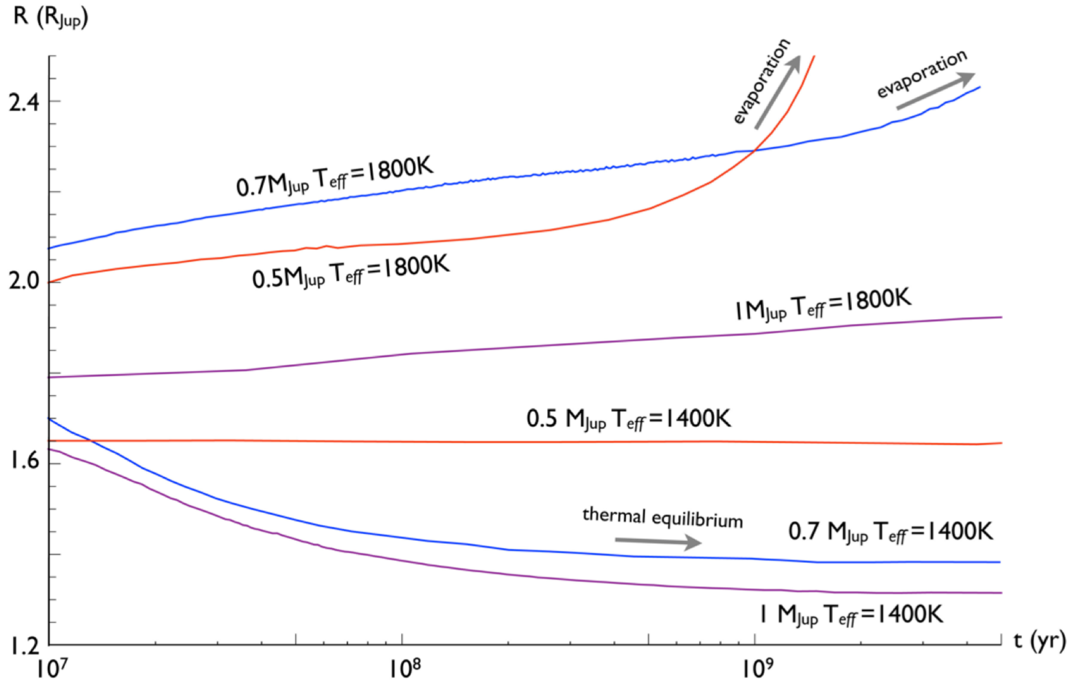

Figure 4.7: The figure depicts the evolution runs for different runs by Batygin et al. (2011). All simulations are stopped at a timescale of 5 Gyr. The runs are applied by an efficiency of 3%. All exoplanets with an effective temperature of 1800 K lead towards Roche lobe overflow, thus evaporation. But, the $1M_{Jup}$ planet is more stable due to its degenerate state, but ends in evaporation in a later stage. Figure taken from (Batygin et al., 2011, cf. Fig. 5).

The figure depicts the evolution run of several exoplanets of different mass, ranging from $0.5M_{Jup}$ to $1M_{Jup}$ at 1400 K and 1800 K. It is seen that for the higher temperature case, evaporation is inevitable. It looks stable for the $1M_{Jup}$ planet in 5 Gyr-run, but it is only due to its core being in a degenerate state, and it will eventually end in an evaporation (Batygin et al., 2011). Wu and Lithwick (2013) do not find any signs of evaporation by their calculations of the ohmic heating, compared to the results presented here. For the lower temperature case of Figure 4.7, the evolution of exoplanets is more stable due to the lower generated heat. It was seen earlier that large heating levels could end in evaporation, as for `HAT-P-32 b` in Figure 4.5.

To avoid evaporation for the lower mass planets, a core mass has to be inserted in the inner of the planet to keep it stable. Low-mass planets with no core mass have a higher chance to evaporate than those with larger core masses (Owen and Wu, 2013). The last mentioned authors notice that evaporation should apply for lower mass exoplanets, around Neptune-size, while not for Hot-Jupiters.

The main difference is that the ohmic heating has a higher equilibrium radii than the models of Burrows et al. (2007), where even 10x solar-metallicity in the atmosphere cannot yield radii of the Ohmic heating (Burrows et al., 2007, cf. Fig. 6 & Fig. 7).

The ohmic heating model depicts the behavior of the radii as a function of temperature at a given mass (Batygin et al., 2011). I transformed the models into a function of mass at a given temperature, to continue working on a (M,R)-plot.

There are three different efficiencies, ϵ, which determine the conversion of the kinetic energy from the wind into heating. The efficiency is a function of $(\rho_{pl}, v_\phi, H, T_{eff})$ (Batygin et al., 2011, Eq. (17)). Several of the parameters within the efficiency are quite uncertain and depend on the models built for the Hot-Jupiters; as the velocity of the atmospheric flows, or winds. A lower velocity of winds will reduce the Ohmic heating of a planet (Laughlin et al., 2011).

It should be noted that these values are taken out of the figures by hand (Batygin et al., 2011, Figure 6-8).

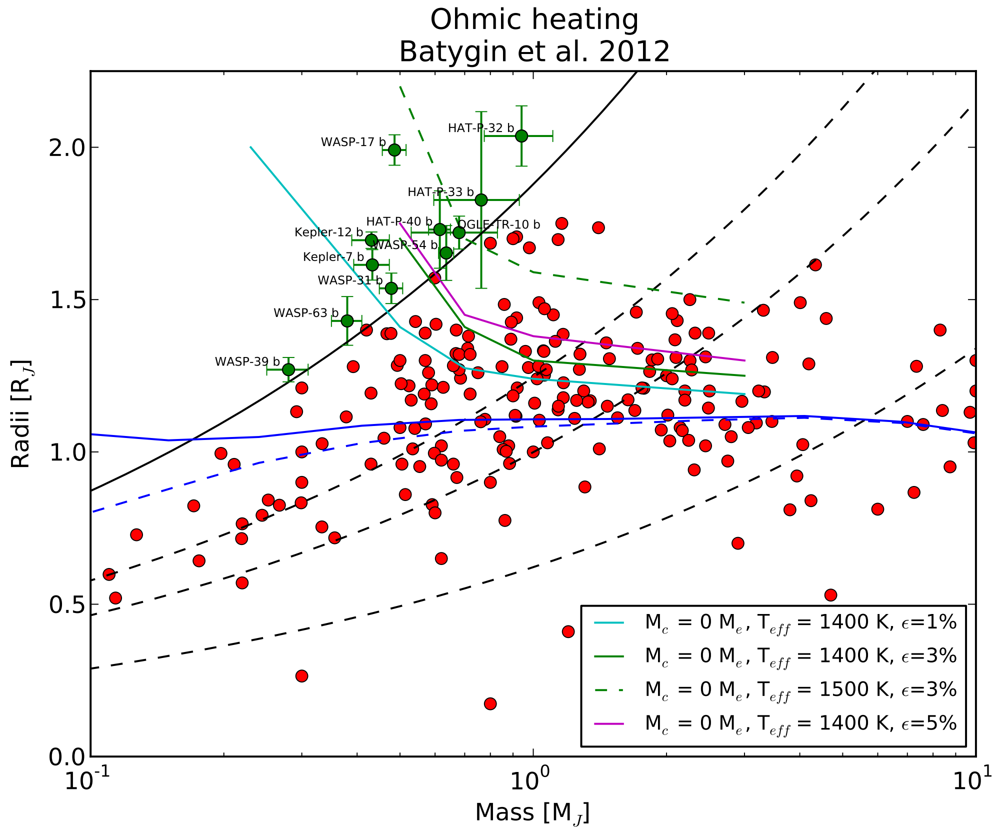

Figure 4.8: The figure depicts the predicted radii as a function of mass, at a certain temperature, by the Ohmic dissipation. The colors indicate different efficiencies 1%, 3% and 5% being cyan, green and magenta, respectively. The dashed green line indicates an increase in temperature by 100 K. A higher temperature increases the amount of generated heating. The models are built on coreless exoplanets, thus indicating the upper limits of the model. The blue line is the same as in Figure 4.4 with the isodensities as in Figure 4.1.

The cyan line ($\epsilon \sim 1\%$) goes towards smaller masses than the higher efficiency. The reason is that higher efficiencies is predicted to lead the exoplanets into evaporation at these low masses ($< 0.5\mathrm{M_{Jup}}$), unless some form of stability is present, as a core mass (Batygin et al., 2011).

Figure 4.8 indicates that ohmic heating is strongly dependent on the stellar irradiation, which determines more-or-less the surface temperature of close-in exoplanets. Therefore a correlation between the radius inflation and stellar irradiation is expected (Perna et al., 2012). This correlation has as well been found by Demory and Seager (2011), and will be discussed in greater detail in section 5.2. A large scatter is as well predicted by Ohmic heating, because of its dependence on magnetic field strength and atmospheric opacity (Perna et al., 2012)[1].

The importance of ohmic dissipation can be neglected for equilibrium temperatures below 1700 - 1800 K if the magnetic field strength is similar to Jupiter, several Gauss (Perna et al., 2012)[2]. A stronger magnetic field would decrease the necessary equilibrium temperature for Ohmic dissipation.

4.2 Low-density exoplanets

The following section describes the low-density sample: All exoplanets with a density less than 0.2 g cm^{-3}. The list is constantly being updated by a network of astronomers at Open Exoplanet Catalogue (Rein, 2012). The exoplanet, `Kepler-30 d` has recently been published (Sanchis-Ojeda et al., 2012) and added to the database, and it has as well a density below 0.2 g cm^{-3}. This exoplanet differs by the other in the sample due to its Neptunian mass of 22 $M_\oplus$, but with a Jupiter-like radii of, $0.8R_{\mathrm{Jup}}$. It is as well the only planet in our sample that has companion planets in the system.

In this section, I primarily focus on the inflated Hot-Jupiters in our sample, since their larger size make them good targets for observing exo-atmosphere by spectroscopy (Burrows, 2013a). One of the exoplanets in the sample has recently had its atmosphere observed (Demory et al., 2013)

Each section ends with a table, which describes the physical properties of the star and planet. Some tables will contain updated values of the planets parameters to indicate the change due to improved observations. All values of stars in the tables are described by assuming circular orbits, unless a footnote informs otherwise. The exoplanets semi-major axis is as well based on circular orbit, while the database, *http://openexoplanetcatalogue.com*, uses values based on eccentric orbits[3].

The most important values for each system are given in table 4.14 at page 81 and can be used for comparison.

[1] Ohmic power scales as B_0^2, and a higher atmospheric opacity might create a feedback for the magnetic drag, reducing the exponent of the magnetic field (Perna et al., 2012)

[2] It is important to note that the term, T_{irr} used by Perna et al. (2012) is exactly the same as the equilibrium temperature

[3] The semi-major axis is more or less similar for low eccentricities ($e < 0.2$)

4.2.1 HAT-P-32 b

The exoplanet, `Hat-P-32b`, orbits around an active F or G star, which produces a high jitter. This complicates the precision of the stellar and planetary parameters; since jitter complicates the methods of ruling out blending scenarios and determining a precise eccentricity, as described in section 3.3.1. The period of photometric observations spanned from 9/2005 to 4/2007.

If a circular orbit is assumed, the planet's density would be $0.20^{+0.048}_{-0.045}$ cgs, while an elliptic orbit of $e \approx 0.148$ will increase the radius, thus decreasing the density to $0.15^{+0.054}_{-0.042}$ cgs. It is crucial to define a precise eccentricity, since assuming circular orbits can underestimate the true parameters (Hartman et al., 2011). The eccentricity is usually found by detailed spectroscopic analysis or time-transit variations, as described in section 2.2.

If the stellar host is observed to be active, then mid-IR telescopes can be used instead, since IR-wavelengths are less affected than the optical wavelengths for the active FGK-stars (Sada et al., 2012). The advantage of mid-IR spectroscopy is the lower stellar limb-darkening coefficients, which increases the precision of photometric data.

`HAT-P 32` is classified to lie between the F and G-stellar type, due to its high luminosity and temperature. It is a fairly young system, 2.7 Gyr, with a more-or-less solar metallicity ($Z \approx 0.90\ Z_\odot$). The close-in orbiting exoplanet is one of the most inflated exoplanets. It is the only exoplanet that requires internal core heating above 10^{29} according to Figure 4.5, and a larger core mass of 10 $M_\oplus$ requires a heating in the order of 10^{30}, as seen in Figure 4.6. The tidal circularization has been calculated to last 2 Myr for a tidal-dissipation parameter of 10^6 (Hartman et al., 2011). The short age indicates that the orbit should be circular, if tidal interactions would be initiated by a planet-disk interaction. On the other hand, a companion planet might scatter the planet into the currently observed eccentricity.

In the case of ohmic heating, an evaporation is expected to occur within the exoplanet, as seen in Figure 4.7, and its large mass requires a larger efficiency than 3% to obtain a radii of 2.037 R_{Jup}. An evaporation could be omitted by a core mass, so the planet might contain a core mass that keeps in stable, if the case of ohmic heating is applied.

An enhanced opacity would stall the contraction, and a thicker opacity is required, since a solar metallicity would lead to evaporation, as seen in Figure 4.5. A combination of the enhanced opacity and tidal heating could be a viable solution.

Star	
Object name	HAT-P-32
	GSC 3281-00800
Magnitude	V $\sim$ 11.289
Spectral class	F/G
Mass	1.16 ± 0.04 $M_\odot$
Radii	1.22 ± 0.02 $R_\odot$
T_{eff}	6207 ± 88 K
log $g_\star$	4.33 cgs
[Fe/H]	-0.04 ± 0.08
$L_\star$	1.94 ± 0.15 $L_\odot$
vsin i	20.7 km s^{-1}
Age	2.7 ± 0.8 Gyr

Planet	
Object name	HAT-P-32 b
Semi-major axis	0.034 AU
Period	2.15008 ± 10^{-6}d
mid-IR [a]	$2.1500103 \pm 3\ 10^{-7}$d
Semi-amplitude	$122.8\pm$ 23.2 ms^{-1}
circular orbit	
Mass	0.86 ± 0.164 M_{Jup}
Radii	1.789 ± 0.025 R_{Jup}
Density	0.19 ± 0.04 *cgs*
T_{eq}	1786 ± 26 K
elliptic orbit, $e \sim 0.163$	
Mass	0.941 ± 0.166 M_{Jup}
Radii	2.037 ± 0.099 R_J
Density	$0.14^{+0.03}_{-0.02}$ *cgs*
T_{eq}	1888 ± 51 K

[a]Value taken from Sada et al. (2012)

Table 4.2: An overview of the system. Values were taken from Hartman et al. (2011); Sada et al. (2012)

4.2.2 HAT-P-33 b

The exoplanet, `HAT-P-33 b`, was published with the discovery of `HAT-P-32 b`. It orbits a similar star, which is classified as a late-F type star. The host star does not show any chromospheric activity, which increases the precision of the spectral-results[4].

`HAT-P-33 b` is the third largest exoplanet in our sample, and is more than 50% larger than the predicted radii of stellar irradiated models, see Figure 4.4. The metallicity is a bit larger than the solar metallicity, so a thicker opacity of the atmosphere might be apparent. A core heating of 10^{28} is required according to the models of Burrows et al. (1997), while models of Miller et al. (2009) require a larger heating but in the same order, see Figure 4.5 and 4.6, respectively.

[4]Notice the difference in semi-amplitude of `HAT-P-32 b` and `HAT-P-33 b`; $122.8\pm$ 23.2 ms^{-1} and $82.7\pm$ 10.8 ms^{-1}

The tidal heating to luminosity ratio shows a small or negligible effect of tidal heating on the order of 10^{-2}. The circularization timescale has been calculated to 30 Myr (Hartman et al., 2011), which concludes the same statement as for `HAT-P-32 b`; Planet-disk interactions would have circularized the exoplanet at its current age.

A process that might be more probable would be the ohmic heating, but an efficiency of 3% predicts the exoplanet to be in an evaporated state with a radii of $2.2R_{\mathrm{Jup}}$. A lower efficiency would reduce the predicted radii at current age of the exoplanet and possibly avoid an evaporative state at the current age. The core mass might as described for the case of `HAT-P-32 b` also be a crucial factor of stabilizing the planet. (Batygin et al., 2011).

Star	
Object name	HAT-P-33
	GSC 2461-00988
Magnitude	V $\sim$ 11.188
Spectral class	F8
Mass	1.375 $\pm$ 0.04 $M_\odot$
Radii	1.637 $\pm$ 0.03 $R_\odot$
T_{eff}	6446 $\pm$ 88 K
log $g_\star$	4.15 cgs
[Fe/H]	0.07 $\pm$ 0.08
$L_\star$	4.15 $\pm$ 0.33 $L_\odot$
vsin i	13.7 km s^{-1}
Age	2.3 $\pm$ 0.3 Gyr

Planet	
Object name	HAT-P-33 b
Semi-major axis	0.049 AU
Period	3.4744 $\pm$ 10^{-6}d
Semi-amplitude	82.7 $\pm$ 10.8 ms^{-1}
circular orbit	
Mass	0.762 $\pm$ 0.101 M_{Jup}
Radii	1.686 $\pm$ 0.045 R_{Jup}
Density	0.20 $\pm$ 0.03 *cgs*
T_{eq}	1782 $\pm$ 28 K
elliptic orbit, $e \sim 0.148$	
Mass	0.763 $\pm$ 0.117 M_{Jup}
Radii	1.827 $\pm$ 0.290 R_J
Density	$0.15^{+0.11}_{-0.05}$ *cgs*
T_{eq}	1838 $\pm$ 133 K

Table 4.3: An overview of the system. Values were taken from Hartman et al. (2011)

4.2.3 HAT-P-40 b

`Hat-P-40 b` is an inflated hot-Jupiter orbiting the star, `HAT-P-40`. The star has been observed for 7 years in total, and has a low jitter, thus easing the rule out of blend scenarios. Spectroscopy has been obtained by the Tillinghast Reflector Echelle Spectrograph (TRES) in a period of 84 days, resulting in 5 spectra (Hartman et al., 2012).

The inflated exoplanet has density of 0.15 ± 0.01 g cm^{-3} or 0.11 ± 0.02 g cm^{-3}, depending on circular or elliptical orbit, respectively. The close-in exoplanet, `HAT-P-40 b`, differs from `HAT-P-32b` by having a more evolved star at more or less same age due to the higher stellar mass. Evolved stars show a strong deficit in close-in exoplanets, which could indicate that these planets are in the process of being destroyed rather than newly formed (Hartman et al., 2012). The distribution of exoplanets as a function of stellar mass can be seen in Figure A.1 at page 114. It should be noted that more massive stars have a more violent history due to the short lifespan and are less abundant than less massive stars.

`HAT-P-40 b` has three orders lower ratio between its tidal heating and luminosity, thus disregarding the tidal heating effect. A lower tidal dissipation parameter would increase the tidal heating, but the parameter, Q_p, is proposed to lie in between 10^6 - 10^7 (Beaugé and Nesvorný, 2012; Ibgui and Burrows, 2009).

Figure 4.8 explains the appearance of the exoplanet by an efficiency of 3% and equilibrium temperature of 1500 K. The temperature of `HAT-P-40 b` is $\sim$ 300 K higher. A higher temperature requires an efficiency below 3%, since an evaporation could occur at these conditions with an efficiency of 3%, as seen on Figure 4.7. But again, it is not strictly right to assume that the equilibrium temperature equals the effective temperature (Baraffe et al., 2003; Spiegel and Burrows, 2013) due to the high incident flux, as described in Figure 4.14.

The large luminosity of the stellar host produces an incident flux of $2.27 \cdot 10^9$ erg s^{-1} cm^{-2}, which could be sufficient for evaporation of the exoplanet atmosphere, but then the same tendency should be seen in `HAT-P-32b`, which has a similar incident flux. Evaporation seems improbable for larger exoplanets due to the larger planet mass (Owen and Wu, 2013).

Star	
Object name	HAT-P-40
	GSC 3607-010280
Magnitude	V $\sim$ 11.69
Spectral class	
Mass	$1.512^{+0.45}_{-0.109}$ $M_\odot$
Radii	2.206 ± 0.061 $R_\odot$
T_{eff}	6080 ± 100 K
log $g_\star$	3.93 cgs
[Fe/H]	0.22 ± 0.10
$L_\star$	6.00 ± 0.61 $L_\odot$
vsin i	6.9 km s^{-1}
Age	$2.7^{+0.9}_{-0.3}$ Gyr

Planet	
Object name	HAT-P-40 b
Semi-major axis	0.0607 AU
Period	4.45724 ± 10^{-5}d
Semi-amplitude	58.1 ± 2.9 ms^{-1}
circular orbit	
Mass	0.615 ± 0.038 M_{Jup}
Radii	1.730 ± 0.062 R_{J}
Density	0.15 ± 0.01 *cgs*
T_{eq}	1770 ± 33 K
elliptic orbit, $e \sim 0.095$	
Mass	0.584 ± 0.035 M_{Jup}
Radii	1.900 ± 0.127 R_{J}
Density	0.11 ± 0.02 *cgs*
T_{eq}	1843 ± 60 K

Table 4.4: Brief overview of HAT-P-40b, values were taken from Hartman et al. (2012)

4.2.4 Kepler-7 b

`Kepler-7 b` orbits a quiet star with a mass of 1.36 $M_\odot$, radii of 2.02 $R_\odot$, and an age of 3.3 Gyr. However the stellar effective temperature is not much larger than the Suns, which could indicate that `Kepler-7` is on the end of its main-sequence. According to the Yonsei-Yale (YY) evolution tracks, the position of `Kepler-7` could be either before the hydrogen burning in the core is exhausted or with a lesser probability at the bottom of the Red-giant-branch (Latham et al., 2010). In the latter case, the mass and radii decrease but in a manner to keep the stellar density constant (12% by mass, 4% by radii). The lower stellar mass enforces a lower planetary mass by 8%, because of on the 2/3 power of the system mass dependency, see Equation (2.6). The lower stellar radii will in turn decrease the exoplanets radii by 4% due to the linear-relation (Latham et al., 2010), see Equation (2.1). The results in table 4.5 are given as a best guess by the YY-tracks and analyzing the spectra of FIbre-fed Echelle Spectrograph (FIES) using MOOG (Latham et al., 2010). MOOG is an analysis package as the earlier mentioned Spectroscopy Made Easy (SME) in Chapter 3.

The spectroscopy was made by FIES at the 2.5m Nordic Optical Telescope (NOT) (Latham et al., 2010). Newer observations by Demory and Seager (2011) make use of measurements near the eclipse to focus on transits and occultations with the ARizona Infrared image and Echelle Spectrograph (AIRES) and data by asteroseismology. These newer measurements focused on measuring the occultation depth to calculate a geometric albedo. The geometrical albedo can yield information about the atmospheric composition, as noted in a recent publication by Demory et al. (2013).

In our case, the measured parameters from asteroseismology lie in between of the results from FIES and AIRES, and are far more precise than those achieved by spectroscopy. The quiet nature of `Kepler-7` makes blending scenarios quite improbable.

`Kepler-7 b` has a smaller radii than the mentioned `HAT-P`-exoplanets, but its mass is correspondingly lower, thus keeping a density in the same range. The exoplanet has with a high confidence a circular orbit, which tells us that tidal heating has no or negligible effect on the inflated radii. This can also be seen on table 4.1, where as an eccentricity of 0.1 has been assumed in the database.

The ohmic dissipation can explain the occurrence by an efficiency lower than 3% with a temperature of 1500 K. The exoplanet has an equilibrium temperature of 1600 K, so a probable efficiency around 1% could be expected.

A recent publication by Demory et al. (2013) discusses the appearance of thick clouds on the surface of `Kepler-7 b`. New data indicates that cloud-models fit the observed lines, which could indicate that thick moving clouds might produce an enhanced opacity. These clouds are additional aided by the low surface gravity, which suppresses cloud sedimentation (Demory et al., 2013).

Star	
Object name	Kepler-7
KOI 97.01	2MASS J19141956+4105233
Magnitude	B ∼ 13.4 [c]
Spectral class	G0 [d]
Mass	$1.359 \pm 0.031 M_\odot$ [a]
Radii	$2.02 \pm 0.02\ R_\odot$ [a]
T_{eff}	5933 ± 44 K [b]
log $g_\star$	3.984 cgs [a]
[Fe/H]	0.11 ± 0.03[b]
$L_\star$	$4.15\ ^{+0.63}_{-0.54}\ L_\odot$ [b]
vsin i	4.5 km s^{-1} [d]
Age	3.3 ± 0.4 Gyr [a]

Planet	
Object name	Kepler-7 b
Semi-major axis	0.0623 AU
Period	$4.88548 \pm 4{\cdot}10^{-6}$d
Semi-amplitude	$43.1^{3.9}_{4.0}$ ms^{-1}
Demory and Seager (2011)	
Mass	$0.443\ ^{+0.041}_{-0.042}\ M_{\mathrm{Jup}}$
Radii	$1.614 \pm 0.015 R_J$
Density (*cgs*)	0.14 ± 0.01
T_{eq}	1628 ± 25 K
Latham et al. (2010)	
Mass	$0.433\ ^{+0.040}_{-0.041}\ M_{\mathrm{Jup}}$
Radii	$1.478^{+0.050}_{-0.051} R_J$
Density (*cgs*)	$0.166^{+0.019}_{-0.020}$
T_{eq}	1540 ± 200 K

Table 4.5: Values were taken from different sources; [a]Demory and Seager (2011), [b]Latham et al. (2010), [c]Cutri et al. (2003), [d]Ehrenreich and Désert (2011). It primarily differs between the older and newer results of Latham et al. (2010) (b) and Demory and Seager (2011) (a), respectively.

4.2.5 Kepler-12 b

`Kepler-12 b` is orbiting a slightly larger star than the Sun; with a mass of 1.16 $M_\odot$ star, radii of 1.483 $R_\odot$ and age of 4 Gyr. Blending scenarios have been dismissed by the Keck I telescope and a near infrared image by the Palomar Hale 200 inch telescope (Fortney et al., 2011b). Radial velocity measurements of `Kepler-12 b` have been made by HIRES in a timespan of two year, with one outlier, which was made near morning twilight and may be contaminated in larger degree than other RV-measurements.

The inflated radii of `Kepler-12 b` could be explained by circularization, which requires an initial eccentricity. But, precise transit measurements, with the scatter, show no signs of a larger planetary companion, which could enable planet-planet scattering (Fortney et al., 2011b). The circularization timescale is around 0.1 Gyr according to Equation (4.1), but the eccentricity is with a high confidence low, so the exoplanet might recently entered a circular orbit. Table 4.1 as well points against the tidal heating mechanism by the low ratio, and the value is calculated by an eccentricity of 0.1.

Ohmic dissipation might be able to explain the appearance of `Kepler-12 b` due to its temperature of 1482 K. According to Figure 4.8 an efficiency around 1% would be sufficient to explain the exoplanets appearance. A 3% efficiency could as well be the case as seen at the red 0.5 M_{Jup} line in Figure 4.7, since a lower mass and higher temperature would increase the expected radii to the observed 1.7 R_{Jup}.

Fortney et al. (2011b) make a comparison with `HD 209458 b`, because their mutual incident stellar flux is a like but a size difference of 20%[1]. The different physical appearance at same incident flux tells us that the heavy element enrichment might be different. A larger core mass would require a corresponding larger core heating to inflate a planet to a given radii, therefore Fortney et al. (2011b) proposes that the difference in radii might be due to the core mass. The difference in core heating between core masses can be seen in Figure 4.5 (0 $M_\oplus$) and Figure 4.6 (10 $M_\oplus$).

An enhanced atmosphere might as well help in increasing the radii of an exoplanet by stalling the cooling rate.

Star	
Object name	Kepler-12
KOI 20.01	GSC 03549-00844
Magnitude	V ∼ 13.8
Spectral class	G0
Mass	$1.166\ ^{+0.051}_{-0.054}\ M_\odot$
Radii	$1.483\ ^{+0.025}_{-0.029}\ R_\odot$
T_{eff}	5947 ± 100 K
log $g_\star$	4.175 cgs
[Fe/H]	$+0.07 \pm 0.04$
$L_\star$	$2.47^{+0.26}_{-0.25}\ L_\odot$ [a]
vsin i	0.8 km s^{-1}
Age	$4.0^{+0.3}_{-0.2}$ Gyr

[a] Value has been calculated by assuming a blackbody radiation

Planet	
Object name	Kepler-12 b
Semi-major axis	0.0555 AU
Period	$4.43796 \pm 0.2 \cdot 10^{-6}$d
Semi-amplitude	$48.2^{4.4}_{4.3}\ ms^{-1}$
Fortney et al. (2011b)	
Mass	$0.431^{+0.041}_{-0.042}\ M_{Jup}$
Radii	$1.695^{+0.025}_{-0.029}\ R_J$
Density (*cgs*)	$0.111^{+0.011}_{-0.009}$
T_{eq}	1482.78 ± 40 K
Open Exoplanet Catalogue	
Eccentricity	$0.1\ (< 3\sigma)$
Mass	0.433 M_{Jup}
Radii	1.614 R_J

Table 4.6: Values are taken from Fortney and Nettelmann (2010) and Open Exoplanet Catalogue

[1] `Kepler-12b`: 1.70R_{Jup}, `HD 209458 b` : 1.38R_{Jup}

4.2.6 WASP-17 b

WASP-17 is a well studied system, which has been investigated by multiple groups: Anderson et al. (2010); Doyle et al. (2013); Southworth et al. (2012). The star is classified as a F6V star; with a mass and radii of 1.286 $M_\odot$ and 1.583 $R_\odot$, and an age of 2.7 Gyr. The evolutionary stage of WASP-17 can be discussed by the results of the observations; 1.38$R_\odot$ (Anderson et al., 2010) and 1.58$R_\odot$ (Southworth et al., 2012). I would predict the star slowly entering a RGB-phase due to the surface gravity difference between both groups, which is not within the uncertainties, 4.23$\pm$ 0.12 and 3.16 cm$\pm$ 0.20 s^{-2}, respectively. This might turn the class of the star towards IV, instead of V. Newer results by Doyle et al. (2013) predict a mass of 1.29$M_\odot$ and radii of 1.27$R_\odot$, but I disregard these results due to their larger uncertainty on the radii of the star, compared to the values of Southworth et al. (2012). It should be noted that the last mentioned authors used the Danish, 1.54m Telescope on La Silla in Chile, while Doyle et al. (2013) used high signal-to-noise ratio (SNR) HARPS spectra, but they used calibration models of (Doyle et al., 2013, cf. *Torres et al. (2010)*) to obtain the mass and radius. The difference could be due to different applied calibration models and/or stellar models, like the ones of (Yi et al., 2001). The different stellar evolution tracks are discussed in Southworth (2010).

Two tables have been made, indicating how the derived physical parameters may change due to the models used for the star (Southworth et al., 2012, tables 5-6), where the latter table is depicted on the next page. WASP-17 b may contain VO and TiO gases in the atmosphere (Anderson et al., 2010), which could increase the opacity of the atmosphere. The increased opacity of the atmosphere would increase the radii above the stellar irradiation models of Fortney et al. (2007). But according to Figure 4.4 the radii of WASP-17 b is almost twice the predicted of the stellar irradiation model, so a massive opacity must be taken into account to predict the observed radii.

A process that could increase the radii would be the circularization from an eccentric orbit, as described in section 4.1.2. Tidal heating could produce a maximum radius of 2 R_{Jup} for WASP-17b by using the models of Ibgui and Burrows (2009), if it evolved from a highly eccentric and close-in orbit with moderate tidal dissipation[1]. It is as well believed that a companion planet might have created a planet-planet scattering, thus creating an inclined orbit as is seen for most of the close-in planets, by the Kozai mechanism (Anderson et al., 2010). The Kozai mechanism requires a three-body system, in our case; the stellar host, the exoplanet and a perturber (the

[1] Values: e$\approx$ 0.79, $Q_p \approx 10^{6.55}$ and $Q_\star \approx 10^{7.0}$

	This work (final)	A10 (Case 1)	A10 (Case 2)	A10 (Case 3)	Triaud et al. (2010)	A11
e	0.0 adopted	$0.129^{+0.106}_{-0.068}$	$0.237^{+0.068}_{-0.069}$	0.0 adopted	0.0 adopted	$0.028^{+0.015}_{-0.018}$
M_A ($M_\odot$)	$1.286 \pm 0.076 \pm 0.020$	1.20 ± 0.12	1.16 ± 0.12	1.25 ± 0.13	1.20 ± 0.12	1.306 ± 0.026
R_A ($R_\odot$)	$1.583 \pm 0.040 \pm 0.008$	$1.38^{+0.20}_{-0.18}$	$1.200^{+0.081}_{-0.080}$	1.566 ± 0.073	$1.579^{+0.067}_{-0.060}$	1.572 ± 0.056
$\log g_A$ (cgs)	$4.149 \pm 0.014 \pm 0.002$	4.23 ± 0.12	4.341 ± 0.068	$4.143^{+0.032}_{-0.031}$		4.161 ± 0.026
ρ_A ($\rho_\odot$)	0.324 ± 0.012	$0.45^{+0.23}_{-0.15}$	$0.67^{+0.16}_{-13}$	$0.323^{+0.035}_{-0.028}$	$0.304^{+0.016}_{-0.020}$	0.336 ± 0.030
M_b (M_{Jup})	$0.477 \pm 0.033 \pm 0.005$	$0.490^{+0.059}_{-0.056}$	$0.496^{+0.064}_{-0.060}$	$0.498^{+0.059}_{-0.056}$	$0.453^{+0.043}_{-0.035}$	0.486 ± 0.032
R_b (R_{Jup})	$1.932 \pm 0.052 \pm 0.010$	$1.74^{+0.26}_{-0.23}$	1.51 ± 0.10	1.97 ± 0.10	$1.986^{+0.089}_{-0.074}$	1.991 ± 0.081
g_b ($\mathrm{m\,s^{-2}}$)	3.16 ± 0.20	$3.63^{+1.4}_{-0.9}$	$5.0^{+1.1}_{-0.9}$	$2.92^{+0.36}_{-0.33}$		2.81 ± 0.27
ρ_b (ρ_{Jup})	$0.0618 \pm 0.0048 \pm 0.0003$	$0.092^{+0.054}_{-0.032}$	$0.144^{+0.042}_{-0.031}$	$0.0648^{+0.0106}_{-0.0090}$		0.0616 ± 0.0080
T'_{eq} (K)	1755 ± 28	1662^{+113}_{-110}	1557 ± 55	1756^{+26}_{-30}		1771 ± 35
Θ	$0.0196 \pm 0.0012 \pm 0.0001$					
a (au)	$0.05125 \pm 0.00099 \pm 0.00027$	$0.0501^{+0.0017}_{-0.0018}$	$0.0494^{+0.0017}_{-0.0018}$	$0.0507^{+0.0017}_{-0.0018}$	0.0500 ± 0.0017	0.05150 ± 0.00034
Age (Gyr)	$2.7^{+0.6}_{-1.0}{}^{+0.6}_{-0.6}$	$3.0^{+0.9}_{-2.6}$	$1.2^{+2.8}_{-1.2}$	$3.1^{+1.1}_{-0.8}$		2.65 ± 0.25

Table 4.7: A figure illustrating how results change by authors and with newer measurements but lie close within the uncertainties. A10 corresponds to Anderson et al. (2010), where case 1 was the favorable. A11 corresponds to Anderson et al. (2011b). The figure is taken from Southworth et al. (2012)

object creating eccentric orbits). The perturber has to have a larger mass than the exoplanet in between to perturb it into eccentric orbits. Future observations could investigate if close-in exoplanets have exoplanets at larger distances.

Southworth et al. (2012) disregards tidal dissipation as a viable explanation due to the planets circular orbit. Their newer observational occultations in infrared by Spitzer have shown that Anderson et al. (2010) found a smaller period thus achieving a wrong mid-occultation, therefore misleading results.

Detection of the Rossiter-McLaughin effect indicate that `WASP-17 b` is in a retrograde orbit, which could be indicative of a violent formation-history involving planet-planet or planet-star interactions (Anderson et al., 2010). The misalignment between the spin axis of the star and planet can be used to investigate migration theories, since different theories predict different alignments, i.e. migration by interaction of a giant planet with disk is expected to preserve spin-orbit, but migration by planet-planet interaction is able to produce significant misalignment (Anderson et al., 2010).

The equilibrium temperature of the exoplanet is 1755 K, which tells us that Ohmic dissipation could explain the radii of 1.9 R_{Jup}. It should be remembered that the models given in Figure 4.8 are based on a core mass of 0 $M_\oplus$, to estimate the upper limit. A larger core mass would reduce the predicted radii of the ohmic heating.

Figure 4.7 depicts that an exoplanet of such low mass and high temperature might be on its path to evaporation; but as was mentioned, these models are built on a core-less planet, so a core mass will counter the evaporation.

The given values in table 4.8 show the primordial results of Anderson et al. (2010) and the newer and more precise results, as discussed in the entry of this description.

Star	
Object name	WASP-17
	TYC 6787-1927-1
Magnitude	V ∼ 11.6
Spectral class	F6V[a]
Mass	1.286 ± 0.076 $M_{\odot}$
Radii	1.583 ± 0.04 $R_{\odot}$
T_{eff}	6550 ± 100 K
log $g_{\star}$	4.149 cgs
[Fe/H]	-0.19 ± 0.09 [b]
	-0.25 ± 0.09 [a]
$L_{\star}$	4.13 ± 0.5 $L_{\odot}$
vsin i	9.8 km s^{-1} [c]
Age	$2.7^{+0.6}_{-1.0}$ Gyr [d]

Planet	
Object name	WASP-17 b
Semi-major axis	0.0512 AU
Period	$3.73544 \pm 0.7 \cdot 10^{-5}$d
Semi-amplitude	$56.9^{0.0055}_{0.0053}$ ms^{-1}
Eccentricity	$0.129^{+0.106}_{-0.068}$
Anderson et al. (2010)	
Mass	$0.490^{+0.059}_{-0.056}$ M_{Jup}
Radii	$1.74^{+0.26}_{-0.23}$ R_J
Density (*cgs*)	$0.12\ ^{+0.07}_{-0.04}$
Southworth et al. (2012)	
Mass	$0.477 \pm$ 0.03 M_{Jup}
Radii	$1.932 \pm$ 0.05 R_{Jup}
Density	0.087*cgs*
T_{eq}	1755 ± 28 K

[a] Anderson et al. (2010)
[b] Anderson et al. (2011b)
[c] Doyle et al. (2013)
[d] Southworth et al. (2012)

Table 4.8: Values are taken from various of sources; Anderson et al. (2010, 2011b); Doyle et al. (2013); Southworth et al. (2012). Most of them are taken from Anderson et al. (2010), except for the values in the footnote or the ones in Figure 4.7.

4.2.7 WASP-31 b

The exoplanet, `WASP-31 b`, is similar to `WASP-17 b` by mass and metallicity. The stellar host of both exoplanets has almost the same mass, but differ on radii and age. The lower radii with age of `WASP-31` could indicate that it is at an earlier stage of evolution than `WASP-17`. The exoplanets differ by a radii of 0.5 R_{Jup}, even though `WASP-31 b` is younger than `WASP-17 b`. Figure A.4 depicts the predicted radii of planets as a function of age, and it is seen that the observed radii of `WASP-31 b` is above the predicted value.

The tidal dissipation could have occurred, since the tidal circularization lasts 0.1 Gyr using $Q_p = 10^{6.55}$, which lasts 10% of the exoplanets lifetime. The ratio of tidal heating to luminosity is non existent due to the assumed circular orbit, but if the upper limit eccentricity is taken, then it is still two orders below a unity.

Ohmic dissipation could be applied without ending in evaporation, as the case of `WASP-17 b` with a 0 $M_\oplus$ core. The exoplanets appearance can almost be explained by the cyan colored line in Figure 4.8, which is for 1400 K. The planet has a temperature 100 K higher, which would probably lift the line as the dashed green line, so an efficiency lower than 1% would explain the observed radii. `WASP-31 b` would as well avoid evaporation due to the lower temperature and efficiency.

It should be noted that the age estimated in table 4.9 is taken by an interpolation and lithium abundance, thus the large uncertainty, since the lithium measurements are weak due to the spectral class of the star, as described in section 3.4.1.

Star	
Object name	WASP-31
	2MASS 11174477-1903521
Magnitude	V ∼ 11.7
Spectral class	F7V
Mass	1.163 ± 0.026 $M_\odot$
Radii	1.252 ± 0.033 $R_\odot$
T_{eff}	6302 ± 102 K
log $g_\star$	4.308 cgs
[Fe/H]	-0.20 ± 0.09
$L_\star$	2.22 ± 0.28 $L_\odot$
vsin i	7.9 ± 0.6 km s^{-1}
Age	$1^{+3}_{-0.5}$ Gyr

Planet	
Object name	WASP-31 b
Semi-major axis	0.0470 AU
Period	$3.4059 \pm 0.5 \cdot 10^{-5}$d
Semi-amplitude	58.1 ± 3.4 m s^{-1}
Eccentricity	< 0.13 ; 3σ
Anderson et al. (2011a)	
Mass	0.478 ± 0.029 M_{Jup}
Radii	1.549 ± 0.050 R_J
Density (*cgs*)	0.129 ± 0.014
T_{eq}	1575 ± 32 K
Open Exoplanet Catalogue	
Mass	0.478 M_{Jup}
Radii	1.537 R_{Jup}
Density	0.175 *cgs*

Table 4.9: Values are taken from Anderson et al. (2011a)

4.2.8 WASP-39 b

The exoplanet, `WASP-39 b`, has a mass corresponding to that of Saturn ($\sim 1/3 M_{Jup}$), but 50% larger radii. It's orbiting a late G-type Star, which is observed by the lack of Lithium-Lines. The old age indicates lower stellar activity, which makes the results achieved more precise. The older age and size of the stellar host also indicates that the models of Fortney et al. (2007) would overestimate the predicted radii.

Tidal dissipation cannot explain the inflated state due to the non-observed eccentricity, with the relatively large age of the star ($\sim$ 9 Gyr). The stellar age is, as earlier discussed in section 3.4.1, very uncertain, but even with its lowest value, the age becomes 5 Gyr, and such a late circularization is improbable.

The exoplanet also has one of the lowest equilibrium temperature in our low density sample, which makes it an interesting candidate for Ohmic dissipation. An efficiency of 1% and temperature of 1400 K would predict a radii around $1.75\mathrm{R}_{\mathrm{Jup}}$, but a temperature of 1100 K would greatly reduce the predicted radii. It is doubtful if the exoplanet can receive heating by ohmic dissipation due to the low temperature (Perna et al., 2012). Any form of evaporation by ohmic heating is as well improbable due to the low temperature. The exoplanet lies just at the boarder of the inflated-exoplanet which is predicted to be above 2×10^8 erg s^{-1} cm^{-2} (Demory and Seager, 2011).

The required core heating to inflate the radii is around 10^{26} erg s^{-1} according to Figure 4.5. If I calculate the heating the planet should experience by gravitational contraction, $\frac{G_{pot}}{t_{age}}$, then I achieve a heating of 7.5×10^{24} erg s^{-1}, which is two-orders lower. The core heating model of Miller et al. (2009) requires 10^{25} erg s^{-1}, thus close to the calculated value. This could mean that a slightly thicker atmosphere could reproduce the radii of `WASP-39 b`, i.e. stellar luminosity.

If a lower limit of the radii is taken by a 3σ confidence level, then it still does not reach the stellar irradiation model, see Figure 4.4, since it as well will be lowered due to the physical properties of `WASP-39`.

Star	
Object name	WASP-39
Magnitude	V $\sim$ 12.11
Spectral class	G8
Mass	0.93 $\pm$ 0.03 $M_\odot$
Radii	0.895 $\pm$ 0.023 $R_\odot$
T_{eff}	5400 $\pm$ 150 K
log $g_\star$	4.503 cgs
[Fe/H]	-0.12 $\pm$ 0.10
$L_\star$	0.612 $L_\odot$
vsin i	1.4 $\pm$ 0.6 km s^{-1}
Age	9.0^{+3}_{-4} Gyr

Planet	
Object name	WASP-39 b
Semi-major axis	0.0486 AU
Period	4.0552 $\pm 1.0 \cdot 10^{-5}$d
Semi-amplitude	38 $\pm$ 4 m s^{-1}
Eccentricity	0
Faedi et al. (2011))	
Mass	0.28 $\pm$ 0.03 M_{Jup}
Radii	1.27 $\pm$ 0.04 R_J
Density (*cgs*)	0.181 $\pm$ 0.014
T_{eq}	1116^{+33}_{-32}

Table 4.10: Stellar and planet parameters are based on circular orbit. Values are taken from Faedi et al. (2011)

4.2.9 WASP-54 b

The exoplanet, `WASP-54 b`, orbits an old F9 star. This star has the lowest metallicity in the sample, which supports the idea of having low core masses for inflated planets. Figure 4.4 predicts a radii of 1.1 R_{Jup} for an exoplanet with no core mass at 0.045 AU for a Solar-type star, but this is not the case for `WASP-54 b`. The exoplanet is 1.65 R_{Jup} with a star larger and more luminous than the Sun.

Tidal dissipation could be a factor due to the eccentric orbit, but the tidal heating ratio is two orders below a unity, thus another mechanism must be responsible for the inflated radii. The circularization timescale is on the order of 0.15 Gyr, which is an order lower than the current age, which increases the improbability of a recent circularization. The large temperature of the exoplanet could indicate that ohmic heating could be responsible for the inflation, but the exoplanets would not exist if the efficiency was above 3%. So a low level of efficiency should be assumed for the high temperature to explain the exoplanets radii.

Another mechanism that `WASP-54 b` can be affected by, is the evolution of the star. The old F9 star has recently increased its radii by more than 60%, which could inflict drag forces upon `Wasp-54 b`. These drag forces will affect the orbital radius, which could heat up the exoplanet and make it appear younger and larger (Faedi et al., 2013). An orbital decay could occur if the stellar material were to block the orbital path, but the Roche lobe limit is still within the stellar radii, thus a larger orbital decay is not predicted. But, severe interactions are predicted since the inflated radii of the star fills up 15% of the orbital path. Regular period-determinations should indicate if the planet is affected by the additional material ejected by the star, since if orbital decay occurs, the period should be decreasing as the exoplanet spirals inwards.

Star	
Object name	WASP-54
Magnitude	V $\sim$ 10.42
Spectral class	F9
Mass	1.201 $\pm$ 0.035 $M_{\odot}$
Radii	1.80 $\pm$ 0.10 $R_{\odot}$
T_{eff}	6100 $\pm$ 100 K
log $g_{\star}$	4.2 cgs
[Fe/H]	-0.27 $\pm$ 0.08
$L_{\star}$	4.03 $L_{\odot}$
vsin i	4.0 $\pm$ 0.8 km s^{-1}
Age	$4.4^{+7.4}_{-2.7}$ Gyr

Planet	
Object name	WASP-54 b
Semi-major axis	0.0497 AU
Period	3.6936 $\pm 1.0 \cdot 10^{-5}$d
Semi-amplitude	73 $\pm$ 2 m s^{-1}
Circular orbit	
Mass	0.626 $\pm$ 0.023 $M_{\rm Jup}$
Radii	1.65 $\pm$ 0.09 $R_{\rm J}$
Density (*cgs*)	0.184 $\pm$ 0.014
T_{eq}	1742^{+49}_{-69}
Eccentric, e $\sim$ 0.067	
Mass	0.636 $\pm$ 0.025 $M_{\rm Jup}$
Radii	1.653 $\pm$ 0.09 $R_{\rm Jup}$
Density	0.187 *cgs*

Table 4.11: Stellar parameters are based on circular orbit. Values are taken from Faedi et al. (2013)

4.2.10 WASP-63 b

The exoplanet was observed in a period of 4 years by photometry and a year of radial velocity measurements (24 points). The stellar spectral type with the radii of the star indicates that it has evolved off the main sequence track with an age of $\sim$ 8 Gyr. This has been shown by making a modified H-R diagram ($\rho_{\star}^{-1/3}$ versus T_{eff}) (Hellier et al., 2012, cf. Fig. 8).

The exoplanet reminds a bit of `WASP-39 b`, but with larger mass, radii and equilibrium temperature. The latter parameter can be investigated with the ohmic heating to give an upper boundary of 1.6 $R_{\rm Jup}$ for $\epsilon = 1\%$ (for T = 1400 K). The planets radii is 1.43 R_{Jup}, so a possible core mass might reduce the predicted radii of ohmic heating. A more massive core might be probable due to the larger solar-metallicity of the system.

Since this star follows the Red Giant Branch path; it might inflate its planet by the ejected material, as `WASP-54`. If the 3σ upper limit eccentricity is applied, then the tidal heating ratio from section 4.1.2 is on the order of 10^{-2}, but the old age would still make tidal circularization doubtful, lasting only 0.3 Gyr. The core heating models expect both a similar heating of 3-5$\times$ 10^{26} erg s^{-1}, which is one order higher than calculated by the gravitational potential.

Star	
Object name	WASP-63
	2MASS 06172074-3819237
Magnitude	V $\sim$ 11.2
Spectral class	G8
Mass	1.32 $\pm$ 0.05 $M_\odot$
Radii	$1.88^{+0.10}_{-0.06}$ $R_\odot$
T_{eff}	5570 $\pm$ 90 K
log $g_\star$	4.01 cgs
[Fe/H]	0.08 $\pm$ 0.07
$L_\star$	3.06 $L_\odot$
vsin i	3.0 $\pm$ 0.6 km s^{-1}
Age	6.0^{+5}_{-3} Gyr

Planet	
Object name	WASP-63 b
Semi-major axis	0.0574 AU
Period	4.378 $\pm 1.0 \cdot 10^{-5}$d
Semi-amplitude	39 $\pm$ 3
Eccentricity	<0.22 at 3σ
	0 (adopted)
Hellier et al. (2012)	
Mass	0.38 $\pm$ 0.03 M_{Jup}
Radii	$1.43^{+0.10}_{-0.06} R_J$
Density (*cgs*)	0.17 $\pm$ 0.03
T_{eq}	1540 $\pm$ 40 K

Table 4.12: Stellar and planet parameters are based on circular orbit. Values are taken from Hellier et al. (2012)

4.2.11 OGLE-TR-10 b

The exoplanet, `OGLE-TR-10 b`, is the only one from the survey of OGLE transits with density below 0.2 g cm^{-3}. The parameters of the exoplanet, `OGLE-TR-10 b`, have been heavily debated from 2005 till 2007(Pont et al., 2007). Values in radii have ranged from 1.06 R_{Jup} to 1.54 R_{Jup}, due to observational difficulties. The photometric problem arises due to the view of the OGLE-III survey being towards the Galactic Bulge.

Results of `OGLE-TR-10 b` should be taken with concern due to bad spectroscopies (Southworth, 2010)[1]. The problem with spectroscopy is also seen in table 2 of Pont et al. (2007), where 4 different results are given for the mass. The problem could be due to the view towards the Galactic Bulge; which decreases the S/N of spectra.

The mechanisms for the inflation of the exoplanet will be omitted, since the results are doubtful. An interesting feature of `OGLE-TR-10` is that its metallicity is by far larger than the second largest, which is `Kepler-30 d`. If the metallicity is true, then it might be a sign of a thick opacity or/and a heavy core mass. The models of Ohmic heating would predict to evaporate according to Figure 4.7, but a heavy core mass would keep the planet intact.

Star[a]	
Object name	OGLE-TR 10
Magnitude	V ~ 15.7
Spectral class	G2V
Mass	1.277 ± 0.082 $M_\odot$
Radii	1.52 ± 0.010 $R_\odot$
T_{eff}	5960 ± 100 K [b]
log $g_\star$	4.178 cgs
[Fe/H]	0.15 ± 0.1 [b]
`OEC`	0.28
$L_\star$	2.62 $L_\odot$
vsin i	...
Age	$3.1^{+3.3}_{-0.7}$ Gyr

[a]Values of Magnitude and Spectral class were taken from `simbad`

Planet	
Object name	OGLE-TR-10 b
Semi-major axis	0.04516 AU
Period	$3.10129 \pm 1.0 \cdot 10^{-5}$d [b]
Semi-amplitude	...
Eccentricity	0 (adopted)
Pont et al. (2007)	
Mass	0.63 ± 0.14 M_{Jup}
Radii	1.22 ± 0.07 R_J
Density (*cgs*)	0.46
Southworth (2010)	
Mass	0.68 ± 0.15 M_{Jup}
Radii	1.706 ± 0.054 R_{Jup}
Density (*cgs*)	0.177
T_{eq}	1702 ± 54 K

Table 4.13: Values found by Pont et al. (2007) are marked,[b]. The other values are from Southworth (2010). OEC stands for Open Exoplanet Catalogue (Rein, 2012).

[1]This can be seen on page 1705, and in table 7

4.3 Conclusion of the eleven exoplanets

Most of the low-density exoplanets described above could be explained by Ohmic dissipation, due to its variable parameter, the efficiency ϵ, which is weakly constrained. This was as well pointed out in section 4.1.3.

In the case of tidal heating, table 4.1 gave us an idea of which exoplanets might be affected, and `HAT-P-32 b` was a plausible target for tidal heating. But tidal heating was out of the question for most of the cases; either due to circular orbits, a low ratio value on a factor lower than 10^{-2}, a low-tidal circularization timescale or an old age. But, it should be noted that the tidal circularization Equation 4.1 is built on an older model of tidal heating (Liu et al., 2008). It was possible to reach ratio between the luminosity and tidal heating to a unity, but that would require very low tidal dissipation parameters, which does not agree with the results of Beaugé and Nesvorný (2012). The authors propose a value between 10^6 and 10^7 based on simulations.

The simulations of Ohmic heating (Batygin et al., 2011; Perna et al., 2012) allow us to increase the power, and thus match a larger variety of exoplanets, and a 1% efficiency for most of these cases was accepted. But, the higher temperature exoplanets all suffered from the evaporation-problem, and larger core masses or enhanced opacities were necessary to keep these planets intact. Evaporation should according to Figure 4.7 occur fairly quickly depending on mass.

If an enhanced opacity should occur due to a super-solar metallicity, then it wouldn't explain the scatter of metallicity seen in our sample. Figure A.2 depicts four different values, where a large scatter in metallicity is seen for the large and irradiated exoplanets in our sample. The largest exoplanet in the sample, `HAT-P-32 b`, seems also to be one of the most metal poor ones, so a super-solar metallicity is highly unlikely. The largest exoplanets sitting on the metal-poor edge of the graph could be a sign of being core less. But, it is hard to say anything with such a scatter of exoplanets, which are all extreme case of inflation.

All exoplanets had temperatures above 1400 K, except for `Wasp-39 b`. The exoplanet has a similar distance to the host star as the other exoplanets, but the luminosity of the star was by far lower, which resulted in a lower incident flux of the planet. It is the only exoplanet, which could almost be explained by using our rough calculation of its internal energy, $\frac{G_{pot}}{t_{age}}$.

The only exoplanet which I have omitted is `Kepler-30 d` (Sanchis-Ojeda et al., 2012). This is due to the fact that it is a Neptune-mass planet, which has a low-density, but is not inflated, according to Figure 4.2. The low-density is probably due to evaporation, which occurs more likely in less massive exoplanets (Owen and Wu, 2013). The exoplanet has been confirmed during the work of this thesis, and is as well the only system found to have multiple-planetary companions. Its lower mass is probably the reason of it being in a multiple-planetary system, since scattering would require it to be a more massive object during the early formation stage. The other exoplanets, described here, are all as massive as Saturn and up to a Jupiter-mass, and these masses should have a larger probability of scattering planetary companions.

The exoplanets involved in a stellar evolution towards RGB can be tidally-interacted by the star, due to its increased size. So even though none of them show any signs of recent tidal interactions based on the models from section 4.1.2, then a more recent event by their stellar host might have inflated them as proposed by Faedi et al. (2013).

	HAT-P-32 b	HAT-P-33 b	HAT-P-40 b	Kepler-12 b	Kepler-30 d	Kepler-7 b	OGLE-TR-10 b	WASP-17 b	WASP-31 b	WASP-39 b	WASP-54 b	WASP-63 b
Mass (M_{Jup})	0.941	0.763	0.615	0.431	0.073	0.433	0.680	0.486	0.478	0.280	0.636	0.380
Radii (R_{Jup})	2.037	1.827	1.730	1.695	0.802	1.614	1.720	1.991	1.537	1.270	1.653	1.430
Density (g cm^{-3})	0.15	0.17	0.16	0.12	0.19	0.14	0.18	0.08	0.17	0.18	0.19	0.17
Distance (AU)	0.03	0.05	0.06	0.06	0.50	0.06	0.05	0.05	0.05	0.05	0.05	0.06
T_{eq} (K)	1677	1675	1615	1354	334	1487	1702	1518	1411	1022	1759	1540
Flux (erg s^{-1} cm^{-2})	2.62e9	2.60e9	2.22e9	1.09e9	4.05e6	1.60e9	1.89e9	2.24e9	1.29e9	0.35e9	1.34e9	1.27
Spectral type	F/G	F	F	G0	G	G0	G2V	F4	F	G8	F9	G8
Luminosity ($L_{\odot}$)	2.24	4.77	5.98	2.47	0.74	4.55	2.83	4.35	2.04	0.61	2.44	3.06
Metallicity [Fe/H]	-0.160	0.050	0.220	0.070	0.180	0.110	0.280	-0.190	-0.190	-0.120	-0.270	0.080
Timescale (Gyr)	2.7	2.3	2.7	4.0	2.0	3.3	3.1	2.7	1.0	9.0	4.4	6.0

Table 4.14: The table above illustrates the value from the Open Exoplanet Catalogue, and most of them should correspond to the newest updated values from the tables in section 4.2.

CHAPTER 5

Discussion and Conclusion

I have explained the reader about the problem regarding inflated exoplanets in Chapter 1 with a brief overview of exoplanets. Then in Chapter 2, I showed the different detection techniques, which could be used to obtain information on the exoplanets, as in; using the transits to predict the radii and radial velocity to estimate the minimum mass. Both values combined result in a density of the exoplanets, which indicates their composition. I tried to investigate data, which I thought was inflated in Chapter 3, but with time I learned that these exoplanets are not inflated, and instead I looked into the exoplanets with the lowest density, since these exoplanets must be inflated in some sort of way. In Chapter 4, I started investigating mechanisms that could provide the heating necessary to provide these large radii, that gave the low densities. I tried to analyze each exoplanet, one-by-one, just to experience that some might have evaporated by models of Ohmic heating, while others fitted it quite well. But, the low-density sample fitted only the models as the inaccurate parameter, efficiency, was adjusted. The same case applied the tidal heating, where the unknown parameter, tidal dissipation parameter, Q_p, could be 2-orders of magnitude different, which in turn could yield two-order of difference in tidal heating, and circularization timescale.

The following Chapter will look into some ideas, which I got during the project. I found an equation that predicts the equilibrium radii of exoplanets based on a heating-mechanism for a certain mass and distance from a Sunlike star. These calculations are shown in §5.1. Ideas of double-checking models with new candidates have also come to mind, so I investigate the lower flux limit on inflated exoplanets, which is believed to be for all exoplanets with an incident flux above $F_{pl} \approx 2 \cdot 10^8$ erg s^{-1} cm^{-2} (Demory and Seager, 2011; Spiegel and Burrows, 2013). The check-up is presented in §5.2.

I will as well express my thoughts on the mechanisms described in section 4.1, in §5.3. And a brief discussion on my data analysis is presented in §5.4.

5.1 The Equilibrium radii

One way to investigate the predictions of the models described in section 4.1 is to compare these results with an equation, which determines the radii based on a heating, as shown in Equation (5.1). The equation is built on simulations of a Sun-like star, but where I can vary the distance and mass of the exoplanet. The simulations stop when the equilibrium radii (R_{eq}) is reached, or in other words, when a exoplanets radii varies with less than 10^{-5} R_{Jup} a year.

Comparing all the given heating mechanisms from Chapter 4 will give us an estimate of how well they fit our sample of low-density exoplanets. I will assume that the mass of all exoplanets is 0.5 M_{Jup} and the distance is 0.04 AU, which is a fair assumption[1]. The only necessary parameter for the equation is the heating mechanism as a fraction of the insolation heating, which is the heating purely by the stellar host, $\dot{E} = \pi R_p^2 F_{inc} = R_p^2 \frac{L_\star}{4 \cdot a^2}$.

The equation is described as followed for a 0.5 M_{Jup} exoplanet at a proximity of 0.04 AU to a Sun-like star.

$$\frac{R_{eq}}{\mathrm{R_{Jup}}} = C_0 + C_1 x + C_2 x^2 + C_3 x^3 + C_4 x^4 \tag{5.1}$$

$$x = log\left(\frac{\dot{E}_{heating}}{\dot{E}_{insolation}}\right)$$

$$\text{Values for } C_n \qquad [6.42, 4.00, 1.25, 0.182, 0.0101]$$

If the mass would be raised to $1 M_{Jup}$, then the constants would be lowered except for C_4, as seen in (Liu et al., 2008, cf. Table 3)

[1] The average mass and distance of the sample is; 0.51 M_{Jup}, 0.08 AU. Without `Kepler-30 d` it is; 0.56 M_{Jup}, 0.05 AU

As the heating from the mechanisms in section 4.1 are inserted into Equation (5.1), the following figure is produced with the data of our low-density exoplanet sample (by green dots).

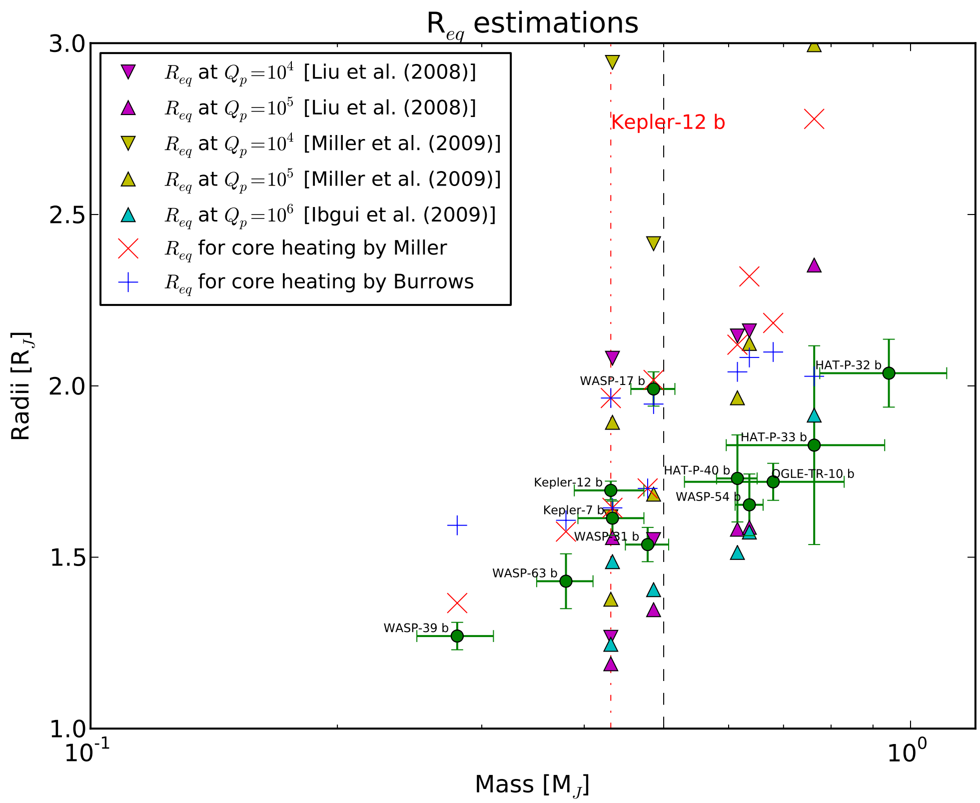

Figure 5.1: The figure depicts two different cases of heating; the tidal heating and core heating, triangles and crosses, respectively. The green dots represent the low-density sample with the name of the exoplanet and their errorbars. The R$_{eq}$ has been calculated by the model presented in Equation (5.1). The colors on triangles depict the model; purple, yellow and cyan with the authors as annotated. The shape of the triangle is a measure of "min-max" of the model, since as the tidal dissipation parameter becomes larger, the lower the prediction of the radii of the exoplanet.

It should be noted that the values further away from the dashed line are further away from the models initial values[1]. Values larger than 0.5 M$_{\rm Jup}$ will as well vary

[1] I mean the constants applied for Equation (5.1)

differently due to the different constants applied in Equation (5.1). Some values for the core heating are placed upon each-other, which is due to reading the data by hand from Figure 4.5 (blue cross) and Figure 4.6 (red cross). It could be noticed that the tidal heating model of Miller et al. (2009) is exactly the same as the one used by Ibgui and Burrows (2009).

The general trend is that Equation (4.2) (Miller et al., 2009) assumes larger tidal heating for same Q_p than the older tidal equation of Liu et al. (2008), which has an exoplanet radii dependency two orders lower. The latter author has taken the older equation into account, in which the tidal dissipation only depends on eccentric decay, while the newer equation states that the orbital decays needs to be taken into account as well (Fortney et al., 2011a; Jackson et al., 2008a).

An interesting feature is that models in Figure 5.1 fit the exoplanet, `Kepler-7 b`, see section 4.2.4. According to table 4.1, the effect of tidal dissipation should be negligible, but one should consider that the table was built upon the equations given in section 4.1.2, which takes additional effects into account, as the mentioned orbital decay. The newer tidal heating model fits within 3σ for a tidal dissipation of 10^6, but this would actually lower the tidal heating by one order, thus making the ratio even smaller.

It can be seen that the core heating models fit the exoplanet, `Kepler-7 b`, perfectly. One might assume that it could be due to the fact that `Kepler-7` is similar to our star, but this is not the case, as seen in section 4.2.4. The stellar parameters indicate a depleted hydrogen core, and movement towards the red giant branch. But the exoplanet is also 0.02 AU further away than for the assumed models of Figure 5.1, and it is known that the tidal heating equation is a stiff function of the semi-major axis, as seen in Equation (4.2). But, since the core heating models predicts the correct radii for `Kepler-7 b`, then the exoplanet might have a core mass between 0 - 10 $M_\oplus$[1].

For most cases, the core heating models predict higher radii than those seen for exoplanets. This might be due to the fact that the heating values for both models were guessed by eye, and not calculated numerically. The cases where the numbers fit are; `WASP-17b`, `Kepler-7 b`, `HAT-P-33 b` and within 3σ confidence; `WASP-63b` and `WASP-31b`.

I predicted the core-heating models would predict the radii worse the further away

[1]Models of Burrows et al. (1997) assume 0 $M_\oplus$ core, while Miller et al. (2009) assume a core of 10 $M_\oplus$

the data points moved from the dashed-line in Figure 5.1. But, it was not predicted that the core heating would predict wrong radii of planets like `Kepler-12 b`. I determined the core heating to be 3×10^{27} erg s^{-1}, but if the heating was to be lower, then the predicted radii would be lower. So, if I assume it to be a factor three smaller, then the radii becomes 1.7$R_{\rm Jup}$ by Equation (5.1), which is close to the radii seen in table 4.6. But, now I begin to play with the data, and it can be seen from Figure 4.5 that the heating is definitely not 10^{27} erg s^{-1}.

It seems that the newer tidal heating models hit the radii far from the observed radii, and only for the larger mass exoplanets, `HAT-P-40 b` and `WASP-54 b` does it fit within the uncertainties. But the ratio in table 4.1 is on the order of 10^{-3}, as in the case of `Kepler-7 b`.

The general trend in Figure 5.1 is that the core heating is larger than what is observed, and increasing the core mass would require a larger core heating, as discussed by Fortney et al. (2011b). The tidal heating models (yellow and cyan) are able to reproduce most of the exoplanets if the tidal dissipation parameter, Q_p, is adjusted correctly for each exoplanet. For the most massive exoplanet, the value should lie between 10^6 and 10^5, while within 10^6 to 10^4 for lower mass exoplanets (behind the dashed line of 0.5 $M_{\rm Jup}$).

The following table shows the ratio of core heating-to-insolation.

WASP		HAT		Kepler		OGLE-TR	
Exoplanet	$\frac{\dot{E}_{core}}{\dot{E}_{inso}}$	Exoplanet	$\frac{\dot{E}_{core}}{\dot{E}_{inso}}$	Exoplanet	$\frac{\dot{E}_{core}}{\dot{E}_{inso}}$	Exoplanet	$\frac{\dot{E}_{core}}{\dot{E}_{inso}}$
`WASP-17 b`	9.531e-03	`HAT-P-32 b`	1.819e-01	`Kepler-12 b`	6.225e-03	`OGLE-TR-10 b`	1.162e-02
`WASP-31 b`	2.143e-03	`HAT-P-33 b`	3.793e-02	`Kepler-7 b`	1.571e-03		
`WASP-39 b`	1.140e-04	`HAT-P-40 b`	9.854e-03	`Kepler-30 d`	...		
`WASP-54 b`	1.601e-02						
`WASP-63 b`	1.005e-03						

Table 5.1: The results above are the calculated heating from the core heating model of Burrows et al. (1997) used in section 4.1.1, figure 4.5. $\dot{E}_{inso} = \pi R_p^2 F_{inc}$

The table above shows the amount of heating needed, which is strong for most cases[1]. The table above indicates that almost all cases require a strong core heating.

[1]I define strong according to Liu et al. (2008), which mentions that strong heating is a value near 10^{-3} erg s^{-1}.

The final remark to Figure 5.1 is that it seems like a higher tidal-dissipation parameter aids the newer model of Jackson et al. (2008a); Miller et al. (2009), and Beaugé and Nesvorný (2012) estimate the tidal parameter, Q_p, should be within; $10^6 - 10^7$. According to Figure 5.1, the value of 10^6 fits better[1] than lower values, which indicates weaker tidal heating. A larger tidal dissipation parameter would as well increase the tidal circularization, as seen in Equation (4.1).

It should also be noted that the disposal of tidal heating has not been discussed, and could make a difference, but most authors assume it to be within the core (Ibgui and Burrows, 2009), as I do in this thesis (to compare it with the core heating).

5.2 A lower flux limit on inflation

I have described three different mechanisms for inflating exoplanets in section 4.1, and in the following subsections of the low-density sample, section 4.2, I noticed that all exoplanets are heavily irradiated due to their proximity to the star. The close distance increases the incident flux on the exoplanet[2], so several authors have investigated the inflated exoplanets with the incident flux (Demory and Seager, 2011; Fortney et al., 2011b; Spiegel and Burrows, 2013).

It seems as the physical mechanism of inflating an exoplanet initiates around 2×10^8erg s^{-1} cm^{-2}, as can be seen on Figure 5.2. The figure depicts a sample of candidates and confirmed exoplanets, where the first mentioned are gray and black, while the confirmed exoplanets are colored by red. The gray diamonds illustrate ambiguous candidates.

[1]This is simply by saying that according to the newer tidal dissipation models, $Q_p = 10^4$ and 10^5 fit 0 exoplanets, while $Q_p = 10^6$ fits 2 exoplanets

[2]$F_p \propto \frac{L}{a^2}$

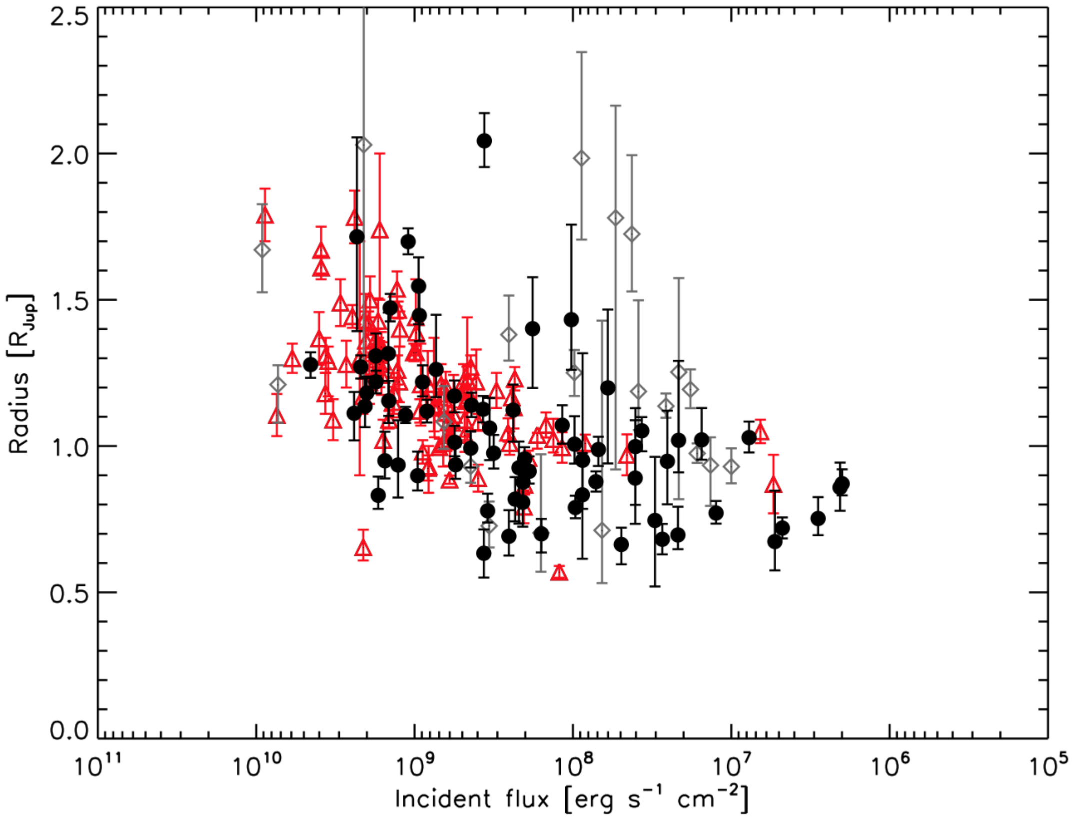

Figure 5.2: The figure depicts exoplanets' radii as a function of incident flux. The sample is composed of two types of candidates and confirmed exoplanets, black, gray and red, respectively. A tendency shows that at larger incident fluxes than 2×10^8erg s^{-1} cm^{-2} inflation occurs. Figure is taken from Demory and Seager (2011).

The trend seems pretty confident as a steepening occurs after $\sim 2 \cdot 10^8$ erg s^{-1} cm^{-2}. The authors took a sample of exoplanets and candidates between 8 and 22 $R_{\oplus}$, and find around 115 giant exoplanets within the first two quarters of the Kepler data (Q0 - Q2).

But as seen for the case of `KOI-102` in section 3.2.1, updated results may indicate additional data, as a companion candidate. Updated results from the Kepler Input Catalogue increase the dataset to 174 candidates, and if these are taken into account then the trend is removed, and a scatter appears.

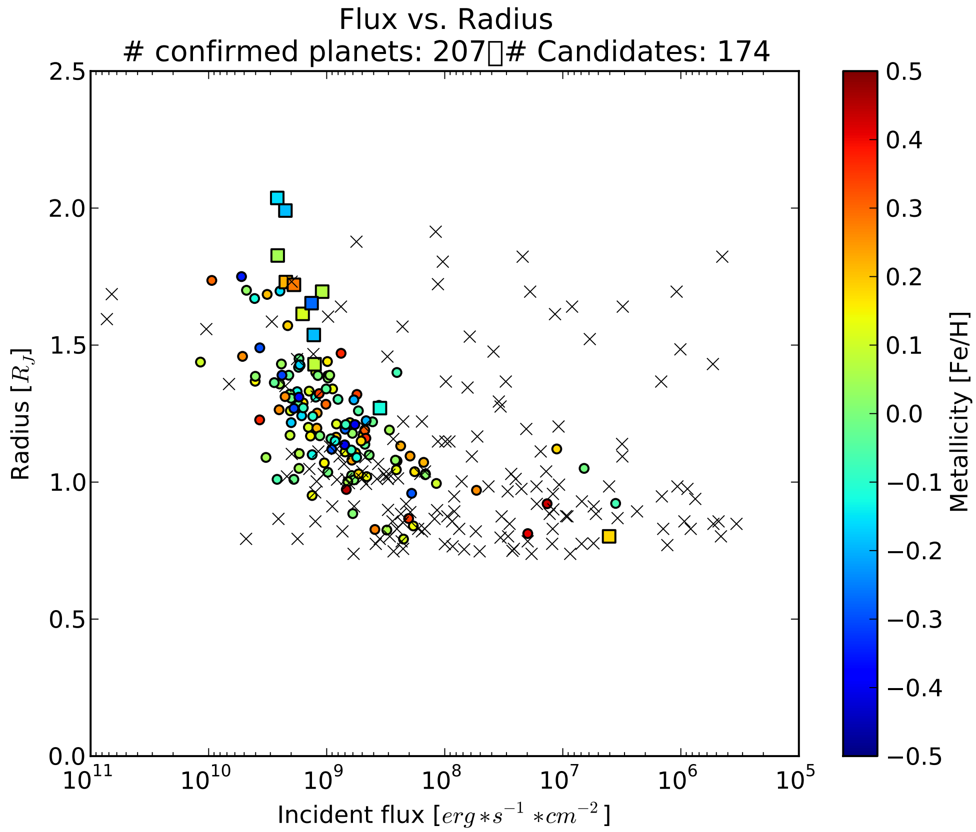

Figure 5.3: Same figure as Figure 5.2, but with newer data from the Kepler mission, which shows a scatter instead of the earlier observed tendency. The crosses are the candidates, while the colored dots are the confirmed exoplanets with their respective metallicity. The larger squares are exoplanets within our low-density sample.

The updated figure depicts that one should be careful with the flux limit found in Figure 5.2, since a larger scatter appears due to around 20 new candidates. The 20 new candidates correspond to 11% of the total amount of candidates in the sample (8R$_\oplus$- 22 R$_\oplus$).

One might say that these candidates are within the 14% false-positive determined by Demory and Seager (2011). If, one states that the 20 candidates seen in Figure 5.3 are all false-positives, then the tendency from earlier is true. The values in Figure 5.2 have been double checked by observing secondary eclipses to avoid blending scenarios as described in section 3.3.2. These results are more confident than those from our database, which are taken directly from the Kepler Input Catalogue and without any double-checked detection. A double check is necessary since the stellar radii uncertainty of the Kepler Catalogue of Interest is 35% (Demory and Seager, 2011, cf. *Brown et al., 2011*), which changes the luminosity, thus the incident flux, and the radius of the candidate due to the linear-relation, described in section 2.1.

If the relation, between the incident flux and radii, disappears after a follow-up observation of the candidates, then it means that the stellar irradiation has a lesser effect on the inflation, and other processes such as double-diffusive convection might be necessary (Demory and Seager, 2011).

The conclusion is that the flux-limit could be up for debate, but one should not determine a conclusion based on raw-data from the candidate-database, which has not been checked for blending scenarios.

Another interesting feature of Figure 5.3 is that the metallicity seems quite scattered, and this is against the remarks of Demory and Seager (2011), who mention that exoplanets enriched with heavy elements would be smaller, due to a more compact structure. This tendency is not seen in the figure, which could indicate that the metallicity might not be a strong source for determining the inflation. This feature was as well seen in our low-density sample, in Figure A.2.

5.3 Thoughts on the mechanisms

The stellar irradiation model assumes a modest radiation even though all of the most inflated exoplanets in our sample have a stellar luminosity above 2 $L_\odot$. A higher luminosity would probably lift the models used by Fortney et al. (2007), since they would inflict the exoplanets with a stronger heating.

In section 4.1, I mention that a low mass exoplanet at 0.045 AU has a radius of $1.9R_{\mathrm{Jup}}$ at 10 Myr after formation (Fortney et al., 2007, cf. Fig. 5). The radius is among the largest seen in the low-density sample, i.e. `WASP-17 b`, and it requires a mechanism that stalls the radius contraction completely for at least 1.6 Gyr (for `WASP-17 b`). Tidal circularization would last approx. 40 Myr at $Q_p = 10^{6.55}$ for `Wasp-17 b`. So, other mechanisms have to stall the contraction, like the enhanced opacity of the atmosphere, ohmic heating or other. In the following section, I will briefly express my thoughts on each mechanism described in section 4.1.

5.3.1 Enhanced atmosphere

The thickened opacity has shown to be in good combination with tidal heating to explain exoplanets such as HD 209458 b (Ibgui and Burrows, 2009). A sign of thicker opacities is assumed by TiO and VO-lines in the spectra, which can lead to temperature inversions. The temperature inversion ensures that the upper layers of the atmosphere are hotter than the inner layers until a pressure of around 0.1-1 bar. This shift in temperature may act as a layer with increased opacity, thus stalling the outgoing radiation (Spiegel and Burrows, 2012). The presence of temperature inversions in the atmosphere of some exoplanets, but not in others, has been shown to be an effect of atmospheric opacity (Burrows, 2013a; Perna et al., 2012). Knutson et al. (2010) proposes that the source of temperature inversions might not be due to TiO and VO, but an increased UV flux from the stellar host. Therefore proposing these temperature inversions to exists primarily for planets near active stars, since some planets have TiO in the atmosphere, but no sign of temperature inversions.

A recent publication by Demory et al. (2013) has found evidence of optically thick clouds in Kepler-7 b. This has been done by calculating the albedo of the exoplanet, which indicates a presence of a cloud or haze layer in its atmosphere. These clouds could perhaps be formed due to silicate condensation due to the incident flux, and with the low surface gravity, cloud sedimentation is suppressed (Demory et al., 2013).

5.3.2 Tidal heating

A question might be raised of where the tidal heating affects the exoplanet? As the exoplanet orbits the star, the tidal force heats up the whole exoplanet, but where is the energy deployed? It has been noted that this factor is still unknown, and if the energy is deployed in the atmosphere then tidal heating cannot be responsible for inflation (Batygin et al., 2011). But, all the models used in the section of tidal heating, §4.1.2, assume the energy to be deposited in the core of the exoplanet (Ibgui and Burrows, 2009; Miller et al., 2009).

The uncertainty in tidal theory is of such magnitude that no approach can be considered correct (Anderson et al., 2011b). The applied models are only indicative with the uncertain tidal dissipation parameter, which seems to have an order of uncertainty, ranging between 10^6 and 10^7 (Beaugé and Nesvorný, 2012; Ibgui and Burrows, 2009). The results obtained in Figure 5.1 indicate that planets more massive than 0.5 M_{Jup} have tidal dissipation in between 10^5 to 10^6, which is one order lower than proposed by the authors. Lower mass planets require a larger spread in the tidal dissipation parameter; $10^4 - 10^6$. The range of the tidal dissipation parameter has also been noticed by Leconte et al. (2010), which point out that these large uncertainties lead to a large variety in timescales of circularization.

5.3.3 Ohmic heating

Many parameters in the model are unknown; such as the internal structure, magnetic field strength and atmospheric composition (Burrows, 2013b; Faedi et al., 2013). A high temperature around 1800 K almost always ended in evaporation, so it has been noted that the efficiency, ϵ, might be lower at these temperatures (Faedi et al., 2013, cf. *Huang & Cumming et al. (2012)*). But, it has also been noted that ohmic heating cannot inflate exoplanets at $< 1700 - 1800$K if the magnetic field is similar to that of Jupiter (Perna et al., 2012).

Several exoplanets would be in the process of evaporation for the high equilibrium temperatures calculated, but one should remember that the effective and equilibrium temperature are not similar (Spiegel and Burrows, 2013).

Thermal inversions might complicate ohmic heating, since they are able to reduce the depth at which energy is deployed. If no thermal inversion is present then the energy deployment might go to several tens of bars (Perna et al., 2012)

5.3.4 Does the problem lie in our assumptions?

There are numerous of models, which are based on different initial conditions for the equation of states (EOS) in the interior of planets. But, the models evolve into similar equilibrium parameters (Baraffe et al., 2008; Fortney and Nettelmann, 2010). Same behavior is seen in brown dwarfs, which are more massive than Jupiter, their radii only increases 0.25% by an increase of 0.03 in Helium abundance (Y) (Burrows et al., 2011; Ibgui and Burrows, 2009). The atmosphere structure and cooling properties of brown dwarfs is hard to distinguish from massive exoplanets, due to their similar convective interior with a mixture of metallic Hydrogen and Helium (H/He) (Baraffe et al., 2003)

It should be noted that the field of investigating the EOS of H/He-compositions is strongly under development due to the technological advancement (*Conference talk, Fortney and Baraffe (2013)*). Militzer and Hubbard (2013) revises the mass-radius relationship, which lifts the models, in Figure 4.4 and 1.3, by several 0.1 R_{Jup}. The differences are due to the behavior of the EOS at high pressures.

A thought that might occur is if exoplanets that form in different ways have different outcome. The two main formation theories of planets are; Core accretion and Disk Instability. These vary primarily on the timescale of formation, where the first mentioned takes in order of Gyr, while disk instability is 2-3 orders shorter. It is expected that exoplanets formed under disk instability would have higher entropies, thus larger radii, also referred to as the "hot-start". The core accretion would then be referred to as the "cold-start". One might then expect that the sample of low density exoplanets might be a relic of rare incidents of formation by disk instability, but even such a formation would cool down fast enough within 100 Myr, thereby merging with the predicted radii of core accretion (Spiegel and Burrows, 2012, cf. Fig. 5). The different starts would only be apparent in newborn exoplanets in young stellar objects, and not in inflated exoplanet due to the older age, unless some inflation mechanism is ongoing, i.e. Ohmic heating.

High precision infrared observations by direct imaging would be required to investigate exoplanet formation in young stellar objects in greater detail to find additional evidence for one of these formation theories.

5.4 Discussion of the data analysis

In the case of `KOI-102`, I investigated the case if the only exoplanet was `K00102.01`, because it was larger. If I use Equation (2.3), I could investigate what semi-amplitudes I would predict from the system based on an assumption of the planet and solar mass. If I assume a similarity between `KOI-102` and our solar system, then `K00102.01` and `K00102.02` will have a mass of 17 $M_\oplus$ and 1 $M_\oplus$, respectively. This assumption should be good enough, since the stellar system, `KOI-102` is alike the Sun, but just at close-in orbits. The result is a semi-amplitude of 9.06 m s^{-1} and 0.53 m s^{-1} for the exoplanets. The larger amplitude would therefore be the dominant one in our radial-velocity measurements, while the smaller value would be under our limit for detection, as described in section 2.2.

These calculations are roughly based on the assumption that the exoplanets are alike the ones of our solar system, but this is unlikely due to the vast diversity of exoplanets, as seen in Figure 4.1. It is also seen that I receive a mass of 0.12 M_{Jup}, which corresponds to 40 $M_\oplus$. The mass is two times larger than that which I predicted if the system was alike our solar system.

It could be interesting to investigate if planets found at close-in orbits but at similar radii to those in our solar system are generally larger. This could point towards interesting features of migration or formation of planets in-situ.

In section 3.2.2, I discussed whether `KOI-94 d` is the dominant source of providing a radial velocity. I can calculate the semi-amplitude by the use of the exoplanet masses by Weiss et al. (2013). The calculations conclude that my assumption of `KOI-94d` not being the dominant source of my semi-amplitude is wrong, since its semi-amplitude is four times larger than the second largest amplitude of `KOI-94 e` at 5 m s^{-1}. This means that the three other companions would get lost within my uncertainty of the semi-amplitude, which was 9 m s^{-1}, and my fit would actually be able to guess the semi-amplitude of the exoplanet, `KOI-94d`, and thus the mass of the planet.

In section 3.5, I discussed that the exoplanets are not inflated according to the standard cooling models for irradiated planets, as seen by the blue-lines in Figure 4.1. The incident flux of the exoplanets are; 2×10^9 erg s^{-1} cm^{-2} and 1.48×10^8 erg s^{-1} cm^{-2} for `K00102.01` and `KOI-94 d`, respectively[1]. The first mentioned planet should be irradiated, but a look at Figure 1.3 tells us that it can be explained by models of Fortney et al. (2007), since its radii is below 13 $R_\oplus$(The radii of `K00102.01` is 3.63 $R_\oplus$). But the result also fits Figure A.3, and it points towards no relation between inflation and incident flux for Neptune-sized exoplanets. `KOI-94 d` does not surpass the flux-limit of $2\times\ 10^8$ erg s^{-1} $cm^{-2}$and is as well not inflated, which fits with the general view of inflated exoplanets (Demory and Seager, 2011).

5.5 Future prospects

Many of the heating models described in this thesis need to be thoroughly revised, because not all exoplanets are explained by them and they are made of unconstrained assumptions. The new observation of clouds on `Kepler-7 b` by Demory et al. (2013) ignites the study of gaseous planets. The enhanced atmosphere could be a viable solution but only in combination with other mechanisms for the largest exoplanets. The work of Ohmic heating is probable for most cases, and is as well indicated by Figure 5.2 to be a factor - because a lower limit incident flux is observed.

An interesting trend for the future would be to observe whether Neptunelike exoplanets have radii above the models of Baraffe et al. (2008); Fortney et al. (2007). I have tried to estimate the mass of candidate planets by looking at the sample of confirmed planets, and the result is shown in Figure A.7. The figure depicts how the upcoming confirmation of candidates might change Figure 1.3. I have given four mass-sample limits of planets with four different radii, which can be seen in

[1]Inserted values for `K00102.01`: 1.2 $L_\odot$, 0.02 AU, and for `KOI-94 d`: 3.0 $L_\odot$, 0.168 AU.

the program, which is described in Appendix B[1]. The figure depicts that not many planets are proposed to be inflated in the regime of the low-density sample, and the reason could be that *Kepler* has not detected many hot-Jupiters, but rather multiple Neptune-sized planets, see Figure 1.2. Inflated planets at Neptune-sizes, if the mass of Neptune is assumed, would be interesting to observe, since these should only exist in a short period due to Evaporation (Owen and Wu, 2013). The evaporation process would be quite short due to the amount of gas available for evaporation. If evaporation is the cause of inflated Neptunelike planets, then a relation between incident flux and radii should not be apparent as for larger mass exoplanets, but a large amount of core-sized planets are proposed to lie in the high incident flux area.

At last, I want to underline the importance of collaboration between astronomers. Numerous of articles used different values of exoplanets compared to the newest values, gathered in this thesis. This is a major problem, because comparison becomes a hard task to preform, since different articles use different values for exoplanets, i.e. (Wu and Lithwick, 2013, cf. Fig. 5) compared to our results of radii. In some cases it is due to the fact that I do not assume all orbits to be circular in my plots.

I hope that astronomers will start collaborating more intensively and ensure that their data-set is the most updated. This is the reason that I used a dynamic database, as that of Open Exoplanet Catalogue, which updates frequently. It is important to achieve consistent data in specified areas of exoplanets.

At last, I just wanted to show the reader that even a constant update of all the plots in this thesis cannot follow the hast of exoplanet confirmation and detection. Around 50 new planets have been published during the last weeks of my thesis, and 4 more low-density exoplanets are added, incl. two giants, `WASP-90` and `WASP-76` (West et al., 2013).

[1]The estimated mass of candidates is seen in the program, oec_plot.py; Candidate; add_mass(). I have estimated the mass of candidates based on the radii-regime seen in the confirmed exoplanets. I have as well added a random factor to create a spread seen for masses in similar radii

List of Figures

List of Tables

References

D. R. Anderson, C. Hellier, M. Gillon, A. H. M. J. Triaud, B. Smalley, L. Hebb, A. Collier Cameron, P. F. L. Maxted, D. Queloz, R. G. West, S. J. Bentley, B. Enoch, K. Horne, T. A. Lister, M. Mayor, N. R. Parley, F. Pepe, D. Pollacco, D. Ségransan, S. Udry, and D. M. Wilson. Wasp-17b: An Ultra-Low Density Planet in a Probable Retrograde Orbit. *apj*, 709:159–167, January 2010. doi: 10.1088/0004-637X/709/1/159.

D. R. Anderson, A. Collier Cameron, C. Hellier, M. Lendl, T. A. Lister, P. F. L. Maxted, D. Queloz, B. Smalley, A. M. S. Smith, A. H. M. J. Triaud, R. G. West, D. J. A. Brown, M. Gillon, F. Pepe, D. Pollacco, D. Ségransan, R. A. Street, and S. Udry. WASP-31b: a low-density planet transiting a metal-poor, late-F-type dwarf star. *aap*, 531:A60, July 2011a. doi: 10.1051/0004-6361/201016208.

D. R. Anderson, A. M. S. Smith, A. A. Lanotte, T. S. Barman, A. Collier Cameron, C. J. Campo, M. Gillon, J. Harrington, C. Hellier, P. F. L. Maxted, D. Queloz, A. H. M. J. Triaud, and P. J. Wheatley. Thermal emission at 4.5 and 8 μm of WASP-17b, an extremely large planet in a slightly eccentric orbit. *mnras*, 416:2108–2122, September 2011b. doi: 10.1111/j.1365-2966.2011.19182.x.

I. Baraffe, G. Chabrier, T. S. Barman, F. Allard, and P. H. Hauschildt. Evolutionary models for cool brown dwarfs and extrasolar giant planets. The case of HD 209458. *aap*, 402:701–712, May 2003. doi: 10.1051/0004-6361:20030252.

I. Baraffe, G. Chabrier, and T. Barman. Structure and evolution of super-Earth to super-Jupiter exoplanets. I. Heavy element enrichment in the interior. *aap*, 482:315–332, April 2008. doi: 10.1051/0004-6361:20079321.

K. Batygin, D. J. Stevenson, and P. H. Bodenheimer. Evolution of Ohmically Heated Hot Jupiters. *apj*, 738:1, September 2011. doi: 10.1088/0004-637X/738/1/1.

C. Beaugé and D. Nesvorný. Multiple-planet Scattering and the Origin of Hot Jupiters. *apj*, 751:119, June 2012. doi: 10.1088/0004-637X/751/2/119.

C. Beaugé and D. Nesvorný. Emerging Trends in a Period-Radius Distribution of Close-in Planets. *apj*, 763:12, January 2013. doi: 10.1088/0004-637X/763/1/12.

Y. Bhattacharjee and D. Clery. A Gallery of Planet Hunters. *Science*, 340:566–569, May 2013.

W. J. Borucki, D. Koch, G. Basri, N. Batalha, T. Brown, D. Caldwell, J. Caldwell, J. Christensen-Dalsgaard, W. D. Cochran, E. DeVore, E. W. Dunham, A. K. Dupree, T. N. Gautier, J. C. Geary, R. Gilliland, A. Gould, S. B. Howell, J. M. Jenkins, Y. Kondo, D. W. Latham, G. W. Marcy, S. Meibom, H. Kjeldsen, J. J. Lissauer, D. G. Monet, D. Morrison, D. Sasselov, J. Tarter, A. Boss, D. Brownlee, T. Owen, D. Buzasi, D. Charbonneau, L. Doyle, J. Fortney, E. B. Ford, M. J. Holman, S. Seager, J. H. Steffen, W. F. Welsh, J. Rowe, H. Anderson, L. Buchhave, D. Ciardi, L. Walkowicz, W. Sherry, E. Horch, H. Isaacson, M. E. Everett, D. Fischer, G. Torres, J. A. Johnson, M. Endl, P. MacQueen, S. T. Bryson, J. Dotson, M. Haas, J. Kolodziejczak, J. Van Cleve, H. Chandrasekaran, J. D. Twicken, E. V. Quintana, B. D. Clarke, C. Allen, J. Li, H. Wu, P. Tenenbaum, E. Verner, F. Bruhweiler, J. Barnes, and A. Prsa. Kepler Planet-Detection Mission: Introduction and First Results. *Science*, 327:977–, February 2010. doi: 10.1126/science.1185402.

L. A. Buchhave, D. W. Latham, J. A. Carter, J.-M. Désert, G. Torres, E. R. Adams, S. T. Bryson, D. B. Charbonneau, D. R. Ciardi, C. Kulesa, A. K. Dupree, D. A. Fischer, F. Fressin, T. N. Gautier, III, R. L. Gilliland, S. B. Howell, H. Isaacson, J. M. Jenkins, G. W. Marcy, D. W. McCarthy, J. F. Rowe, N. M. Batalha, W. J. Borucki, T. M. Brown, D. A. Caldwell, J. L. Christiansen, W. D. Cochran, D. Deming, E. W. Dunham, M. Everett, E. B. Ford, J. J. Fortney, J. C. Geary, F. R. Girouard, M. R. Haas, M. J. Holman, E. Horch, T. C. Klaus, H. A. Knutson, D. G. Koch, J. Kolodziejczak, J. J. Lissauer, P. Machalek, F. Mullally, M. D. Still, S. N. Quinn, S. Seager, S. E. Thompson, and J. Van Cleve. Kepler-14b: A Massive Hot Jupiter Transiting an F Star in a Close Visual Binary. *apjs*, 197:3, November 2011. doi: 10.1088/0067-0049/197/1/3.

A. Burrows. Spectra as windows into exoplanets atmospheres. 2013a.

A. Burrows. *personal communication*, July 2013b.

A. Burrows, M. Marley, W. B. Hubbard, J. I. Lunine, T. Guillot, D. Saumon, R. Freedman, D. Sudarsky, and C. Sharp. A Nongray Theory of Extrasolar Giant Planets and Brown Dwarfs. *apj*, 491:856, December 1997. doi: 10.1086/305002.

A. Burrows, I. Hubeny, J. Budaj, and W. B. Hubbard. Possible Solutions to the Radius Anomalies of Transiting Giant Planets. *apj*, 661:502–514, May 2007. doi: 10.1086/514326.

A. Burrows, K. Heng, and T. Nampaisarn. The Dependence of Brown Dwarf Radii on Atmospheric Metallicity and Clouds: Theory and Comparison with Observations. *apj*, 736:47, July 2011. doi: 10.1088/0004-637X/736/1/47.

D. Buzasi. Stellar Magnetic Fields as a Heating Source for Extrasolar Giant Planets. *apjl*, 765:L25, March 2013. doi: 10.1088/2041-8205/765/2/L25.

B. Campbell, G. A. H. Walker, and S. Yang. A search for substellar companions to solar-type stars. *apj*, 331:902–921, August 1988. doi: 10.1086/166608.

W. D. Cochran, D. C. Fabrycky, G. Torres, F. Fressin, J.-M. Désert, D. Ragozzine, D. Sasselov, J. J. Fortney, J. F. Rowe, E. J. Brugamyer, S. T. Bryson, J. A. Carter, D. R. Ciardi, S. B. Howell, J. H. Steffen, W. J. Borucki, D. G. Koch, J. N. Winn, W. F. Welsh, K. Uddin, P. Tenenbaum, M. Still, S. Seager, S. N. Quinn, F. Mullally, N. Miller, G. W. Marcy, P. J. MacQueen, P. Lucas, J. J. Lissauer, D. W. Latham, H. Knutson, K. Kinemuchi, J. A. Johnson, J. M. Jenkins, H. Isaacson, A. Howard, E. Horch, M. J. Holman, C. E. Henze, M. R. Haas, R. L. Gilliland, T. N. Gautier, III, E. B. Ford, D. A. Fischer, M. Everett, M. Endl, B.-O. Demory, D. Deming, D. Charbonneau, D. Caldwell, L. Buchhave, T. M. Brown, and N. Batalha. Kepler-18b, c, and d: A System of Three Planets Confirmed by Transit Timing Variations, Light Curve Validation, Warm-Spitzer Photometry, and Radial Velocity Measurements. *apjs*, 197:7, November 2011. doi: 10.1088/0067-0049/197/1/7.

R. M. Cutri, M. F. Skrutskie, S. van Dyk, C. A. Beichman, J. M. Carpenter, T. Chester, L. Cambresy, T. Evans, J. Fowler, J. Gizis, E. Howard, J. Huchra, T. Jarrett, E. L. Kopan, J. D. Kirkpatrick, R. M. Light, K. A. Marsh, H. McCallon, S. Schneider, R. Stiening, M. Sykes, M. Weinberg, W. A. Wheaton, S. Wheelock, and N. Zacarias. 2MASS All-Sky Catalog of Point Sources (Cutri+ 2003). *VizieR Online Data Catalog*, 2246:0, March 2003.

B.-O. Demory and S. Seager. Lack of Inflated Radii for Kepler Giant Planet Candidates Receiving Modest Stellar Irradiation. *apjs*, 197:12, November 2011. doi: 10.1088/0067-0049/197/1/12.

B.-O. Demory, S. Seager, N. Madhusudhan, H. Kjeldsen, J. Christensen-Dalsgaard, M. Gillon, J. F. Rowe, W. F. Welsh, E. R. Adams, A. Dupree, D. McCarthy, C. Kulesa, W. J. Borucki, and D. G. Koch. The High Albedo of the Hot Jupiter Kepler-7 b. *apjl*, 735:L12, July 2011. doi: 10.1088/2041-8205/735/1/L12.

B.-O. Demory, J. de Wit, N. Lewis, J. Fortney, A. Zsom, S. Seager, H. Knutson, K. Heng, N. Madhusudhan, M. Gillon, T. Barclay, J.-M. Desert, V. Parmentier, and N. B. Cowan. Inference of Inhomogeneous Clouds in an Exoplanet Atmosphere. *ArXiv e-prints*, September 2013.

A. P. Doyle, B. Smalley, P. F. L. Maxted, D. R. Anderson, A. C. Cameron, M. Gillon, C. Hellier, D. Pollacco, D. Queloz, A. H. M. J. Triaud, and R. G. West. Accurate spectroscopic parameters of WASP planet host stars. *mnras*, 428:3164–3172, February 2013. doi: 10.1093/mnras/sts267.

D. Ehrenreich and J.-M. Désert. Mass-loss rates for transiting exoplanets. *aap*, 529:A136, May 2011. doi: 10.1051/0004-6361/201016356.

B. Enoch, A. Collier Cameron, and K. Horne. Factors affecting the radii of close-in transiting exoplanets. *aap*, 540:A99, April 2012. doi: 10.1051/0004-6361/201117317.

F. Faedi, S. C. C. Barros, D. R. Anderson, D. J. A. Brown, A. Collier Cameron, D. Pollacco, I. Boisse, G. Hébrard, M. Lendl, T. A. Lister, B. Smalley, R. A. Street, A. H. M. J. Triaud, J. Bento, F. Bouchy, O. W. Butters, B. Enoch, C. A. Haswell, C. Hellier, F. P. Keenan, G. R. M. Miller, V. Moulds, C. Moutou, A. J. Norton, D. Queloz, A. Santerne, E. K. Simpson, I. Skillen, A. M. S. Smith, S. Udry, C. A. Watson, R. G. West, and P. J. Wheatley. WASP-39b: a highly inflated Saturn-mass planet orbiting a late G-type star. *aap*, 531:A40, July 2011. doi: 10.1051/0004-6361/201116671.

F. Faedi, D. Pollacco, S. C. C. Barros, D. Brown, A. Collier Cameron, A. P. Doyle, R. Enoch, M. Gillon, Y. Gómez Maqueo Chew, G. Hébrard, M. Lendl, C. Liebig, B. Smalley, A. H. M. J. Triaud, R. G. West, P. J. Wheatley, K. A. Alsubai, D. R. Anderson, D. Armstrong, J. Bento, J. Bochinski, F. Bouchy, R. Busuttil, L. Fossati, A. Fumel, C. A. Haswell, C. Hellier, S. Holmes, E. Jehin, U. Kolb, J. McCormac, G. R. M. Miller, C. Moutou, A. J. Norton, N. Parley, D. Queloz, A. Santerne, I. Skillen, A. M. S. Smith, S. Udry, and C. Watson. WASP-54b, WASP-56b, and WASP-57b: Three new sub-Jupiter mass planets from SuperWASP. *aap*, 551:A73, March 2013. doi: 10.1051/0004-6361/201220520.

D. Foreman-Mackey, D. W. Hogg, D. Lang, and J. Goodman. emcee: The MCMC Hammer. *pasp*, 125:306–312, March 2013. doi: 10.1086/670067.

J. Fortney and I. Baraffe. Planetary internal structures. Protostars and Planets VI, July 2013. URL http://youtu.be/eMBGae7mXjQ.

J. J. Fortney and N. Nettelmann. The Interior Structure, Composition, and Evolution of Giant Planets. *ssr*, 152:423–447, May 2010. doi: 10.1007/s11214-009-9582-x.

J. J. Fortney, M. S. Marley, and J. W. Barnes. Planetary Radii across Five Orders of Magnitude in Mass and Stellar Insolation: Application to Transits. *apj*, 659:1661–1672, April 2007. doi: 10.1086/512120.

J. J. Fortney, I. Baraffe, and B. Militzer. *Giant Planet Interior Structure and Thermal Evolution*, pages 397–418. 2011a.

J. J. Fortney, B.-O. Demory, J.-M. Désert, J. Rowe, G. W. Marcy, H. Isaacson, L. A. Buchhave, D. Ciardi, T. N. Gautier, N. M. Batalha, D. A. Caldwell, S. T. Bryson, P. Nutzman, J. M. Jenkins, A. Howard, D. Charbonneau, H. A. Knutson, S. B. Howell, M. Everett, F. Fressin, D. Deming, W. J. Borucki, T. M. Brown, E. B. Ford, R. L. Gilliland, D. W. Latham, N. Miller, S. Seager, D. A. Fischer, D. Koch, J. J. Lissauer, M. R. Haas, M. Still, P. Lucas, M. Gillon, J. L. Christiansen, and J. C. Geary. Discovery and Atmospheric Characterization of Giant Planet Kepler-12b: An Inflated Radius Outlier. *apjs*, 197:9, November 2011b. doi: 10.1088/0067-0049/197/1/9.

R. Galicher, C. Marois, B. Zuckerman, and B. Macintosh. Fomalhaut b: Independent Analysis of the Hubble Space Telescope Public Archive Data. *ArXiv e-prints*, October 2012.

B. S. Gaudi and J. N. Winn. Prospects for the Characterization and Confirmation of Transiting Exoplanets via the Rossiter-McLaughlin Effect. *apj*, 655:550–563, January 2007. doi: 10.1086/509910.

J. D. Hartman, G. Á. Bakos, G. Torres, D. W. Latham, G. Kovács, B. Béky, S. N. Quinn, T. Mazeh, A. Shporer, G. W. Marcy, A. W. Howard, D. A. Fischer, J. A. Johnson, G. A. Esquerdo, R. W. Noyes, D. D. Sasselov, R. P. Stefanik, J. M. Fernandez, T. Szklenár, J. Lázár, I. Papp, and P. Sári. HAT-P-32b and HAT-P-33b: Two Highly Inflated Hot Jupiters Transiting High-jitter Stars. *apj*, 742:59, November 2011. doi: 10.1088/0004-637X/742/1/59.

J. D. Hartman, G. Á. Bakos, B. Béky, G. Torres, D. W. Latham, Z. Csubry, K. Penev, A. Shporer, B. J. Fulton, L. A. Buchhave, J. A. Johnson, A. W. Howard, G. W. Marcy, D. A. Fischer, G. Kovács, R. W. Noyes, G. A. Esquerdo, M. Everett, T. Szklenár, S. N. Quinn, A. Bieryla, R. P. Knox, P. Hinz, D. D. Sasselov, G. Fűrész, R. P. Stefanik, J. Lázár, I. Papp, and P. Sári. HAT-P-39b-HAT-P-41b: Three Highly Inflated Transiting Hot Jupiters. *aj*, 144:139, November 2012. doi: 10.1088/0004-6256/144/5/139.

C. Hellier, D. R. Anderson, A. Collier Cameron, A. P. Doyle, A. Fumel, M. Gillon, E. Jehin, M. Lendl, P. F. L. Maxted, F. Pepe, D. Pollacco, D. Queloz, D. Ségransan, B. Smalley, A. M. S. Smith, J. Southworth, A. H. M. J. Triaud, S. Udry, and R. G. West. Seven transiting hot Jupiters from WASP-South, Euler and TRAPPIST: WASP-47b, WASP-55b, WASP-61b, WASP-62b, WASP-63b, WASP-66b and WASP-67b. *mnras*, 426:739–750, October 2012. doi: 10.1111/j.1365-2966.2012.21780.x.

A. W. Howard. Observed Properties of Extrasolar Planets. *ArXiv e-prints*, May 2013.

A. W. Howard, G. W. Marcy, S. T. Bryson, J. M. Jenkins, J. F. Rowe, N. M. Batalha, W. J. Borucki, D. G. Koch, E. W. Dunham, T. N. Gautier, III, J. Van Cleve, W. D. Cochran, D. W. Latham, J. J. Lissauer, G. Torres, T. M. Brown, R. L. Gilliland, L. A. Buchhave, D. A. Caldwell, J. Christensen-Dalsgaard, D. Ciardi, F. Fressin, M. R. Haas, S. B. Howell, H. Kjeldsen, S. Seager, L. Rogers, D. D. Sasselov, J. H. Steffen, G. S. Basri, D. Charbonneau, J. Christiansen, B. Clarke, A. Dupree, D. C. Fabrycky, D. A. Fischer, E. B. Ford, J. J. Fortney, J. Tarter, F. R. Girouard, M. J. Holman, J. A. Johnson, T. C. Klaus, P. Machalek, A. V. Moorhead, R. C. Morehead, D. Ragozzine, P. Tenenbaum, J. D. Twicken, S. N. Quinn, H. Isaacson, A. Shporer, P. W. Lucas, L. M. Walkowicz, W. F. Welsh, A. Boss, E. Devore, A. Gould, J. C. Smith, R. L. Morris, A. Prsa, T. D. Morton, M. Still, S. E. Thompson, F. Mullally, M. Endl, and P. J. MacQueen. Planet Occurrence within 0.25 AU of Solar-type Stars from Kepler. *apjs*, 201:15, August 2012. doi: 10.1088/0067-0049/201/2/15.

L. Ibgui and A. Burrows. Coupled Evolution with Tides of the Radius and Orbit of Transiting Giant Planets: General Results. *apj*, 700:1921–1932, August 2009. doi: 10.1088/0004-637X/700/2/1921.

B. Jackson, R. Greenberg, and R. Barnes. Tidal Heating of Extrasolar Planets. *apj*, 681: 1631–1638, July 2008a. doi: 10.1086/587641.

B. Jackson, R. Greenberg, and R. Barnes. Tidal Evolution of Close-in Extrasolar Planets. *apj*, 678:1396–1406, May 2008b. doi: 10.1086/529187.

P. Kalas. Direct imaging of massive extrasolar planets. In A. Sozzetti, M. G. Lattanzi, and A. P. Boss, editors, *IAU Symposium*, volume 276 of *IAU Symposium*, pages 279–286, November 2011. doi: 10.1017/S1743921311020321.

H. A. Knutson, A. W. Howard, and H. Isaacson. A Correlation Between Stellar Activity and Hot Jupiter Emission Spectra. *apj*, 720:1569–1576, September 2010. doi: 10.1088/0004-637X/720/2/1569.

D. W. Latham, W. J. Borucki, D. G. Koch, T. M. Brown, L. A. Buchhave, G. Basri, N. M. Batalha, D. A. Caldwell, W. D. Cochran, E. W. Dunham, G. Fűrész, T. N. Gautier, III, J. C. Geary, R. L. Gilliland, S. B. Howell, J. M. Jenkins, J. J. Lissauer, G. W. Marcy, D. G. Monet, J. F. Rowe, and D. D. Sasselov. Kepler-7b: A Transiting Planet with Unusually Low Density. *apjl*, 713:L140, April 2010. doi: 10.1088/2041-8205/713/2/L140.

G. Laughlin, M. Crismani, and F. C. Adams. On the Anomalous Radii of the Transiting Extrasolar Planets. *apjl*, 729:L7, March 2011. doi: 10.1088/2041-8205/729/1/L7.

J. Leconte, G. Chabrier, I. Baraffe, and B. Levrard. Is tidal heating sufficient to explain bloated exoplanets? Consistent calculations accounting for finite initial eccentricity. *aap*, 516:A64, June 2010. doi: 10.1051/0004-6361/201014337.

X. Liu, A. Burrows, and L. Ibgui. Theoretical Radii of Extrasolar Giant Planets: the Cases of TrES-4, XO-3b, and HAT-P-1b. *apj*, 687:1191–1200, November 2008. doi: 10.1086/592189.

C. Lovis and D. Fischer. *Radial Velocity Techniques for Exoplanets*, pages 27–53. 2011.

R. Martínez-Arnáiz, J. Maldonado, D. Montes, C. Eiroa, and B. Montesinos. Chromospheric activity and rotation of FGK stars in the solar vicinity. An estimation of the radial velocity jitter. *aap*, 520:A79, September 2010. doi: 10.1051/0004-6361/200913725.

M. Mayor and D. Queloz. A Jupiter-mass companion to a solar-type star. *nat*, 378:355–359, November 1995. doi: 10.1038/378355a0.

B. E. McArthur, G. F. Benedict, R. Barnes, E. Martioli, S. Korzennik, E. Nelan, and R. P. Butler. New Observational Constraints on the Andromedae System with Data from the Hubble Space Telescope and Hobby-Eberly Telescope. *apj*, 715:1203–1220, June 2010. doi: 10.1088/0004-637X/715/2/1203.

B. Militzer and W. B. Hubbard. Ab Initio Equation of State for Hydrogen-Helium Mixtures with Recalibration of the Giant-planet Mass-Radius Relation. *apj*, 774:148, September 2013. doi: 10.1088/0004-637X/774/2/148.

N. Miller. *private communication*, July 2013.

N. Miller and J. J. Fortney. The Heavy-element Masses of Extrasolar Giant Planets, Revealed. *apjl*, 736:L29, August 2011. doi: 10.1088/2041-8205/736/2/L29.

N. Miller, J. J. Fortney, and B. Jackson. Inflating and Deflating Hot Jupiters: Coupled Tidal and Thermal Evolution of Known Transiting Planets. *apj*, 702:1413–1427, September 2009. doi: 10.1088/0004-637X/702/2/1413.

C. D. Murray and A. C. M. Correia. *Keplerian Orbits and Dynamics of Exoplanets*, pages 15–23. 2011.

J. E. Owen and Y. Wu. Kepler planets: a tale of evaporation. *ArXiv e-prints*, March 2013.

John C.B. Papaloizou and Caroline Terquem. Planet formation and migration. *Reports on Progress in Physics*, 69(1):119–180, 2006.

R. Perna, K. Heng, and F. Pont. The Effects of Irradiation on Hot Jovian Atmospheres: Heat Redistribution and Energy Dissipation. *apj*, 751:59, May 2012. doi: 10.1088/0004-637X/751/1/59.

Michael. Perryman. Cambridge University Press, 2011. URL http://dx.doi.org/10.1017/CBO9780511994852.006.

F. Pont, C. Moutou, M. Gillon, A. Udalski, F. Bouchy, J. M. Fernandes, W. Gieren, M. Mayor, T. Mazeh, D. Minniti, C. Melo, D. Naef, G. Pietrzynski, D. Queloz, M. T. Ruiz, N. C. Santos, and S. Udry. The ”666” collaboration on OGLE transits. I. Accurate radius of the planets OGLE-TR-10b and OGLE-TR-56b with VLT deconvolution photometry. *aap*, 465:1069–1074, April 2007. doi: 10.1051/0004-6361:20066645.

W. H. Press, B. P. Flannery, and S. A. Teukolsky. *Numerical recipes. The art of scientific computing*. 2007.

H. Rein. A proposal for community driven and decentralized astronomical databases and the Open Exoplanet Catalogue. *ArXiv e-prints*, November 2012.

P. V. Sada, D. Deming, D. E. Jennings, B. K. Jackson, C. M. Hamilton, J. Fraine, S. W. Peterson, F. Haase, K. Bays, A. Lunsford, and E. O'Gorman. Extrasolar Planet Transits Observed at Kitt Peak National Observatory. *pasp*, 124:212–229, March 2012. doi: 10.1086/665043.

R. Sanchis-Ojeda, D. C. Fabrycky, J. N. Winn, T. Barclay, B. D. Clarke, E. B. Ford, J. J. Fortney, J. C. Geary, M. J. Holman, A. W. Howard, J. M. Jenkins, D. Koch, J. J. Lissauer, G. W. Marcy, F. Mullally, D. Ragozzine, S. E. Seader, M. Still, and S. E. Thompson. Alignment of the stellar spin with the orbits of a three-planet system. *nat*, 487:449–453, July 2012. doi: 10.1038/nature11301.

S. Seager, M. Kuchner, C. A. Hier-Majumder, and B. Militzer. Mass-Radius Relationships for Solid Exoplanets. *apj*, 669:1279–1297, November 2007. doi: 10.1086/521346.

J. Southworth. Homogeneous studies of transiting extrasolar planets - III. Additional planets and stellar models. *mnras*, 408:1689–1713, November 2010. doi: 10.1111/j.1365-2966.2010.17231.x.

J. Southworth, T. C. Hinse, M. Dominik, X.-S. Fang, K. Harpsøe, U. G. Jørgensen, E. Kerins, C. Liebig, L. Mancini, J. Skottfelt, D. R. Anderson, B. Smalley, J. Tregloan-Reed, O. Wertz, K. A. Alsubai, V. Bozza, S. Calchi Novati, S. Dreizler, S.-H. Gu, M. Hundertmark, J. Jessen-Hansen, N. Kains, H. Kjeldsen, M. N. Lund, M. Lundkvist, M. Mathiasen, M. T. Penny, S. Rahvar, D. Ricci, G. Scarpetta, C. Snodgrass, and J. Surdej. High-precision photometry by telescope defocusing - IV. Confirmation of the huge radius of WASP-17 b. *mnras*, 426:1338–1348, October 2012. doi: 10.1111/j.1365-2966.2012.21781.x.

D. S. Spiegel and A. Burrows. Spectral and Photometric Diagnostics of Giant Planet Formation Scenarios. *apj*, 745:174, February 2012. doi: 10.1088/0004-637X/745/2/174.

D. S. Spiegel and A. Burrows. Thermal Processes Governing Hot-Jupiter Radii. *apj*, 772: 76, July 2013. doi: 10.1088/0004-637X/772/1/76.

B. Tingley. *personal communication*, September 2013.

A. H. M. J. Triaud. The time dependence of hot Jupiters' orbital inclinations. *aap*, 534: L6, October 2011. doi: 10.1051/0004-6361/201117713.

L. Wade. And a Glossary of Their Quarry. *Science*, 340:570–571, May 2013.

L. M. Weiss, G. W. Marcy, J. F. Rowe, A. W. Howard, H. Isaacson, J. J. Fortney, N. Miller, B.-O. Demory, D. A. Fischer, E. R. Adams, A. K. Dupree, S. B. Howell, R. Kolbl, J. A. Johnson, E. P. Horch, M. E. Everett, D. C. Fabrycky, and S. Seager. The Mass of KOI-94d and a Relation for Planet Radius, Mass, and Incident Flux. *apj*, 768:14, May 2013. doi: 10.1088/0004-637X/768/1/14.

R. G. West, J.-M. Almenara, D. R. Anderson, F. Bouchy, D. J. A. Brown, A. Collier Cameron, M. Deleuil, L. Delrez, A. P. Doyle, F. Faedi, A. Fumel, M. Gillon, G. Hebrard, C. Hellier, E. Jehin, M. Lendl, P. F. L. Maxted, F. Pepe, D. Pollacco, D. Queloz, D. Segransan, B. Smalley, A. M. S. Smith, A. H. M. J. Triaud, and S. Udry. Three irradiated and bloated hot Jupiters: WASP-76b, WASP-82b & WASP-90b. *ArXiv e-prints*, October 2013.

J. N. Winn. *Exoplanet Transits and Occultations*, pages 55–77. 2011.

J. N. Winn, S. Albrecht, J. A. Johnson, G. Torres, W. D. Cochran, G. W. Marcy, A. W. Howard, H. Isaacson, D. Fischer, L. Doyle, W. Welsh, J. A. Carter, D. C. Fabrycky, D. Ragozzine, S. N. Quinn, A. Shporer, S. B. Howell, D. W. Latham, J. Orosz, A. Prsa, R. W. Slawson, W. J. Borucki, D. Koch, T. Barclay, A. P. Boss, J. Christensen-Dalsgaard, F. R. Girouard, J. Jenkins, T. C. Klaus, S. Meibom, R. L. Morris, D. Sasselov, M. Still, and J. Van Cleve. Spin-Orbit Alignment for the Circumbinary Planet Host Kepler-16 A. *apjl*, 741:L1, November 2011. doi: 10.1088/2041-8205/741/1/L1.

Y. Wu and Y. Lithwick. Ohmic Heating Suspends, Not Reverses, the Cooling Contraction of Hot Jupiters. *apj*, 763:13, January 2013. doi: 10.1088/0004-637X/763/1/13.

S. Yi, P. Demarque, Y.-C. Kim, Y.-W. Lee, C. H. Ree, T. Lejeune, and S. Barnes. Toward Better Age Estimates for Stellar Populations: The Y^2 Isochrones for Solar Mixture. *apjs*, 136:417–437, October 2001. doi: 10.1086/321795.

H. S. Zapolsky and E. E. Salpeter. The Mass-Radius Relation for Cold Spheres of Low Mass. *apj*, 158:809, November 1969. doi: 10.1086/150240.

APPENDIX A

Different plots

The following chapter contains images, which I made during my thesis, to either double check the results of authors or my ideas. All of the plots, except Figure A.4, are made in python by the program in Appendix B.

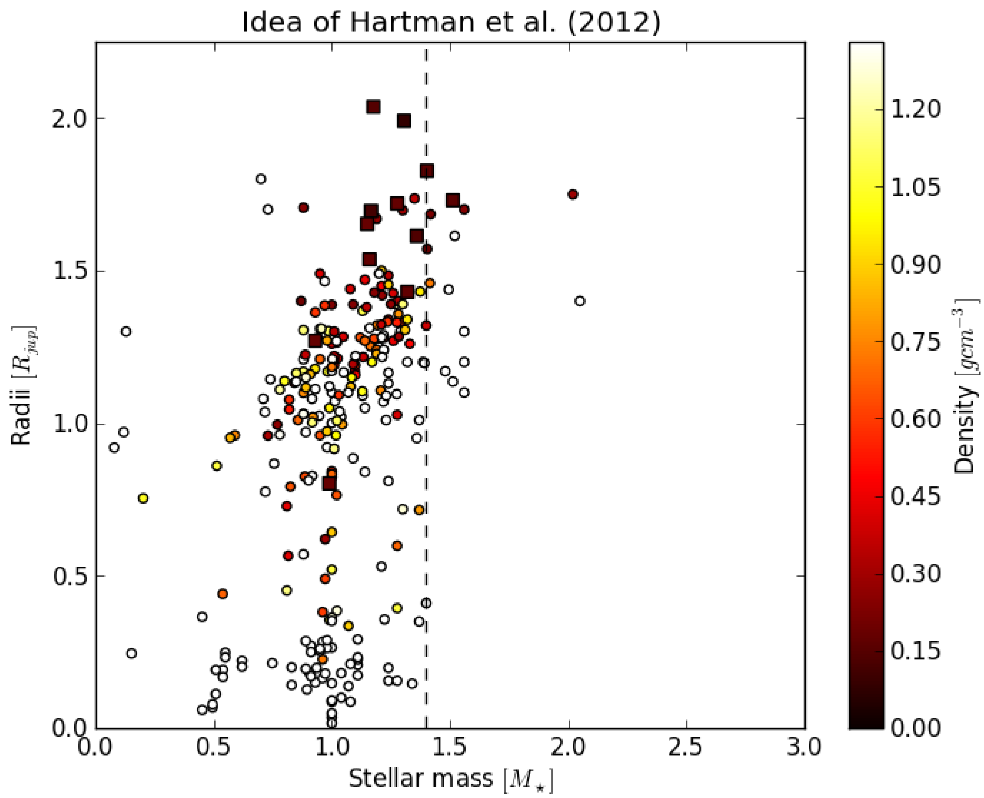

Figure A.1: Hartman et al. (2012) noticed that there is a deficit of exoplanets for masses beyond $1.4M_\odot$ (dashed-vertical line). The figure illustrates that the largest exoplanets are the ones that are least dense, with some exceptions. All exoplanets above the density of Jupiter are marked by white. The squared points are the exoplanets from my low-density sample

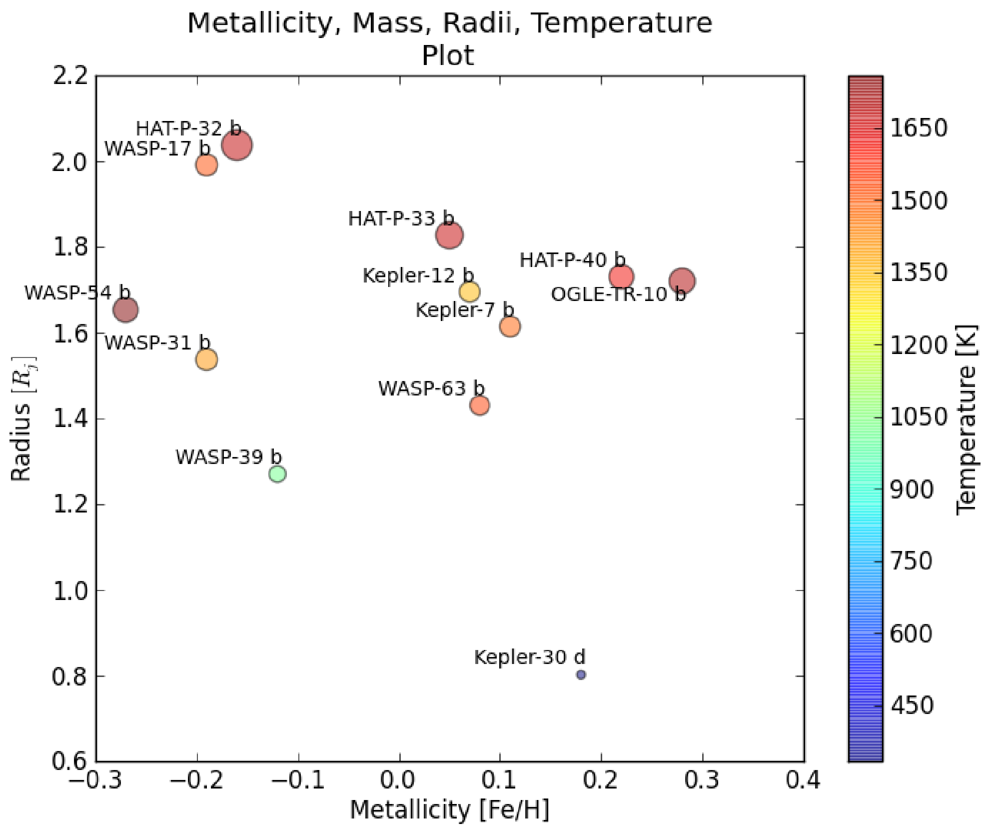

Figure A.2: A figure indicating four different parameters. The x-axis, y-axis with the colorbar being indexed, while the size of the data points is the mass of the exoplanets. The figure illustrates the scattering of exoplanets, but shows a tendency of the more massive planets being the largest. `WASP-17 b` might be a rare case due to its retrograde orbit, as described in section 4.2.6.

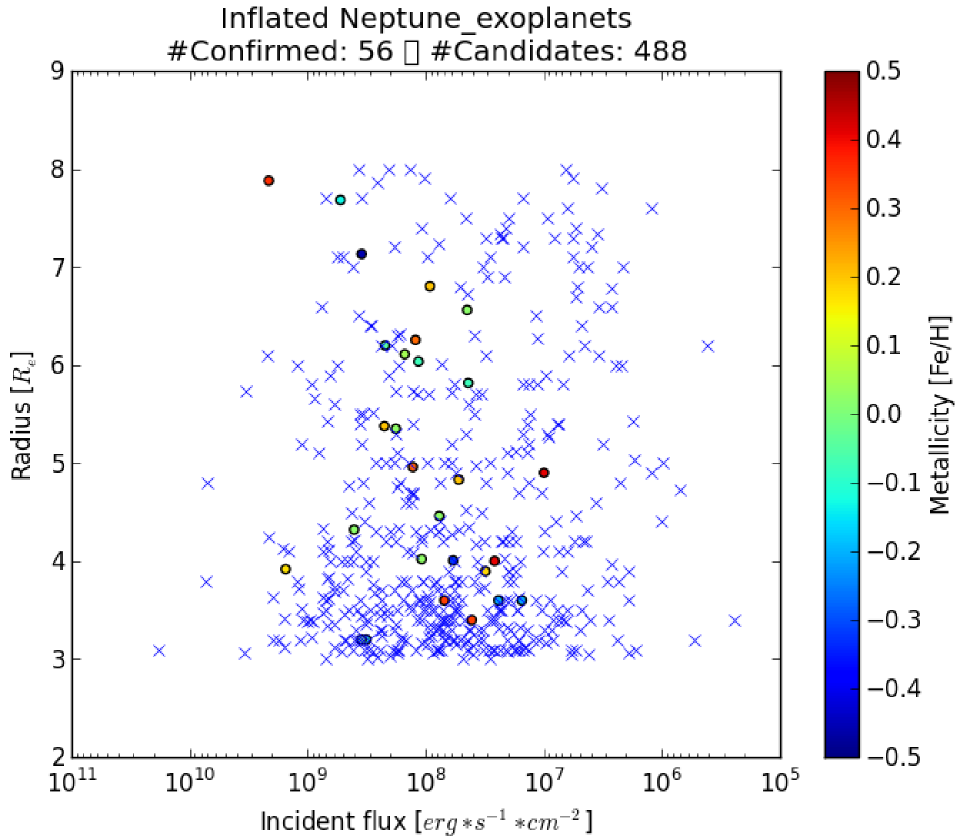

Figure A.3: A figure to investigate if the same tendency as in Figure 5.2 is noticed for a Neptune-like sample; 3R⊕- 8R⊕. It should be noted that 6 of the confirmed exoplanets have masses above the mass of Saturn, as can be noticed in Figure 4.1 (8R⊕= 0.72R_{Jup}). A scatter is clearly apparent from the figure above, hinting towards a heating mechanism only applying more massive exoplanets.

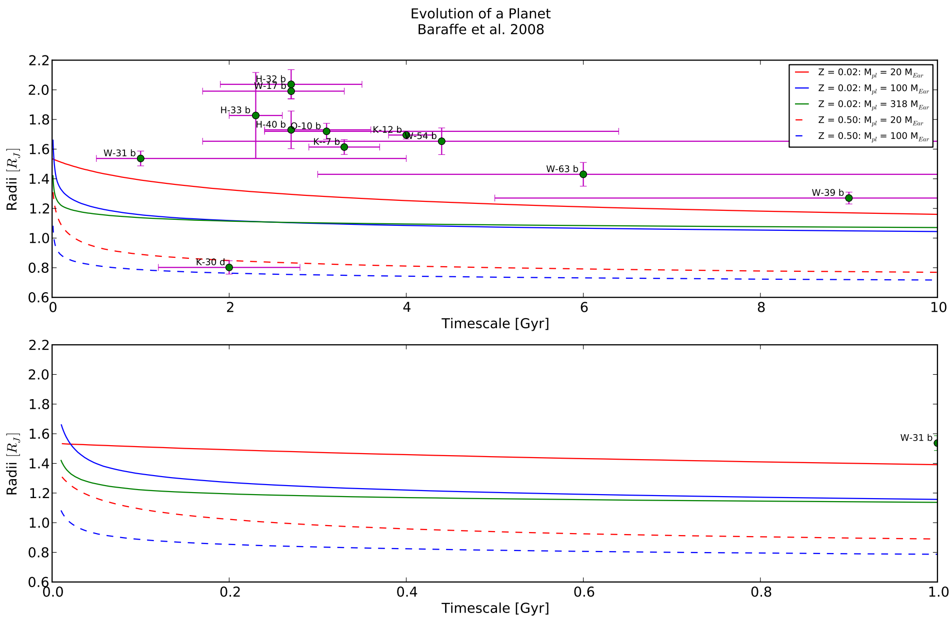

Figure A.4: The Figure depicts the evolution of a planet with three different masses alike Neptune, Saturn and Jupiter by red, blue and green, respectively. The solid line is built upon a Sunlike heavy element enrichment, while the dashed lines indicate planets that have 50% element heavier than Hydrogen and Helium by mass. The model is based on a distance of 0.045 AU to a Sunlike star (Baraffe et al., 2008). The green dots indicate our low-density sample from Chapter 4. If the distance is reduced, then the predicted radii of the models would increase - as seen in (Burrows et al., 2007, cf. Fig. 3).

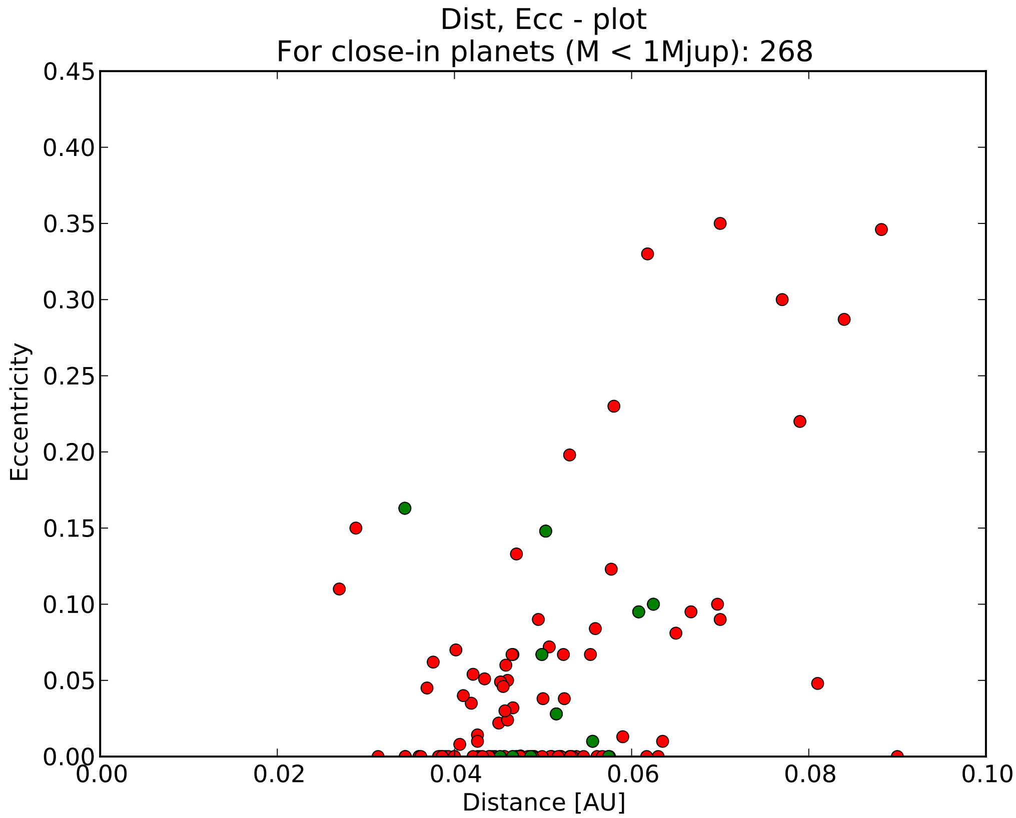

Figure A.5: The figure depicts a mass range in between a Neptune mass and Jupiter mass. The periods of my data in Chapter 3 are low, thus possibly assuming distances within 0.1 AU. The trend shows that most exoplanets seem to have low eccentricities.

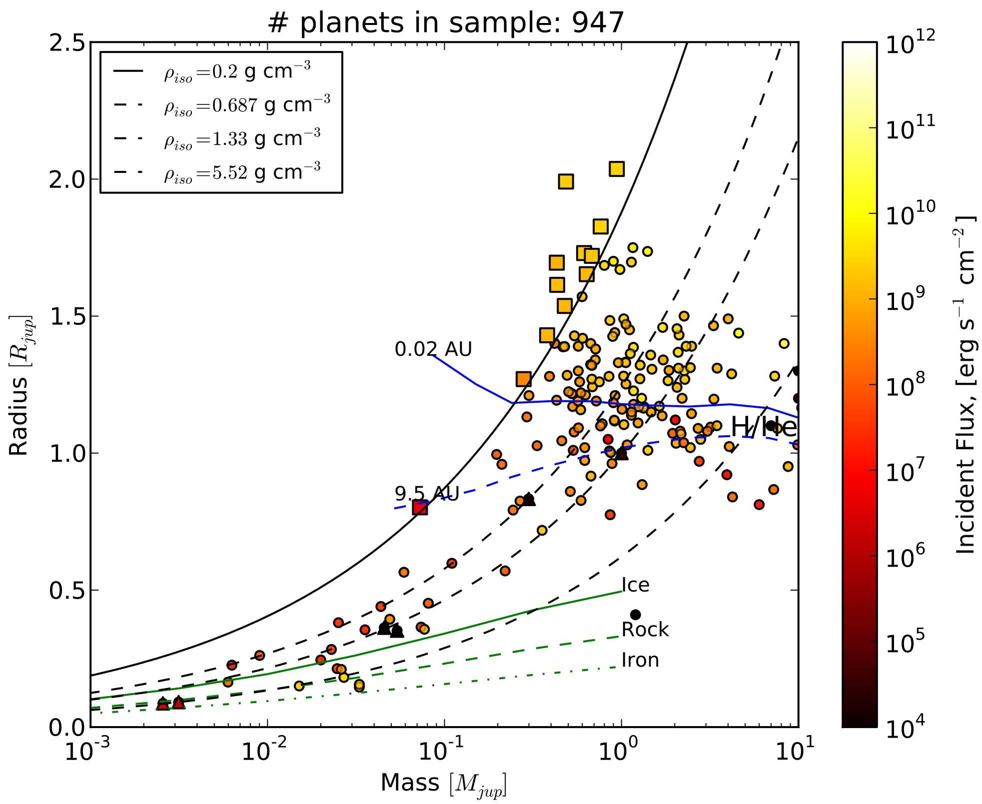

Figure A.6: The figure depicts the (M_{pl}, R_{pl})-plot with the incident flux as colorbar to indicate how the planets are affected by their stellar host compared to their position on the plot.

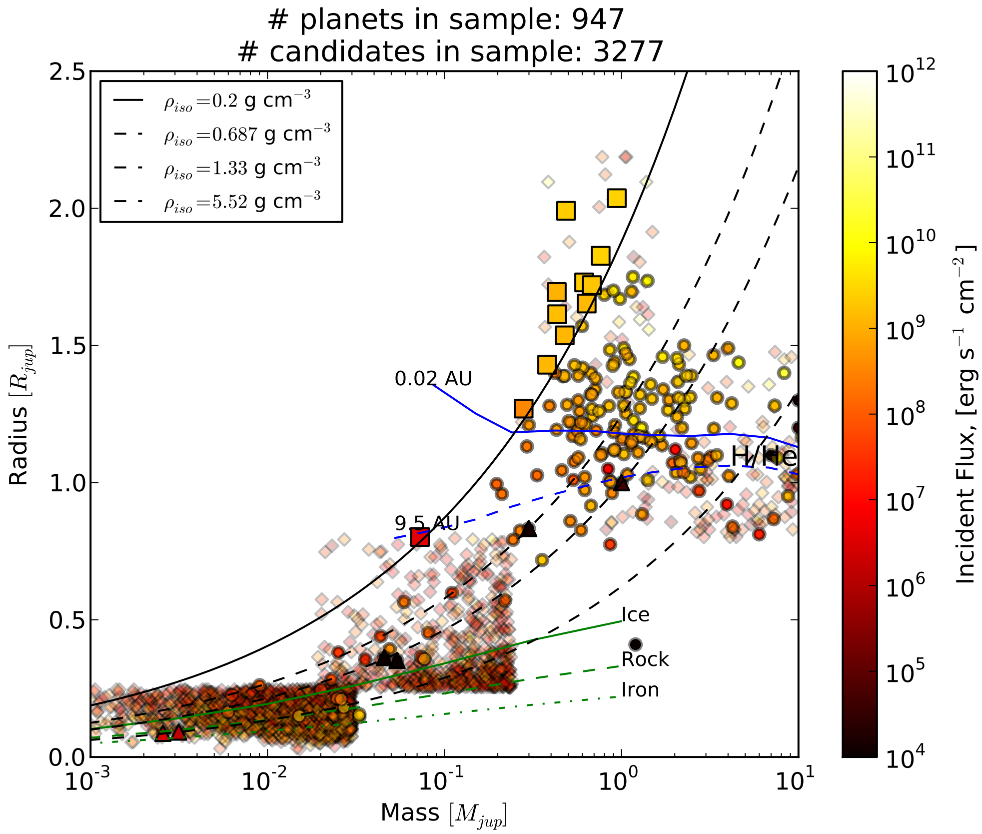

Figure A.7: The figure illustrates the mass-spread of candidates by a rough assumption of their mass. I create a mass sample based on radii from the sample of confirmed exoplanets, i.e. Figure 1.3. The figure clearly depicts a massive amount of oncoming Earth and Neptune-like planets that might be confirmed. The candidate sample also shows a few possible exoplanets that might be inflated, but the interesting fact is that most observed radii in between 0.8 and 1.5 are all below the stellar irradiated lines of Fortney et al. (2007).

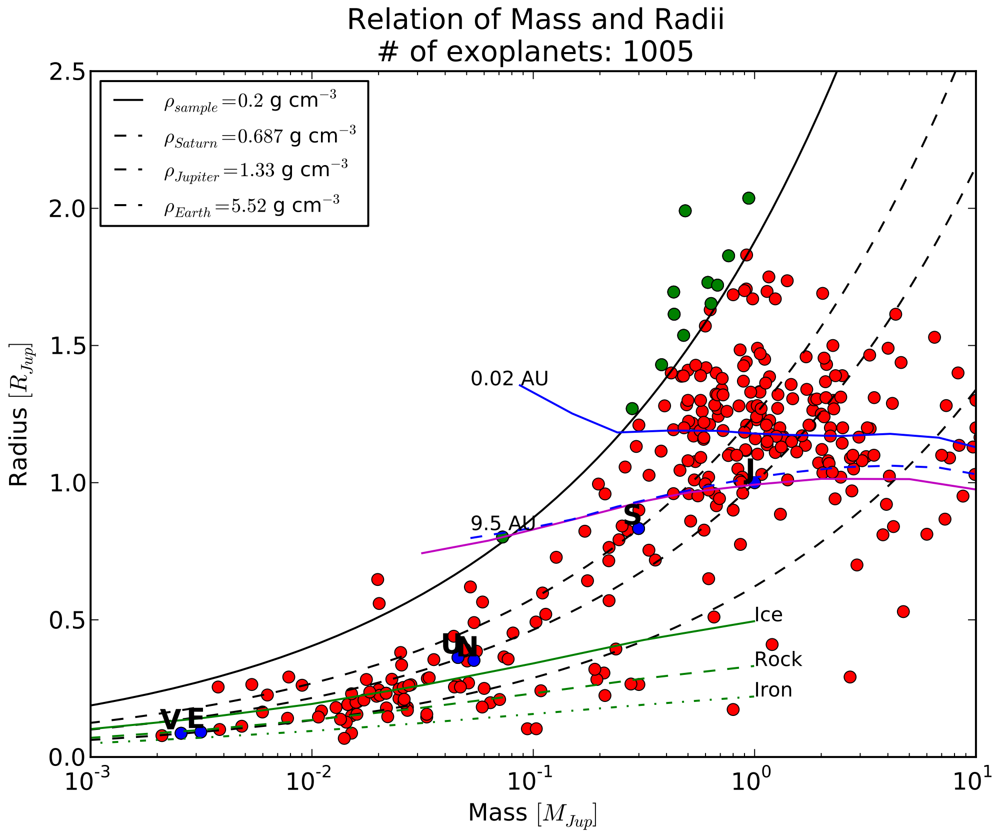

Figure A.8: Same as Figure 1.3 but with newer data (updated 25th of October, 2013) and mass-radii relations of ice, rock and Iron based on equation of states by Seager et al. (2007).

APPENDIX B

The program

My programs have been written in python, and can easily be initialized on most distributions of python. The main program is built on three files, `oec_plot.py`, `Planet_data.py` and `defi_exo.py`. The latter two scripts are my constants and definitions, while the first mentioned is the main script. It utilizes classes, which are based on first author of articles.

An example could be, if the reader wants to reproduce Figure 1.3. The following procedure needs to be applied in python.

`F = Fortney()`	Opens the class of Fortney
`F.`+tab	Shows the possible actions of the class
`F.relation()`	Runs the code in the given class
`plt.show()`	This function will depict the figure, if not shown

Table B.1: The programs will be available on my dropbox link:
https://www.dropbox.com/sh/o171468pleeieg3/eCL5zUDzD9

There has been made multiple programs to fit the data described in Chapter 3. These programs show the same result but various chi-square, which could be due to an error in the first made programs found in folder\K00102 and ..\K0094. But, I would advise the reader to use my newest program, `plot_RV`, which is "user-friendly".